Theses and Dissertations

Fall 2011

Understanding the partitioning of rainfall by the maize canopy through computational modelling and physical measurements

Renato Prata de Moraes Frasson
University of Iowa

Recommended Citation

Frasson, Renato Prata de Moraes. "Understanding the partitioning of rainfall by the maize canopy through computational modelling and physical measurements." PhD (Doctor of Philosophy) thesis, University of Iowa, 2011.
https://ir.uiowa.edu/etd/2702. https://doi.org/10.17077/etd.o37is9xq

UNDERSTANDING THE PARTITIONING OF RAINFALL BY THE MAIZE

CANOPY THROUGH COMPUTATIONAL MODELLING AND PHYSICAL

MEASUREMENTS

by

Renato Prata de Moraes Frasson

An Abstract

Of a thesis submitted in partial fulfillment
of the requirements for the Doctor of
Philosophy degree in Civil and Environmental Engineering
in the Graduate College of
The University of Iowa

December 2011

Thesis Supervisor: Professor Witold F. Krajewski

ABSTRACT

The interception and redirection of rainfall by vegetation has implications for many fields such as remote sensing of soil moisture, satellite observation of rainfall, and the modeling of runoff, climate, and soil erosion. Although the modeling of rainfall partitioning by forests has received attention in the past, partitioning caused by crops has been overlooked. The present work proposes a two front experimental and computational methodology to comprehensively study rainfall interception and partitioning by the maize canopy.

In the experimental stage, we deployed two compact weather stations, two optical disdrometers, and five tipping bucket rain gauges. Two of the tipping bucket rain gauges were modified to measure throughfall while two were adapted to measure stemflow. The first optical disdrometer allowed for inspection of the unmodified drop-size and velocity distributions, whereas the second disdrometer measured the corresponding distributions under the canopy. This indicates that the outcome of the interaction between the hydrometeors and the canopy depends on the drop diameter.

In the computational stage, we created a model that uses drop-size and velocity distributions as well as a three-dimensional digital canopy to simulate the movement of raindrops on the surfaces of leaves. Our model considers interception, redirection, retention, coalescence, breakup, and re-interception of drops to calculate the stemflow, throughfall, and equivalent height of precipitation stored on plants for a given storm. Moreover, the throughfall results are presented as two-dimensional matrices, where each term corresponds to the accumulated volume of drops that dripped at a given location. This allows insight into the spatial distribution of throughfall beneath the foliage. Finally, we examine the way in which the maize canopy modifies the drop-size distribution by recalculating the drop velocity based on the raindrop's size and

detachment height and by storing the counts of drops in diameter-velocity classes that are consistent with the classes used by disdrometers in the experimental study.

Abstract Approved: _____

Thesis Supervisor

_____

Title and Department

_____

Date

UNDERSTANDING THE PARTITIONING OF RAINFALL BY THE MAIZE

CANOPY THROUGH COMPUTATIONAL MODELLING AND PHYSICAL

MEASUREMENTS

by

Renato Prata de Moraes Frasson

A thesis submitted in partial fulfillment
of the requirements for the Doctor of
Philosophy degree in Civil and Environmental Engineering
in the Graduate College of
The University of Iowa

December 2011

Thesis Supervisor: Professor Witold F. Krajewski

Graduate College
The University of Iowa
Iowa City, Iowa

CERTIFICATE OF APPROVAL

_____

PH.D. THESIS

_____

This is to certify that the Ph.D. thesis of

Renato Prata de Moraes Frasson

has been approved by the Examining Committee
for the thesis requirement for the Doctor of Philosophy
degree in Civil and Environmental Engineering at the December 2011
graduation.

Thesis Committee: _____
                    Witold F. Krajewski, Thesis Supervisor

                  _____
                    William Eichinger

                  _____
                    Allen Bradley

                  _____
                    Brian Hornbuckle

                  _____
                    Anton Kruger

To my parents Mirian and Deodoro Frasson and my lovely wife

ACKNOWLEDGMENTS

During my studies at The University of Iowa, I have worked with an amazing array of people, from whom I have learned a wide variety of professional and interpersonal skills. I would like to begin by acknowledging the support, encouragement, and guidance of Professor Witold Krajewski, who made this thesis possible. In addition to the scientific skills that Professor Krajewski taught me, he showed me how to balance my professional and personal lives, how to focus on a task and see it to fruition, and how to maintain sight of where my work fits into the big picture. He improved my ability to present my work and taught me the difference between a poster and a paper.

I would also like to thank the other great educators that I met here: Professor William Eichinger, who changed my views on higher education, and Professors Allen Bradley and Anton Kruger, who were exemplary instructors in the classroom and with whom I had many helpful discussions. I would further like to extend my gratitude to Professor Brian Hornbuckle for helping me deploy instruments in Ames and for serving on my committee.

I would like to acknowledge my colleagues and friends Luciana Kindl da Cunha, Achilleas Tsakiris, Piotr Domaszczynski, and Bongchul Seo for their continuing support and friendship. My time as a student at The University of Iowa would have certainly been much harder without them. Special thanks also to Radoslaw Goska for teaching me about photography, CorelDraw, and ArcGIS. My posters and pictures certainly improved considerably with Radek's and Witek's input. Thanks also to Dr. Cinda Coggins Mosher for her help editing my manuscripts and improving my writing.

Especial thanks to Judy Holland for being always helpful, Daniel Ceynar with whom I learned a great deal about experimental work, Greg Wagner, Wes Cerveny, and David Bowersox for supporting my data acquisition campaign.

ABSTRACT

The interception and redirection of rainfall by vegetation has implications for many fields such as remote sensing of soil moisture, satellite observation of rainfall, and the modeling of runoff, climate, and soil erosion. Although the modeling of rainfall partitioning by forests has received attention in the past, partitioning caused by crops has been overlooked. The present work proposes a two front experimental and computational methodology to comprehensively study rainfall interception and partitioning by the maize canopy.

In the experimental stage, we deployed two compact weather stations, two optical disdrometers, and five tipping bucket rain gauges. Two of the tipping bucket rain gauges were modified to measure throughfall while two were adapted to measure stemflow. The first optical disdrometer allowed for inspection of the unmodified drop-size and velocity distributions, whereas the second disdrometer measured the corresponding distributions under the canopy. This indicates that the outcome of the interaction between the hydrometeors and the canopy depends on the drop diameter.

In the computational stage, we created a model that uses drop-size and velocity distributions as well as a three-dimensional digital canopy to simulate the movement of raindrops on the surfaces of leaves. Our model considers interception, redirection, retention, coalescence, breakup, and re-interception of drops to calculate the stemflow, throughfall, and equivalent height of precipitation stored on plants for a given storm. Moreover, the throughfall results are presented as two-dimensional matrices, where each term corresponds to the accumulated volume of drops that dripped at a given location. This allows insight into the spatial distribution of throughfall beneath the foliage. Finally, we examine the way in which the maize canopy modifies the drop-size distribution by recalculating the drop velocity based on the raindrop's size and

detachment height and by storing the counts of drops in diameter-velocity classes that are consistent with the classes used by disdrometers in the experimental study.

TABLE OF CONTENTS

LIST OF TABLES

LIST OF FIGURES

Figure

CHAPTER I.

A REVIEW OF RAINFALL INTERCEPTION BY A MAIZE CANOPY

Introduction

Thoroughly understanding rainfall interception by vegetation is crucial to many fields including runoff and local climate modeling, soil erosion management (Bui and Box, 1992), crop disease management (Magarey et al., 2006), irrigation management (Steiner et al., 1983), ground water quality control (Parkin and Codling, 1990), and remote sensing of soil moisture (Hornbuckle et al., 2007). From the moment rain drops hit the plant canopy until they reach the soil surface, their interactions with vegetation have important implications.

With respect to the remote sensing of soil moisture, there are at least two implications. The most straightforward of these is the influence of stored water on the microwave radiation emitted (or scattered) from areas covered by vegetation. Water trapped on plants interacts with microwave radiation, introducing errors into estimates of soil moisture for the area under the canopy. Consequently, it is important to fully understand the partition of rainfall into interception, throughfall, and stemflow, as well as its variation over time, during and after rain events.

The second implication pertains to the redistribution of rainfall beneath a maize canopy and the small-scale variability of soil moisture. The literature shows that there is a considerable concentration of water in the area immediately adjacent to the roots, mostly due to rainwater brought to the soil as stemflow. This concentration generates areas where soil moisture is much higher than in the surroundings, which calls into question what estimated soil moisture truly represents. While data on soil moisture in the area adjacent to the roots may not be directly relevant to subjects such as flash flood prediction, it is crucial to crop management, and the redistribution of rainfall under the canopy is significant to both flash flood prediction and crop management.

Prediction of the amount of water stored on crop canopies could be of importance to space borne observations of rainfall by passive microwave sensors, such as the Global Precipitation Measurement (GPM) mission. The instrumentation used in the GPM mission consists of one dual-band radar and a 13-channel microwave radiometer with frequencies ranging from 10 to 183 GHz attached to a 1.2m conical-scanning antenna. As this system scans the earth's surface, it measures the brightness temperatures while using an emissivity model to estimate a vector of variables that characterize the state of the atmosphere such as water vapor, cloud water content, and drop size distribution among others (Kummerow, 2009).

To examine how rainfall interception and subsequent partitioning by crop canopies could interfere with the observation of rainfall by satellites, let us pose three questions: How will the rain water stored on plants be incorporated into the emissivity model? Is the water stored on or in the plants visible during the retrieval of the microwave signature of the atmosphere? Can one tell the difference between wet and dry plants? Estimating the influence of rain water stored on and in plants on microwave signals is not an easy task, *e.g.* the works of Wigneron et al. (2007), Hornbuckle et al. (2007) and Hornbuckle et al. (2006). We believe that water storage prediction tools are important pieces in the multidisciplinary puzzle of microwave remote sensing of rainfall and soil moisture.

<u>Evolution of the measurement techniques</u>

Haynes (1940) measured stemflow using a funnel attached to the maize stem and sealed with wax to divert the flow to a recipient where it was stored and measured. Throughfall was collected using galvanized metal pans with a depth of approximately 100 mm and rectangular cross sections of 1066.8 mm by 1066.8 mm placed between rows. He started his measurements of throughfall and stemflow when the plants were approximately 1.82 m high and continued until the crop was harvested. At the maximum

stage of development, the maize plants were 2.40 m high and had 55 to 65% foliage cover (percentage of ground area covered by leaves when observed from the top). This technique successfully provided the accumulated throughfall and stemflow, but provided no information on the spatial distribution of the throughfall or on the evolution of the processes of stemflow and throughfall with time.

Quinn and Laflen (1983) grew maize plants in 20 liter receptacles filled with soil and placed them under a rainfall simulator at three different row distances, namely 305, 500, and 700mm. They performed the rainfall simulations at different ages, 5, 12, and 15 weeks after emergence. They installed a gutter beneath the plants to collect the throughfall and inserted a specially treated filter paper between the lower remaining leaf and the gutter to measure drop diameters. In their work, stemflow was estimated by taking the difference between the volume incident on the vegetation and the volume of water collected by the gutter, implying that interception of rainfall by a maize plant was negligible.

In 1980 and 1981, Steiner et al. (1983) measured the partition of irrigation water and rainfall by a maize canopy. They measured the stemflow, throughfall, and incident amount of water and used these three parameters to calculate the interception by the vegetation according to equation (I-1) where I_p denotes the interception of water by the plants, D_n denotes the depth of water applied to the plant, T denotes the measured throughfall, S denotes the measured stemflow and E_c denotes the evaporation of water within the canopy region.

$$I_p = D_n - T - S - E_C \qquad \text{(I-1)}$$

In their first campaign, they used 20 rain gauges that were elevated above the canopy height and distributed around the experimental plot to measure the incident amount of water applied to the plants. In their second campaign the following year, they used 12 gauges in each of the three evaluated locations. 40 rain gauges arranged at the

soil surface beneath the canopy captured the throughfall, and stemflow was measured in 20 plants, 10 of which were taken from one row and 10 from an adjacent row.

The stemflow was measured after the irrigation or precipitation event. It was diverted from the plant stem using a collection funnel installed around the stem and sealed to the plant using silicone. The water captured by the funnel was taken to a recipient for storage. The stemflow was then calculated by dividing the accumulated volume by the area occupied by the plant. Unfortunately, there is no further explanation on how this area was determined.

Their evaluation was done only when the leaf area index exceeded 3.0. At that time, almost half of the incident water had reached the ground in the form of stemflow. They also found that the proportion between stemflow and throughfall was not sensitive to the method of water application. Approximately the same proportion of stemflow and throughfall was reported for both natural rainfall and irrigation.

Armstrong and Mitchell (1987) demonstrated that crop canopies such as corn and soybeans modify not only the volume of raindrops reaching the ground, but also their sizes and spatial distribution. By placing dye paper underneath the two canopies and simulating rainfall for short periods of time, the authors were able to measure the stain diameters and their positions. They found that, for both examined canopies, the throughfall median volume diameter was larger than that of the generated rainfall. They also found that the soybean and the corn canopies concentrated rainfall in well-defined dripping points, with dripping being less intense beneath corn. In a later work, Armstrong and Mitchell (1988) described the processes that take place on leaves that are responsible for changing drop characteristics.

Also van Elewijck (1989b) measured stemflow in single plants at the laboratory using a rainfall simulator and in the field subjected to natural rainfall. In both experiments, stemflow was collected by a 10 cm diameter funnel attached to the maize stem. Water captured by the funnel was diverted into a tube leading to a measuring

cylinder that was read every minute for ten minutes in the laboratory experiment and after several days in the field experiment.

Based on van Elewijck's stemflow measurements, one can expect a flow of three millimeters per hour under rainfall with an intensity of 0.2 ml/h and a flow of 990 ml/h under rainfall with an intensity of 17 mm/h. The author also states that the amount of stemflow varies with the season, and is especially different at the end of the season when many of the leaves are broken and partially lose their ability to direct the flow towards the stem. The influence of leaf angle was investigated in a separate work by van Elewijck (1989a), who found that low slope angles (between 5º and 20º) are more efficient to generate stemflow for corn. This contradicts the equation developed by de Ploey (1982) for grasses, which predicts that the optimum stemflow generation angle is between 40º and 50º.

From July through September of 1987, Parkin and Codling (1990) measured the stemflow and total incident rainfall, starting when the maize was 70 cm high. They constructed a stemflow collector using a 150 milliliter plastic beaker attached around the maize stem and sealed with paraffin wax. A hole was drilled in the bottom of the beaker, through which flow was diverted into a recipient for collection and latter measurement, occurring one to six hours after the end of the rainfall event. They installed three rainfall collectors perpendicular to the rows and three between plants, but no further detail is given on the rainfall collector design. The measurements were restricted to totals after each rainfall event for a total of eight events.

Bui and Box (1992) also studied stemflow and throughfall to better understand erosion beneath maize and sorghum canopies. They used a rainfall simulator to generate rainfall with a constant intensity of 63.5 mm h^{-1}. The authors conducted their experiment on a plot where the spacing between rows was approximately 0.5 m and the spacing between plants was approximately 0.25 m. Their experiment was conducted with mature maize plants cut to the height of 1.73 m.

The authors estimated throughfall by taking the difference between the rainfall rate and the stemflow and disregarding the volume of water stored on the plants. They compared their stemflow measurements to the predictions of the equations derived by van Elewijck (1989b) and de Ploey (1982) and found that van Elewijck's equation consistently overestimated the stemflow while de Ploey's equation fits the data better.

In a more recent work, Lamm and Manges (2000) measured the stemflow in 16 plants by attaching a funnel to the maize stem that collected and directed the stemflow to a reservoir jug. The jug accumulated the stemflow during the irrigation or natural rainfall event and was measured within two hours after each event, except in cases of natural rainfall events occurring at night. The authors also measured the throughfall by locating pans between the rows. The volume collected was measured and divided by the land area to express the results as heights.

Bussière et al. (2002) used a more advanced system to measure the throughfall by installing several 6.5 by 4.8 cm rectangular plastic boxes under one maize plant. The authors indexed the plastic boxes and recorded their relative position to the plant, thereby forming a grid of throughfall collectors. The stemflow was measured using a funnel placed just above the soil level to collect the water and redirect it to a recipient.

Their stemflow and throughfall measurement setup was installed on a single plant at a laboratory. They measured the partition of rainfall between throughfall and stemflow after 15 minutes of simulated rainfall, at which point they applied a total rainfall of eight millimeters. By weighing the collectors, the authors obtained the quantity of water accumulated by each throughfall box and by the stemflow collector.

From monitoring the throughfall and the rainfall above the canopy and estimating the stemflow through a water budget, for seven storms, Hupet and Vanclooster (2005) found ratios between stemflow and incident rainfall ranging from 13% to 66%. Part of this variability may result from the fact that the measurements were done in different growth stages and under different rainfall intensities.

Others such as Dolan et al. (2001), addressed the partitioning of rainfall by vegetation using a very similar methodology. Although the methods used by different authors are similar, the variability of the results of stemflow and throughfall measurements is considerable. Such a large variability of results suggests that we still don't fully understand all the phenomena affecting the partitioning of rainfall by vegetation.

Levia and Frost (2003) reviewed the literature and compiled measurement techniques and models to predict the stemflow in plants; however, they were more focused on stemflow measurement and prediction in forests.

Even though the interception of rainfall by vegetation, and especially by a maize canopy, was investigated in a number of works, there is no consensus regarding such fundamental aspects as what area should be used to normalize the volume of stemflow and throughfall, which variables should be controlled or at least observed during the experiments, and how to group variables during data analysis.

<u>Modeling of the partitioning of rainfall by vegetation</u>

Norman and Campbell (1983) described the Cupid model which aims to estimate canopy and soil conditions given the soil and plant characteristics, namely the leaf area index, plant height, height of the lowest leaves, height of the densest region of the canopy, row and plant spacing, the mean leaf size of the canopy, the leaf angle distribution, foliage spectral properties, stomatal conductance versus light, temperature, leaf water potential, plant hydraulic resistance, and root length density distribution.

The Cupid model uses the leaf area index to estimate the direct throughfall under a maize canopy by means of equation (I-2), where T stands for the proportion of direct throughfall accumulation and LAI for the leaf area index. The authors state that one can expect that 25% to 65% of the intercepted rainfall by maize plants will reach the ground in the form of stemflow. The authors point out that plant morphology, leaf inclination,

and plant history can influence the partition between dripping and stemflow but do not explain how they are taken into account by the Cupid model or whether or not they are used to correct the calculations.

$$T = e^{-0.5LAI} \tag{I-2}$$

The equation developed by de Ploey (1982) predicts the stemflow of grasses and similar vegetation. His model estimates the volume of stemflow concentrated at the base of the plant using parameters derived from the plant geometry. His equation is shown in (I-3), where *ICR* is the stemflow amount in cubic centimeters concentrated at the base, I_r the rainfall intensity, t the rainfall duration, S_b the area of the funnel, L_i the length from the stem to the bend, w_i the mean width, and $\overline{}_i$ the slope of the *i*-th leaf, n the number of leaves, and R a factor to adjust the rainfall intensity. According to his data, the R values generally vary from one to two depending on the intensity of the rainfall.

$$ICR = S_b \cdot I_r \cdot t + R \cdot \sum_{i=1}^{n} \left(L_i \cdot \cos(\overline{}_i) \cdot \sin^2(\overline{}_i) \cdot \overline{w}_i \cdot I_r \cdot t \right) \tag{I-3}$$

Although the model described by Calder (1986) was derived for trees, the proposed stochastic approach can be extended to a maize canopy. The author begins by dividing the canopy in elemental areas and assumes that the wetting of these areas is a random process governed by Poisson statistics. One can estimate the actual amount of water stored in a canopy by using equation (I-4).

$$C = n \cdot v \cdot L \tag{I-4}$$

In equation (I-4), *C* stands for the actual amount of water stored in a canopy per ground unit area, *n* for the number of drops that attached to the leaf's elemental area, *v* for the median volume of raindrops and *L* for the number of elemental area surfaces per unit ground area. The parameter *n* is calculated using Poisson statistics that depends on the storage capacity of the canopy, while *v* can be estimated through disdrometer measurements or through drop-size distribution and terminal fall velocity models.

This one layer stochastic model has some noteworthy limitations, however. The author assumes that the storage capacity of the canopy depends only on rainfall regime and type of vegetation; however, in a latter work (Calder, 1996), the author acknowledges that the storage capacity should also be controlled by the kinetic energy of the drops.

Calder (1996) improved upon the basic stochastic model by representing the canopy with two layers and by incorporating the dependence of the maximum volume of intercepted water on the kinetic energy and volume of the drops. By using a two-layer model, the author intended to capture the influence of the origin of the drop, whether primary rainfall or dripping from higher levels, into the water interception capacity. This addition allows the use of a modified drop-size distribution for drops falling from the upper layer into a lower one.

The addition of a second layer of leaves in the model creates a need for extra parameters, namely, a projected area index of the canopy, a projected area index of the two layers, the number of elemental areas on the first and second layers, the volume of raindrops that hit the first and the second layers of the canopy per unit ground area, the depth of water shed from the top layer, the maximum canopy storage for non-zero kinetic energy drops, the maximum canopy storage for the upper layer, and the maximum canopy storage for the lower layer.

The differences between the storage capacity obtained by the two-layer stochastic and the single-layer models decrease with the density of the canopy and, according to the example shown in Calder (1996), the results from the two-layer model converge to that obtained by the single-layer model when the canopy is dense enough.

Calder et al. (1996) tested the two-layer stochastic model on five species of trees using a rainfall simulator. The samples taken from the trees were attached to a scale under a rainfall simulator. The change in weight registered by the scale was used to estimate the interception, and a funnel located below the vegetation sample collected the throughfall.

The paper's most significant result is that the interception capacity C_{max} is not constant with respect to the application rate, rainfall rate, or drop-size distribution. The authors attribute the variation of the capacity to the variation in the kinetic energy of the drops that results from different drop-size distributions.

In a more recent work, Bussière et al. (2002) described the DROP model, which calculates the throughfall height and spatial distribution given a three-dimensional digital model of a plant. The authors identified four simplifying assumptions that can affect accuracy of the drop model when dealing with the maize canopy: storage is neglected, dripping points are fixed, *i.e.* the digital plant is rigid, interception of rainfall by other plant organs is negligible, and raindrops fall vertically. Moreover flow on the stem is not explicitly considered, being replaced by dripping around it.

Although there aren't many attempts to model the partitioning of rainfall by a maize canopy, there are numerous models developed for forests, with some of the ideas developed by Rutter and Kershaw (1971), Rutter et al. (1975), and Rutter and Morton (1977). Also, the model by Gash (1979), which can accommodate other canopies, was recently used to derive the interception of rainfall by forests on a global scale by Miralles et al. (2010).

Other interesting modeling studies include Schellekens et al. (1999), van Dijk and Bruijnzeel (2001a) and validated by van Dijk and Bruijnzeel (2001b), Lewis (2003), Hall (2003), Keim et al. (2004), Keim and Skaugset (2004), and more recently Keim et al. (2006), Wang et al. (2005) and Wang et al. (2007), Bassette and Bussière (2005), Murakami (2006), and Limousin et al. (2008). A literature review discussing the interception of rainfall by vegetation was recently published by Muzylo et al. (2009) and includes other examples.

Summary

In this chapter, we summarized experimental and computational studies of the interception and redirection of rainfall by canopies. Although the partitioning of rainfall by forest canopies has been extensively studied, crop canopies remained relatively untouched. We identified three existing models developed to study the interaction of rainfall with crop canopies. The first one called Cupid model by Norman and Campbell (1983) incorporates evapotranspiration in addition to the estimation of the partitioning of rainfall by plants, but lacks a rigorous three-dimensional description of the canopy. The second model, by Calder et al. (1996) predicts the throughfall drop size distribution, but also lacks explicit considerations regarding the canopy's three-dimensional geometry. The third model, called DROP, developed by Bussière et al. (2002) explicitly takes into account the geometry of a plant to generate two-dimensional maps of the throughfall; however, it doesn't estimate rainfall storage or stemflow and its use was just demonstrated for isolated plants.

To improve upon these models, we adopted a two front approach to examine the interception, partitioning and storage of rainfall by a maize canopy. The present study begins with a description of experimental measurements and ends with the development of a physics-based model that explicitly simulates the movement of rain drops through the canopy to calculate the stemflow, throughfall, rainfall storage, throughfall drop-size, velocity, and two-dimensional spatial distributions.

CHAPTER II.

OBJECTIVES AND METHODOLOGY

Introduction

This chapter summarizes the overarching objectives of our project and delineates the intermediate steps that we took to achieve them. We outline the methodology for each objective and indicate which chapters provide in depth discussion of the issues.

Objective

The overall objective of the present work is to study the interception, partitioning, and modification of rainfall by a maize canopy. In this work, the term interception of rainfall is defined as the fraction of the incoming rainfall that hits the canopy and is partitioned into indirect throughfall, stemflow, and plant storage, whereas direct throughfall constitutes the drops that find a direct path to the soil surface. Our ultimate goal is to predict accumulations of each of these rainfall fractions as well as to determine the characteristics of the rainfall under the canopy such as drop-size distribution and kinetic energy flux based on the three dimensional structure of the canopy and the incoming drop-size distribution.

Goals and methodology

The literature review presented in CHAPTER I indicates that the interpretation of the experimental results is not straightforward. Consequently, we propose a combination of experimental and simulation work to enhance our understanding of the natural phenomena surrounding the partitioning and modification of rainfall by the canopy.

We begin our study with the description of the collected experimental data in CHAPTER III. We discuss the data collected year by year, beginning in the summer of 2007, when only stemflow was collected, followed by another attempt in 2008, when a prototype of a throughfall collector was added to the instrumental setup. We continued

the data collection in 2009, when we deployed fully functional throughfall and stemflow collectors, a regular tipping bucket to measure the rainfall outside of the canopy, two disdrometers (one outside and a second beneath the canopy) and compact weather stations to measure wind velocity. CHAPTER IV elaborates on the analysis of the modification of the throughfall drop-size and velocity distributions and provides possible physical mechanisms that lead to the observed data.

Because data analysis alone does not fulfill our objective of understanding and predicting the partitioning of rainfall by a maize canopy, we developed a physics-based model to understand the movement of rain drops through the canopy. The wide range of scales involved in this study, from the interaction of single water droplets with the maize leaves' trichomes, to the multitude of leaves that forms a canopy, renders solving this problem through a conventional computational fluid mechanics approach unfeasible given our current computational resources. As a result, we chose a semi-empirical approach that begins with obtaining a detailed three-dimensional digital representation of the canopy.

In CHAPTER V, we describe the creation of a three-dimensional digital model of a maize canopy. We present an overview of available digitizing techniques, followed by the presentation of the photogrammetry-based methodology that we applied to assemble a three-dimensional digital model of isolated plants. The last section of the chapter addresses the creation of a realistic canopy based on replicas of a plant model carefully positioned to mimic the field plant density and other observable canopy parameters.

CHAPTER VI describes the development of an explicit rainfall interception model that simulates the movement of raindrops through the digital canopy. The simulation encompasses the evaluation of drop interception, assessment of drop breakup, the decision process of whether or not intercepted drops move, and finally determination of their trajectories. The objective of this chapter is to forecast the throughfall, stemflow

and plant water storage totals for a given storm and also to predict the throughfall drop-size, velocity, and two-dimensional spatial distributions.

Summary

This work intends to enhance the current state of understanding of the partitioning and modification of rainfall by a maize canopy. We address this objective by first measuring and observing the effects of the interaction of rainfall with the canopy, followed by the creation of a three-dimensional model of the canopy and the development of a rainfall interception model. The model allows the prediction of storm totals of stemflow, throughfall, and plant water storage. Subsequently, we aspire to simulate the movement of water drops through the canopy, including modeling drop breakup and coalescence, in order to offer insight into the modification of drop-size and velocity distributions caused by the interaction of rainfall and vegetation. We conclude with a comparison of simulations with measurements taken in fields in Iowa City and Shueyville, Iowa.

CHAPTER III.

MEASURING THE PARTITIONING OF RAINFALL BY A MAIZE

CANOPY

Introduction

This chapter describes our experimental attempts in which we collected data during four summers in order to measure the partitioning of rainfall into stemflow and throughfall. In 2007, we tested a stemflow gauge, and in 2008, we added a throughfall collector to our experimental setup. The equipment used in 2009 featured two improved throughfall gauges, two stemflow gauges, two optical disdrometers, and one reference tipping bucket.

Measuring the stemflow and the throughfall

The 2007 experiment

In the first year of the experiment, we modified a tipping bucket rain gauge to collect and measure the volume of the stemflow collected from one plant. The tipping bucket's funnel was replaced by a stemflow collector attached to plastic tubing that collected and redirected the stemflow to the tipping bucket. We shielded the buckets from other sources of rain by fastening a prismatic plastic container that faced downward and that had an opening to allow the passage of the tubing system, as shown on the right hand side of Figure III-1. The stemflow collector (left hand side of Figure III-1 was made from the flexible yet resistant material from a baby bottle nipple and adjusted to small changes in the stem diameter.

As we replaced the original funnel of the tipping bucket rain gauge, the tips registered by the stemflow gauges no longer corresponded to 0.254 mm of rainfall, which was the measurement of the original gauges. An area is needed in order to translate from the raw number of tips into a "height" of stemflow.

Figure III-1. The left hand side shows a view of the stemflow collector attached to the maize stem. The right hand side shows the modified tipping bucket with indirect rainfall protection. Tubing is attached to a stemflow collector that redirects the water flowing down the stem to the tipping bucket gauge.

At this point there are two options available to calculate the plant area, one derived from the top view of the plant (Figure III-2), and a second from plant spacing. The former is useful for comparing plants at different stages of development, whereas the latter is useful for comparing stemflow with throughfall and total rainfall. We present the areas derived fromFigure III-2 in Table III-1 and offer the area of a regular tipping bucket and the plant area (reciprocal of the plant density) for comparison.

We recorded a total of 11 storms during this first year of experiments. Ten of these took place in a short period of time from 07 August 2007 to 23 August 2007. During these two weeks, the plant was already displaying all leaves and had not yet begun to dry, which allowed us to assume that the plant area calculated from the top view of the canopy (left hand side of Figure III-2) is valid for all 10 events. The month of September was dry, with its single storm occurring on 25 September 2007.
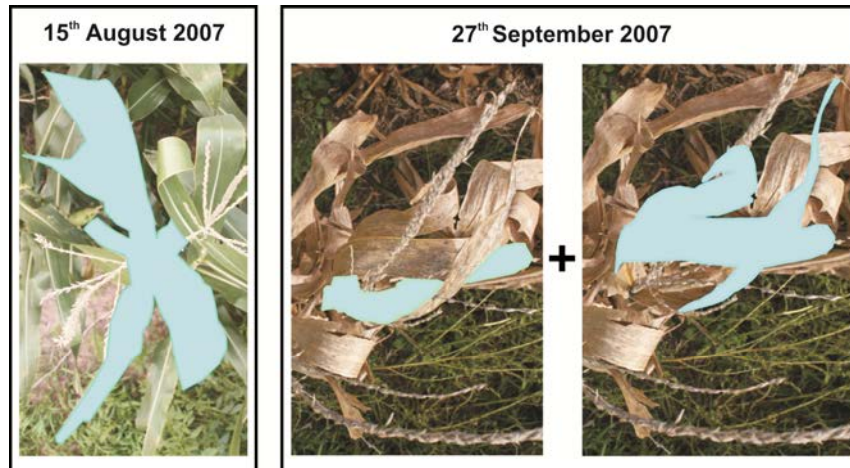
Figure III-2. Top views of the canopy used to calculate the plant catchment area on 15 August 2007 and 27 September 2007. Due to the areal contributions coming from distinct heights, we calculated the area of the 27 September 2007 plant in two stages to minimize errors introduced by lens distortion.

Table III-1. Plant area calculated from the top view of the canopy.

Catchment area (cm^2)		
Rain gauge		735.4
Plant	August 2007	1186
	September 2007	134.5
From plant density		1140

Note: Calculated areas at two distinct ages, August 2007, when the plants displayed all their leaves yet before they began to dry and September 2007, when they were already dry. The original tipping bucket rain gauge area is also shown as a reference.

The left hand side of Figure III-3 shows the number of tips per recorded event during the experiment. The blue dots denote data collected in August, while the green triangle represents the storm registered in September. We observe a quite linear pattern between stemflow and reference rainfall tips for the month of August, but this trend does not continue with the storm recorded in September. However, when we use the plant areas presented in Table III-1 to transform the number of tips into height of stemflow, the linearity greatly improves, as shown on the right hand side of Figure III-3. This supports

our contention that our method allows for the comparison of stemflow of maize plants at different stages of development during the growing season.
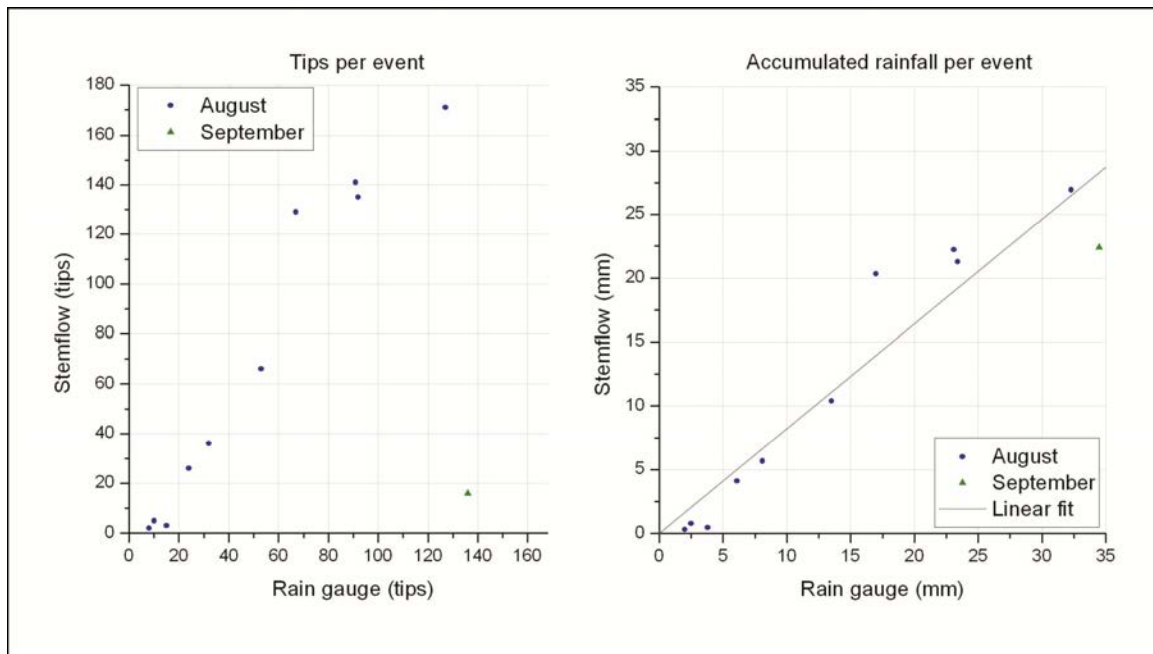
Figure III-3. Number of tips per event of stemflow versus reference rainfall and their corresponding accumulations after normalization using the areas presented in Table III-1 for the 11 recorded events during the summer of 2007.

The 2008 experiment

In 2008, we incorporated two prototype throughfall collectors into our experimental setup that consisted of a rectangular funnel measuring approximately 90 cm in length and 15 cm in width. Each collector directed the throughfall to a tipping bucket which, together with a regular tipping bucket and two stemflow collectors, were connected to a datalogger. The width of the throughfall collector and the diameter of the tube that directed the collected water to the tipping bucket proved to be shortcomings of the original design, which we addressed the following year. Since the collectors were too narrow in comparison to the row spacing (90 cm), and also because the tubing that

directed the water from the collector to the tipping bucket frequently clogged, the quality

of the throughfall measurements is questionable.

Figure III-4 shows the 1-hour stemflow and throughfall accumulations plotted

against the corresponding reference rainfall measurements. The throughfall collectors

were clogged during one of the events, which caused the zero throughfall accumulation

during rainfall. Applying linear regression to the stemflow and reference rainfall dataset

gives us the relationship described by equation III-1, which is graphically represented as

the solid black line in the left panel of Figure III-4.
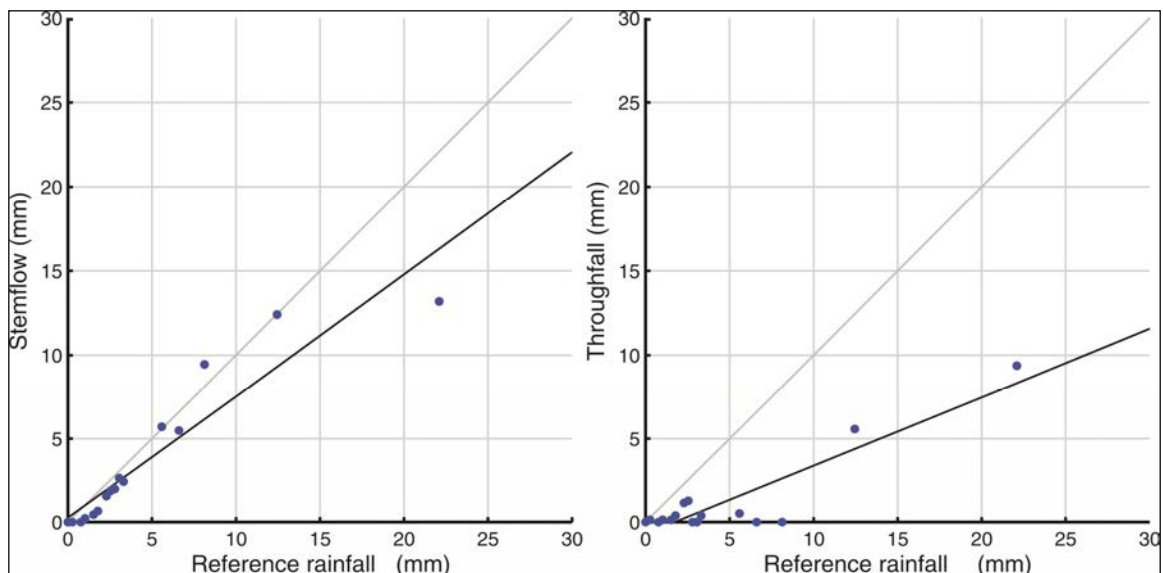
Figure III-4. 1-hour accumulations of stemflow (left panel) and throughfall (right panel)
versus rainfall rate outside of the canopy. Data comprises 5 events taking
place between 19 July 2008 and 21 August 2008.

During the five presented storms, r^2 (square of the correlation) between stemflow

and reference rainfall was 0.87. Even though the presented linear regression does not

describe the data well because it is highly influenced by one point, we show it without

changes. If the point (9.3, 22.1) is removed from the series, the fit of the regression line

is improved. It then displays a negative intercept, which is coherent with water being trapped on the plant. However, it creates an unrealistic prediction of stemflow for storms with accumulations higher than 10 mm.

$$Stem_{acc} = 0.73 \cdot R_{acc} + 0.25 \qquad\qquad\text{(III-1)}$$

The 2009 data collection campaign

We rebuilt the throughfall collectors, increasing the tubing diameter and, more importantly, the collector width. The new collectors featured a rectangular catchment area of 50 by 120 cm, which covers half the distance between the rows used in the examined field. In addition to installing a tipping bucket rain gauge outside of the canopy and two stemflow and two throughfall sensors beneath the canopy, we also deployed two optical disdrometers (Thies LPM) and two compact weather stations (Vaisala WXT510).

The two compact weather stations were installed outside of the canopy to record the wind speed and azimuth, as well as to provide us with extra measurements of rainfall rate. Figure III-5 shows the two WXT510, the reference disdrometer and rain gauge. The first disdrometer was deployed outside of the canopy to provide us with a reference drop-size distribution, while the second disdrometer was deployed beneath the plants to measure the throughfall drop-size distribution and their associated moments, as shown in the right hand side of Figure III-6.

Figure III-7 shows the comparison of the stemflow and the throughfall 1-hour accumulations with the reference rainfall measured outside of the canopy for nine storms occurring between 24 July 2010 and 26 August 2010. The stemflow measurements represent the average accumulation recorded by the two stemflow sensors, to which we applied a linear regression to find the relation shown in equation III-2 with a r^2 of 0.87. As with the stemflow, the throughfall accumulations shown in Figure III-7 are the averages of the two tipping bucket based throughfall sensors. Applying linear regression

to the throughfall and corresponding rainfall led to equation III-3 with r^2 of 0.95. Interestingly, the correlation between the two stemflow sensors, installed on adjacent plants (r^2 of 0.63), was lower than the correlation between the average stemflow sensor and the reference rainfall, which could be due to competition between the two adjacent plants for rain water.

Figure III-5. Instrumentation installed outside of the canopy, including one tipping bucket rain gauge, one optical disdrometer, and two compact weather stations.

Figure III-6. Instrumentation installed under the canopy to capture the direct and indirect throughfall. The left hand side shows a tipping bucket based throughfall sensor. The right hand side shows a disdrometer installed beneath the canopy.
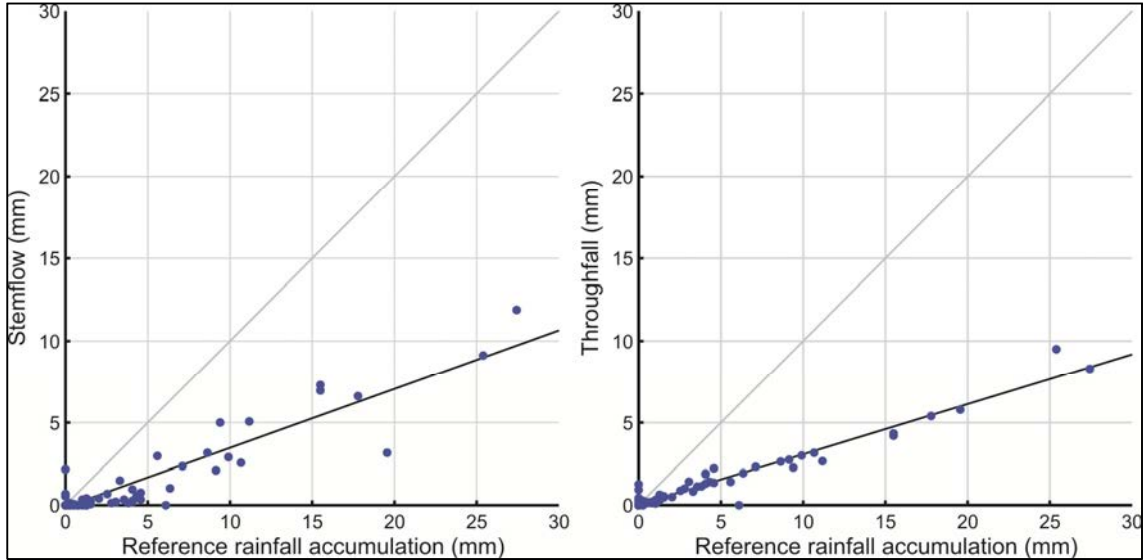
Figure III-7. 1-hour accumulations of stemflow (left panel) and throughfall (right panel) versus rainfall rate outside of the canopy.

$$Stem_{acc} = 0.36 \cdot R_{acc} - 0.11 \qquad \text{(III-2)}$$

$$T_{acc} = 0.30 \cdot R_{acc} - 0.02 \qquad \text{(III-3)}$$

Modification of the kinetic energy flux by the canopy

The two disdrometers, one outside the canopy and the second beneath it, allow us to look into the modification of drop-size distribution and other DSD moments caused by the plants. We analyzed the modification of drop sizes and the diameter-velocity relationship in a maize canopy in Frasson and Krajewski (2011), and we present an extended study in CHAPTER III. Knowing the modification of the drop-size distribution and having measurements of drop velocities allow us to look into the kinetic energy flux beneath the canopy (shown in Figure III-8), a useful parameter in erosion studies.

Even though the presence of the canopy decreases the overall kinetic energy flux of the throughfall, the foliage produces well defined dripping points where drops repeatedly impact. Despite the lower kinetic energy of these drops, the repetition might

mobilize soil particles, which can then be carried by runoff. A discussion of the formation of well-defined dripping points follows in CHAPTER VI.
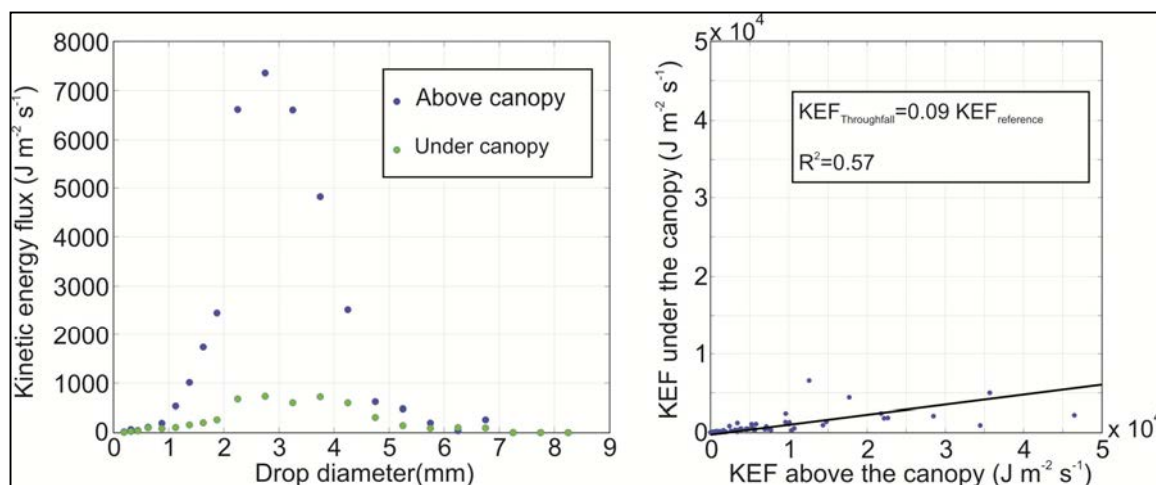
Figure III-8. The left panel shows the contribution of each drop diameter class to the kinetic energy flux above and below the canopy. The right panel shows how the total kinetic energy flux values above and below the canopy are related.

Conclusion

Even though measuring the volume of stemflow and throughfall is not particularly challenging, the interpretation of the data presented here is not straightforward. Ambiguities in the translation from a volume to a "height" of stemflow are evident in the literature, *e.g.* Lamm and Manges (2000) who normalized the stemflow by multiplying the plant spacing by the row spacing, Alves et al. (2001), who used the plant area, and Bussière et al. (2002), who used the stemflow collector area. Our conclusion is that the selection of the stemflow normalizing area depends on the application of this measurement. While using the plant area extracted from the top view of the canopy allows the comparison of the stemflow collected during different stages of development of the canopy, the use of this area does not yield measurements that are readily comparable to the rainfall above the canopy and the throughfall beneath them.

CHAPTER IV.

CHARACTERIZATION OF THE DROP-SIZE DISTRIBUTION AND

VELOCITY-DIAMETER RELATIONSHIP OF THE THROUGHFALL

UNDER A MAIZE CANOPY

<u>Introduction</u>

The interception and partitioning of rainfall by crop canopies is the focus of works such as Haynes (1940), where the author measured stemflow and throughfall totals and noticed a reduction in the volume and energy of rainfall reaching the ground under different crop canopies. Due to these works' potential implications for agricultural praxis (Steiner et al., 1983), the hydrological cycle, leaching of chemicals (Parkin and Codling, 1990), and others, further studies centered on the generation of stemflow followed, and equations to predict the stemflow based on plant geometry and rainfall intensity or accumulation became available. Notable examples include de Ploey (1982), van Elewijck (1989a), and van Elewijck (1989b), and other works summarized in the literature review published by Levia and Frost (2003), which also includes studies developed under forest canopies.

Works incorporating throughfall measurements under crop canopies are also available, *e.g.*, Paltineanu and Starr (2000), who measured stemflow, throughfall and soil moisture under a maize canopy, Bussière et al. (2002), who described a stemflow and throughfall model based on the three dimensional architecture of a maize canopy and contrasted it to experimental data, and Bassette and Bussière (2005), who extended the model to banana plants. Throughfall generation in forests was also extensively studied, as described in the literature review published by Levia and Frost (2006). More recently Muzylo et al. (2009) published a comprehensive review of currently available rainfall interception models.

However, the interception of rainfall by crop canopies changes not only the amount of water reaching the soil but also the velocity and size distribution of the drops that reach the ground. Consequently, understanding the mechanics of soil water recharge, or soil erosion, under canopies requires knowledge of the partitioning of rainfall into stemflow, throughfall, and plant water storage and necessitates our ability to measure the sizes and velocities of hydrometeors under the plants.

Motivated by a desire to understand soil erosion processes under agricultural canopies, Quinn and Laflen (1983) employed the filter paper technique to examine the drop-size distribution (hereafter DSD) under a maize canopy subjected to simulated rainfall. Subsequently utilizing a photographic method to measure drop velocities, the authors were able to calculate the kinetic energy flux under the canopy and assess the throughfall erosivity. Nevertheless, the authors stated that they could have overlooked the importance of dripping when they assessed the erosion potential under a maize canopy.

Still, soil erosion under crop canopies was not fully understood, as noted by Morgan (1985), since he could not explain why the soil detachability increased with canopy cover or determine under what circumstances it occurred. More recently, Bui and Box (1992) investigated the partitioning of simulated rainfall into stemflow and throughfall and their impact on erosion under the maize and sorghum canopies. The authors suggested that the importance of the stemflow was negligible compared to that of throughfall and dripping on soil erosion, which justified further studies of the modification of rainfall characteristics by the canopies.

Armstrong and Mitchell (1987) investigated the DSD under crop canopies, more specifically mature soybeans under simulated rainfall, and Brandt (1989) used the filter paper technique to observe throughfall DSD under trees. These pioneering works allowed the development of empirical predictive models of the DSD under canopies such as Brandt (1990).

Since then, observation methods evolved and researchers moved to automated drop detection and measuring techniques to examine the modification of rainfall characteristics by tree canopies, *e.g.* the works by Hall and Calder (1993), Nanko et al. (2004), Nanko et al. (2006), and Nanko et al. (2008). Subsequently, more modern models of the modification of the DSD by canopies became available, such as the two layer stochastic model byCalder (1996) and Calder et al. (1996). Alternatively, Bassette and Bussière (2008) presented the results of laboratory experiments investigating the influence of leaf inclination, drop size, fall velocity, and water properties on the generation of splashing and water storage in banana trees. Such studies were not extended to popular crops such as maize despite their considerable land cover.

Our work analyzes the modification of rainfall characteristics by a maize canopy, based on storms recorded by two optical laser disdrometers, and offers possible explanations for the modifications of the drop-size distribution and the drop diameter-velocity relationship caused by the canopy. We begin with a description of the experimental site and instrumentation and then offer an interpretation of the observed data. We conclude with the implications of the observed phenomena for soil erosion and remote sensing of vegetation and soil moisture.

Materials and methods

Experimental setup

The experimental site was located in Shueyville, Iowa (41º51'40.15"N, 91º38'42.45"W) in a field containing maize plants (Pioneer 36V75Hx, RR_2) that were planted on 24 April 2009. The plant density was 7.5 plants per square meter, which translates to an average row distance of approximately 940 mm and an in-row distance of 140 mm. The 12 studied storms, summarized in Table IV-1, transpired between 14 July 2009 and 28 August 2009, when the plants were fully developed and before they began to dry out. The experimental setup included two optical disdrometers (laser precipitation

monitor, hereafter LPM), one rain gauge, two modified tipping-bucket rain gauges, and two compact weather stations, which we employed to measure the two-dimensional wind velocity. We detail the instrumentation layout in Figure IV-1.

Table IV-1. Summary of the 12 studied events.

Date	Duration (hours)	Rainfall accumulation (mm)	Throughfall accumulation (mm)	Wind speed (m/s)	Wind direction (degrees)
21 July	17	50.6	5.4	1.1	31
24 July	2	57.6	12.8	1.8	325
03 August	2	1.8	0.2	1.8	225
07 August	6	49.8	6.4	0.6	102
08 August	3	1.3	0.3	0.8	65
09 August	7	40.4	6.6	1.2	274
13 August	2	22.4	11.0	1.0	128
16 August	8	33.3	11.4	2.0	186
17 August	3	10.6	2.3	1.3	196
19 August	5	21.3	7.6	1.2	168
20 August	4	11.4	2.5	1.0	214
26 August	27	162.9	34.2	1.4	59

Note:Storm duration reflects the number of consecutive hours registering at least 0.1 mm h^{-1} of rainfall. Wind speed shows the average speed for the whole event. Wind direction is measured in degrees in the clockwise direction from the north.

Measuring the throughfall

We installed a pair of LPM optical disdrometers, one outside of the canopy to observe unmodified rainfall and a second instrument under the plants, to sample the throughfall. Optical disdrometers can observe the fundamental aspects of rainfall, measuring drop diameters and falling velocities. With this information, one can calculate many characteristics of rainfall, including several moments of the drop-size distribution

such as kinetic energy flux, rainfall rate, optical extinction, or radar reflectivity, as explained by Steiner and Smith (2000) and others.

The LPM disdrometer consists of a laser source, two sets of lenses, a receiver, and a digital signal processing unit (DSP). The laser emitter shoots an infrared beam into a first set of lenses that shapes it into a laser sheet 0.75 mm tall and 20 mm wide. This light sheet extends for 228 mm before reaching the second set of lenses, which converge the beam into the receiver's photodiode and defines the instrument's sensing volume. A drop obscures a fraction of the beam when it enters the LPM's sensing volume, which leads to a decrease in the voltage generated by the receiver's photodiode. The DSP monitors the photodiode's voltage and uses the minimum registered voltage observed during the passage of the drop to calculate the drop diameter. For more details, refer to Thies Clima (2007) and for an assessment of the LPM's performance, refer to Frasson et al. (2011), Lanza and Vuerich (2009) and Lanzinger et al. (2006).
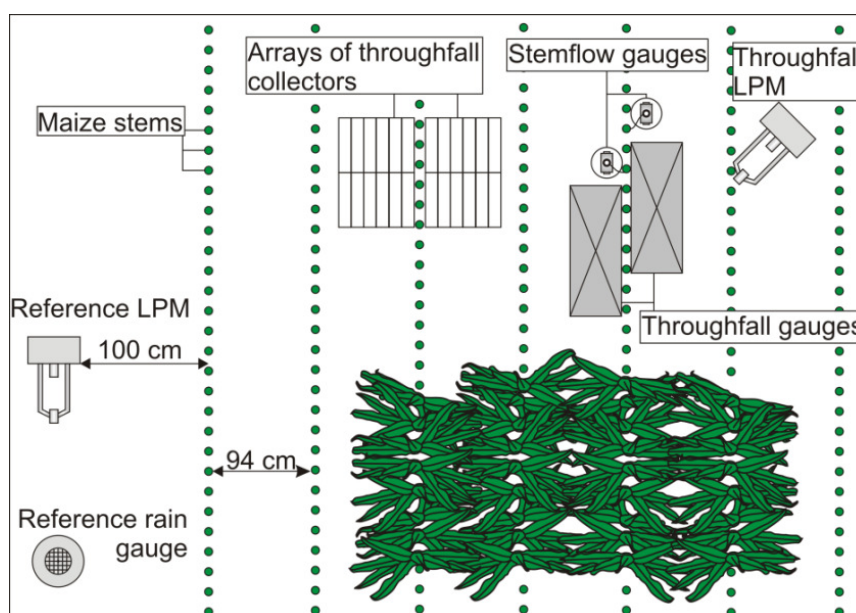
Figure IV-1. Instrumentation layout showing the location of the pair of disdrometers (Reference LPM and Throughfall LPM) along with other instruments installed in Shueyville, Iowa from 08 July 2009 to 01 October 2009.

Computing the drop-size distribution

The drop-size distribution gives the frequency distribution of drop sizes per unit volume of air, usually measured in mm^{-1}m^{-3}. The disdrometer data collected for this work uses equation IV-1 to calculate the drop-size distribution for time resolutions greater than one minute. In equation IV-1, $N(D_i)$ stands for the drop-size distribution corresponding to the diameter class i, n_{ij} represents the number of drops on the diameter class i and velocity class j, A stands for the catchment area of the disdrometer, t for accumulation time, v_j for the central velocity of the velocity class j, and ΔD_i for the width of the diameter class i.

$$N(D_i) = \sum_{j=1}^{20} \frac{n_{ij}}{A \cdot t \cdot v_j \cdot \Delta D_i} \tag{IV-1}$$

Evaluating the canopy coverage factor

The canopy coverage, *i.e.* the fraction of the ground surface covered by plants when the canopy is projected into a horizontal plane, is one of the driving factors of the partitioning of rainfall into direct and indirect throughfall. We evaluated the canopy coverage using digital pictures taken from the top of the canopy, *e.g.* Figure IV-2, approximately a meter above the tassel. We manually traced polygons covering the visible areas of soil and calculated the ratio of the canopy to the total picture area. We evaluated the canopy coverage in two places, one directly above the throughfall disdrometer where the canopy covered 91% of the ground area and a second location above the throughfall collectors, where the canopy covered 88% of the soil surface.

Results and discussion

Modification of the drop-size distribution by the canopy

During the entire experiment, 5.8 million drops were detected by the LPM installed outside of the canopy, while the disdrometer installed under the canopy registered 2.7 million drops, predictably showing that the foliage coverage reduces the

overall number of drops detected at ground level. However, the decrease in the number

of drops is not uniform with respect to the diameter. The solid blue line featured in

Figure IV-3 reveals how the ratio between the counts of drops under and outside of the

canopy changes with respect to the central diameter of each size class. The observed

ratio curve indicates an overall decrease in the number of drops for all but one of the

diameter classes.

Figure IV-2. Top view of the canopy used to evaluate the canopy coverage. This picture
was taken approximately 1 m away from the highest point of the tallest plant
directly above the throughfall LPM. The gap fraction associated with this
picture was 8.8%.

The increased count of drops on the throughfall occurred for the diameter class

with sizes ranging from 4 mm to 4.5 mm. We analyzed the forces acting on the water

droplets on the edges of a leaf for two idealized cases in order to understand what could

cause a peak in the count of drops of a single diameter class. We assumed only two

forces acting on the drop, the weight forcing the detachment of the drop and the surface

tension counteracting it. In the first situation, we approximated the shape of the growing

drop to a perfect sphere and the length of the contact between the drop and the leaf to

equal the drop diameter. For the second case, we imagined a semi-sphere growing on the

bottom of the leaf with a contact length equivalent to the perimeter of the circle formed in the intersection of the semi-spherical drop and the leaf surface.
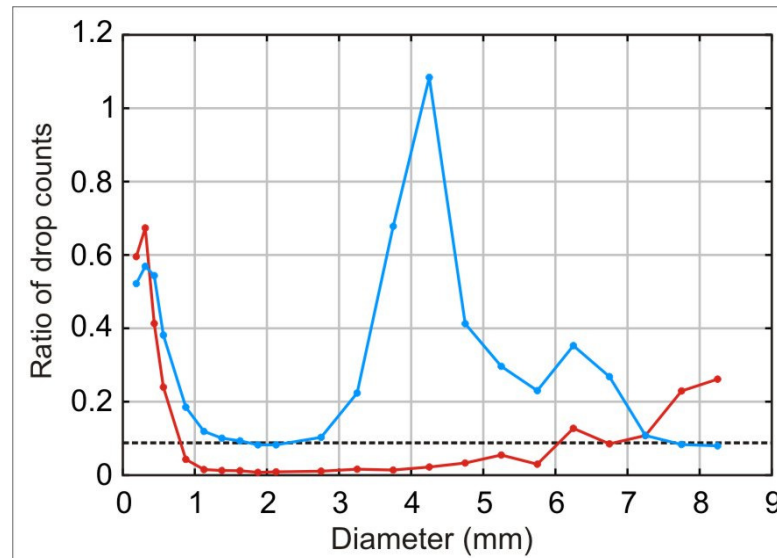
Figure IV-3. Modification of the total number of drops per diameter class by a maize canopy. The solid blue line shows the ratio of the number of drops recorded in the throughfall and the corresponding number observed outside of the canopy for each of the diameter classes. The red line shows the fraction of drops detected outside the canopy that were traveling with velocities under the attachment threshold. The dashed line shows the gap fraction (0.088).

Figure IV-4 shows three examples of drops still attached to maize leaves. The left and middle panels support the assumptions of the first case, where a spherical drop forms on the edge of a leaf and has an attachment length correspondent to approximately the drop diameter. The assumptions about the geometry of the drop and how it attaches to the plant led to equations IV-2 and IV-3, where W stands for the weight of the drop, w the density of water, g represents the acceleration of gravity, D the drop diameter, S the adhesion force resulting from the surface tension, and   stands for the surface tension of water against air. Finally, equations IV-2 and IV-3 allow the calculation of the drop diameter with equation IV-4.

$$W = \frac{\rho_w \cdot g \cdot \pi \cdot D^3}{6} \tag{IV-2}$$

$$S = \sigma \cdot D \tag{IV-3}$$

$$D = \sqrt{\frac{6 \cdot \sigma}{\rho_w \cdot g \cdot \pi}} \tag{IV-4}$$

Figure IV-4. Examples of drops attached on leaves. The left and the middle panels show droplets detaching from the edges of leaves with approximately spherical shapes and attachment lengths similar to the drop diameter. The panel on the right shows an approximately semi-spherical drop attached to the bottom of a leaf. Figures reproduced from Frasson (2007).

The right side panel of Figure IV-4 illustrates the second case, where a semi-sphere adheres to the bottom of a leaf with a contact length equivalent to the circumference of the surface formed by the intersection of the drop and the leaf. These assumptions lead to a volume equivalent diameter described by equation IV-5.

$$D = \sqrt[3]{\frac{1}{2}} \cdot \sqrt{\frac{12 \cdot \sigma}{\rho_w \cdot g}} \tag{IV-5}$$

Numerically, for water at 25°C, $\rho_w = 997$ kg/m^3, $\sigma = 72$ mN/m, and $g = 9.81$ m/s^2, equation IV-4 leads to a diameter of 3.75 mm and equation IV-5 to 7.46 mm.

When we compare the range of drop sizes with higher throughfall counts to the estimated drop detachment threshold from equation IV-4, we see that the increased count

of drops on the throughfall occur one diameter class above the estimated minimum detachment diameter of 3.75 mm. However, the counts of throughfall drops with sizes between 3.5 mm and 4 mm experienced a dramatic increase with respect to the smaller diameter classes, indicating that despite the simplicity of our calculation and the strength of the associated assumptions, there is consistency with the experimental data.

Passing the peak of 4.25 mm, the ratio rapidly decreases as diameter increases, which could reflect a lack of opportunity for extra drop growth. However, the ratio of drops under and above the canopy for the next three subsequent diameter classes remains higher than the corresponding ratio for drops with diameters larger than 1 mm and smaller than 3 mm. To better understand the mechanisms of drop growth, let us look at the sequence of events following the moment a drop hits the foliage.

Intercepted raindrops can remain stationary, run towards the stem of the plant, or run towards the edge of a leaf. One mechanism of drop growth occurs when drops, while traveling on a leaf, make contact with other drops and sometimes merge. After multiple drops coalesce, the result is a single, larger drop. The incorporation of a stagnant drop into a moving one or the merging of two moving drops, can occur in drops of any size.

When combined drops reach the edge of the leaf, they fall if they are heavy enough to detach and either travel to the ground level and become detected by the disdrometer or get intercepted by a lower leaf where they can again turn into stemflow or throughfall or else remain stagnant on the leaf. Drops that reach the leaf edge but are not heavy enough will not detach unless they grow or the canopy is disturbed, *e.g.* they are shaken loose by a gust of wind and are therefore less frequently seen on our data.

The relationship between gusts of wind and the number and size distribution of drops in the throughfall is still an open question. We measured the wind speed and azimuth with the aid of a compact weather station and intend to use our measurements to further explore this problem. This analysis, however, is outside of the scope of the present work and will be discussed at another time.

The number of drops with diameters larger than 1 mm and smaller than 3 mm in the throughfall represented 10% of the number of drops of corresponding diameter recorded outside the canopy. Canopy coverage offers a possible explanation for this ratio.

Simplistically, if we assume that raindrops fall vertically and are uniformly distributed in space, the fraction of raindrops intercepted by the canopy would coincide with the canopy coverage. If such a scenario were true, the direct throughfall would correspond to the gap fraction given by equation IV-6, where G stands for the gap fraction and C for the canopy coverage. Using Figure IV-2, we calculated the canopy coverage immediately above the throughfall disdrometer and used equation IV-6 to evaluate the gap fraction, which was approximately 9%.

$$G = 1 - C \tag{IV-6}$$

With respect to our data, the percentage of drops with diameters from 1 mm to 3 mm that reached the ground was slightly greater than 10%. Interestingly, even though drops with diameters larger than 7 mm are rare in rainfall, we found a similar ratio, 9%, of their counts in the throughfall with respect to their count in the rainfall. The proximity to the measured gap fraction, indicated in Figure IV-3 by the horizontal dashed black line, indicates that most of the drops with diameters inside these two ranges should come from direct throughfall. This supports the drop weight threshold presented earlier in which small drops do not detach unless the canopy is disturbed and large drops have less opportunity to grow and are therefore less frequent in indirect throughfall.

Another interesting feature of Figure IV-3 is the relatively high ratio (55% on average) of drops with diameters ranging from 0.125 mm to 0.5 mm in the throughfall with respect to their numbers in the rainfall outside of the canopy. A possible explanation for this high ratio is that drops of such diameters, even when traveling with terminal fall velocity, do not have enough energy to adhere to the maize leaf.

Depending on their kinetic energy at the instant of impact, droplets may bounce, adhere to, or run on a leaf's surface. Nosonovsky and Bhushan (2008) studied the impact of water droplets on hydrophobic surfaces, focusing specifically on energy barriers that could define whether or not a drop would adhere to the surface after impact. They stated that if the impact time is short, a thin film of compressed air could form between the surface and the drop, preventing the wetting of the surface. However, if the kinetic energy is high enough to overcome the free surface energy, the drop might adhere to the leaf. Equation IV-7 explains the relationship between the free surface energy (E_{surf}), the drop diameter (D), and the surface tension ( ), in our case between air and water. The kinetic energy of the drops is given by equation IV-8, where E_{kin} stands for the kinetic energy, D for the drop diameter, $_w$ for the density of water, and v for the drop velocity.

$$E_{surf} = \pi \cdot D^2 \cdot \sigma \qquad \text{(IV-7)}$$

$$E_{kin} = \frac{\rho_w \cdot \pi \cdot D^3 \cdot v^2}{12} \qquad \text{(IV-8)}$$

The combination of equations IV-7 and IV-8 leads to the velocity limit, as seen in equation IV-9:

$$V = \sqrt{\frac{12 \cdot \sigma}{\rho_w \cdot D}} \qquad \text{(IV-9)}$$

Comparing velocity limits calculated with equation IV-9 to the Gunn and Kinzer terminal fall velocity curve (Gunn and Kinzer, 1949), we observe that drops with diameters smaller than 0.378 mm that are falling at their expected terminal fall velocity should not attach to the plant and should instead roll on its surface. Such drops fall on the first three diameter classes, *i.e.* 0.125 mm<D≤0.25 mm, 0.25 mm< D ≤0.375 mm, and 0.375 mm< D ≤0.5 mm, leading to an increase in the drop count ratio. This is consistent with the data presented in Figure IV-3.

However, not all rain drops travel at terminal fall velocity, as determined by Montero-Martinez et al. (2009). To account for the velocity distribution of raindrops, we

compared the measured drop velocities to the calculated drop attachment threshold and computed, for each diameter class, the fraction of drops with velocities lower than this threshold. The red solid line in Figure IV-3 shows the computed fraction of different diameters of drops that are not expected to attach to the leaves.

Comparing the ratio of drops that are not expected to attach to the canopy to the drop count ratio of throughfall to rainfall drops; we see that the magnitude and shape of the two curves are quite similar for diameters less than 2.5 mm. This indicates that the lack of kinetic energy necessary to promote attachment of drops to the foliage could be one of the sources of small drops, *i.e.* droplets that are not heavy enough to separate from the leaves and should otherwise not be present in the throughfall proportions higher than the gap fraction.

The uneven canopy blocking efficiency causes an increase in throughfall median volume diameter (D_{50}). While the D_{50} computed outside of the canopy for the duration of the experiment was between 2.5 mm and 2.75 mm, with the diameter of 2.75 mm corresponding to the 57th percentile, the median volume diameter observed under the canopy was approximately 3.75 mm. Our median volume diameter was higher than that found by Armstrong and Mitchell (1987), who reported a throughfall D_{50} of 3.1 mm under a maize canopy. However, their plants were exposed to simulated rainfall with D_{50} of 2 mm, which is smaller than the median volume diameter of natural rainfall that we recorded for the duration of this experiment. The increase of the throughfall D_{50} is not exclusive to a maize canopy. It has also been reported for other vegetation types from soy bean cultures to trees (Armstrong and Mitchell, 1987; Brandt, 1989; Hall and Calder, 1993; Nanko et al., 2006).

Thus far, we have discussed modification of the counts of drops. However, a more frequently used measurement of drop diameter distribution pertains to the concentration of drops per diameter and volume of air, which leads to the unit of $mm^{-1}m^{-3}$. From this quantity, one can calculate all other rainfall moments, such as

rainfall rate, kinetic energy flux, and the radar reflectivity factor. Figure IV-5 compares the drop-size distribution under and outside the canopy. Similarly to what we observed when comparing counts of drops on the throughfall and rainfall, we observed ranges of diameters in which the canopy more successfully decreased the concentration of drops and ranges where the concentration increased on the throughfall.

The disagreement between the Marshall and Palmer distributions and the rainfall and throughfall DSDs is not surprising as the drop-size distributions presented here are averages of 12 storms, some characterized by low rates and longer duration and others by higher rates and shorter duration. We present them for reference.
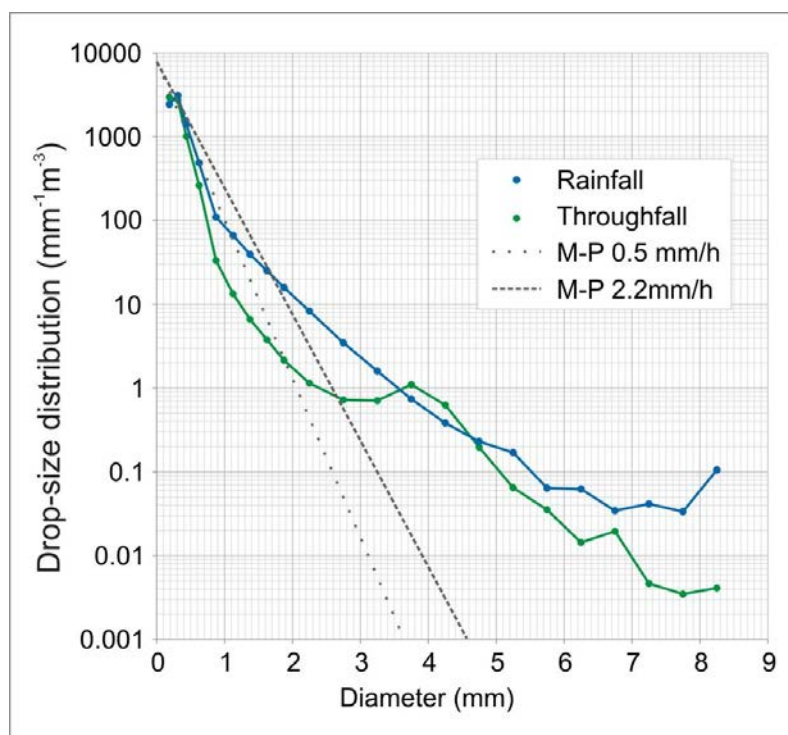
Figure IV-5. Comparison of the drop-size distribution (DSD) outside of and under the canopy. The DSDs shown here are averages of 12 recorded storms. We included only hours when the detected rainfall exceeded an accumulation of 0.01 mm, leading to an average rainfall rate of 2.2 mm h^{-1} outside of the canopy and an average throughfall rate of 0.75 mm h^{-1}. The dotted and dashed lines show the Marshall and Palmer distributions (Marshall and Palmer, 1948) for rainfall rates of 0.75 mm h^{-1} and 2.2 mm h^{-1}, respectively.

Figure IV-5 shows that drops with diameters smaller than 0.25 mm and those with diameters between 3.5 mm and 4.5 mm are present in higher concentration on the throughfall than on the rainfall, whereas Figure IV-3 shows increased counts only for drops with diameters between 4 mm and 4.5 mm. Initially, this appears to indicate error, but the cause for this apparent discrepancy lies in the normalization of the drop counts per volume of atmospheric air. The volumetric concentration of drops is calculated by associating each drop with a volume of air that equals the sampling area of the instrument multiplied by height, which is defined by the velocity of the drop multiplied by the integration interval. Drops falling from maize leaves might not have enough time to develop terminal fall velocity. Slower drops are associated with smaller volumes, which reflect in the DSD as higher concentrations. To ground this assumption, we examine the modification of the drop velocity-diameter relationship by the canopy in the next section.

Modification of the drop velocity-diameter relationship by the canopy

In the previous section, we hypothesize that indirect throughfall causes the increase in the number of drops under the canopy with diameters between 4 mm and 4.5 mm. To support this hypothesis, we consider the velocity-diameter relationship of the throughfall and its relationship to measurements of unblocked rainfall. Figure IV-6 presents two plots of raw disdrometer data, which consist of counts of drops in each one of the 440 classes (22 diameter and 20 velocity classes). To aid the visualization, we plot the logarithm of the number of drops on a color scale, where hotter colors represent higher numbers and white stands for no drops detected in that class. The solid line shows the Gunn and Kinzer (1949) terminal fall velocity curve based on experimental measurements of drops falling in still air.

Comparing the two panels in Figure IV-6, we notice that the throughfall shows not only fewer drops but also a distinct family of drops with diameters between 3 mm and

5 mm and relatively low velocity. To aid the visualization of this family of drops, we include Figure IV-7 to represent only the drop classes with increased counts under the canopy.
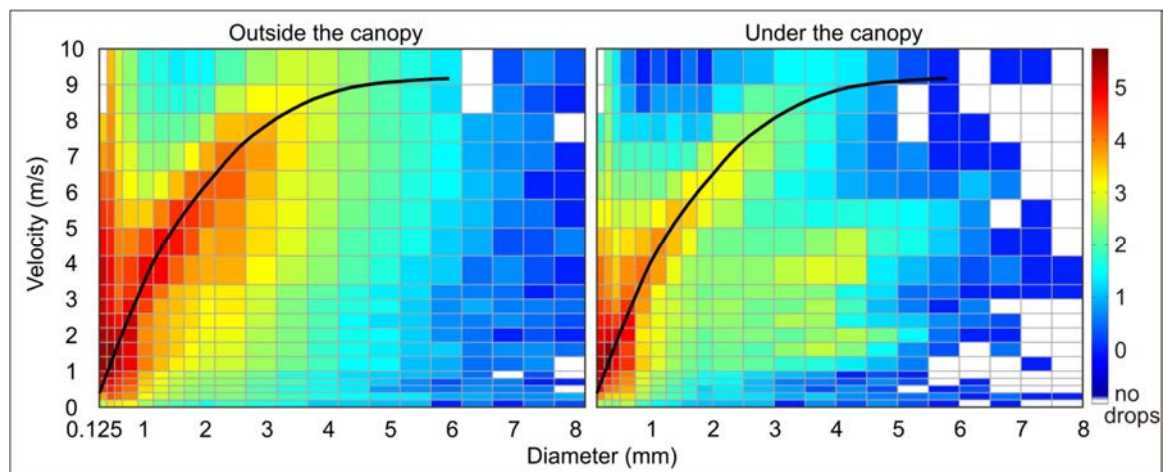
Figure IV-6. Relationship between diameter and velocity of raindrops observed outside and under the canopy. Identical color schemes for both panels represent the logarithm of the count of drops inside each diameter (horizontal bins that range from 0.125 mm to 8 mm) and velocity (vertical bins that range from 0 m s^{-1} to 10 m s^{-1}) classes. The solid curves show the Gunn and Kinzer terminal fall velocity curve.

In Figure IV-7, we assign white for classes with fewer drops in the throughfall. The remaining classes feature increased drop counts in the throughfall. For these classes, we color-coded the logarithm of the difference in counts for each class of the throughfall and rainfall and set the color scale to match the scale of the other two panels. The six lower solid curves represent the velocity curves computed for each drop diameter using the methodology described by Wang and Pruppacher (1977) after a fall of 0.3 m, 0.5 m, 1 m, 1.3 m, 2 m, and 3 m, respectively. The seventh curve shows the Gunn and Kinzer terminal fall velocity curves in still air.

From a total of 440 classes, 24 displayed higher counts under the canopy. Considering this subset of 24 classes, we can identify two families of drops. The first is made up of small drops (diameters between 0.125 mm and 0.250 mm) falling at near terminal velocity, and the second is composed of larger drops (diameters ranging from 3 mm to 6 mm) falling with speeds considerably lower than the terminal velocity. Even though the small, fast moving drops are falling at near terminal fall velocity, they could still originate from the canopy. Due to their relatively low terminal velocity, even a fall height of 0.30 m is sufficient for them to reach terminal velocity, which prevents us from locating their origin.

Figure IV-7. Classes of drops experiencing higher counts on the throughfall. White bins stand for either no detected drops or for classes with higher counts outside of the canopy. The color coded classes show the logarithm of the difference between throughfall and rainfall counts. Solid curves represent the velocity distribution of drops after a fall of 0.3 m, 0.5 m, 1 m, 1.3 m, 2 m and 3 m (Wang and Pruppacher, 1977) and the terminal fall velocity after Gunn and Kinzer (1949).

From a total of 440 classes, 24 displayed higher counts under the canopy. Considering this subset of 24 classes, we can identify two families of drops. The first is made up of small drops (diameters between 0.125 mm and 0.250 mm) falling at near terminal velocity, and the second is composed of larger drops (diameters ranging from 3 mm to 6 mm) falling with speeds considerably lower than the terminal velocity. Even though the small, fast moving drops are falling at near terminal fall velocity, they could still originate from the canopy. Due to their relatively low terminal velocity, even a fall height of 0.30 m is sufficient for them to reach terminal velocity, which prevents us from locating their origin.

Due to the larger diameters found in the second group of drops, the distance to reach terminal velocity is of a higher order of magnitude than the expected height of a maize canopy. For example, a 3 mm rain drop could require a fall of more than 13 m to reach 99% of its terminal velocity (Wang and Pruppacher, 1977). Consequently, their velocity at the throughfall disdrometer level (approximately 0.25 m above the ground) offers insight into the height from which drops could have originated. For instance, all classes of drops displaying higher counts on the throughfall with diameters between 3 mm and 5.5 mm have velocities that are compatible with fall heights ranging from 0.3 m to 1.3 m (with respect to the disdrometer level, or 0.55 m to 1.55 m with respect to the ground level), which are within the maize leaf heights listed in Table IV-2. This finding supports the claim that the peak shown in Figure IV-3 was caused by drops dripping from the leaves.

The higher counts of drops with diameters ranging from 3.5 mm to 4 mm traveling with lower than terminal fall velocity also supports the claim that the higher throughfall DSD of drops with a central class diameter of 3.75 mm resulted from their lower velocity. Despite the overall lower count of this class of drops (throughfall counts accounted for only 67% of corresponding numbers registered outside of the canopy), they were present in higher concentration under the canopy. The classes with lower velocities

have smaller associated volumes, leading to a higher drop concentration than is seen in higher velocity classes even at identical counts. The skew in the drop velocity distribution of the throughfall at this diameter class was enough to overcome its lower number of drops, leading to the observed increase in the drop-size distribution.

Table IV-2. Heights of leaves with respect to ground level.

Leaf	Minimum height (m)	Maximum height (m)
1	0.27	0.46
2	0.31	0.52
3	0.41	0.75
4	0.53	0.79
5	0.65	1.03
6	0.78	1.16
7	0.94	1.57
8	1.11	1.60
9	1.27	1.75
10	1.45	1.95
11	1.61	2.23
12	1.79	2.15
13	1.99	2.39

Note: The minimum and maximum heights measured from a three dimensional digital model of a plant were located in the neighborhood of the disdrometer. The disdrometer's measurement volume was located at a height of approximately 0.25 m. We removed the first layer of leaves from the plants next to the LPM in order to avoid beam blockage and instrument malfunction. The three dimensional digital model of the plant was created according to the methodology described by Frasson and Krajewski (2010).

Conclusion

A pair of disdrometers, one installed under and a second installed outside of a maize canopy, allowed us to look at the distribution of sizes and velocities of raindrops that constituted the throughfall as well as at their modification caused by the plant's

foliage. We identified four distinct regions by plotting the ratio of the counts of drops for the 22 different diameter classes registered under the canopy with respect to the corresponding counts observed outside of the canopy.

The first region entails drops with diameters ranging from 0.125 mm to 0.5 mm in which the number of throughfall drops accounted for 55% of the numbers registered outside of the canopy. While splashing could have generated some of these droplets, the number and size of droplets present on the throughfall was consistent with the fraction of droplets recorded outside of the canopy that were traveling with kinetic energy lower than the attachment threshold described by (Nosonovsky and Bhushan, 2008). We showed that drops with such diameters, even when traveling at their terminal fall velocity, do not have enough energy to adhere to the leaf and should roll from its surface.

The second region contains drops with a diameter ranging from 0.5 mm to 3 mm, where drops have enough energy to adhere to the leaves and, according to our simplified calculations, are not heavy enough to detach after they reach the edge of a leaf. Their ratio in the throughfall was slightly higher than the canopy gap fraction, indicating that drops with such diameters are most likely part of the direct throughfall.

A third region comprises drops with diameters between 3 mm to 5.5 mm. In this region, the number of drops recorded under the canopy, divided by the corresponding counts outside of the plant coverage, was larger than the canopy gap fraction, with one of the diameter classes (4 mm to 4.5 mm) showing a higher count in the throughfall. This observation is consistent with the simplified calculation of the drop detachment threshold based on the comparison of the drop weight and the surface tension formed on the interface of the water-air-leaf. Past this point, we identified a fourth and final region, where the ratio again slowly converges to the gap fraction. The comparison of drop velocity measurements to drop velocity estimations shows that the drops featuring increased counts on the throughfall originated from heights compatible with a maize canopy.

Knowledge of the throughfall drop-size distribution is one of the initial steps in the mechanistic modeling of soil erosion and the recharge of soil moisture under crop canopies. While the overall number of drops is lower under the foliage, about 46% of the observed number of drops registered outside the canopy during the present study, they are generally larger (D_{50} of 3.75 mm on the throughfall in contrast to less than 2.75 mm outside of the canopy) and slower (refer to Figure IV-7), affecting the way in which throughfall drops interact with soil particles. Knowledge of the concentration of drops and their size distribution on the throughfall is also important in the future development of microwave-based sensors to measure the evolution of plant water storage and soil moisture during storms. This would allow the separation of the throughfall signature from signals coming from water stored on the vegetation and in the soil.

CHAPTER V.

THREE-DIMENSIONAL MODELING OF A MAIZE CANOPY

Introduction

This chapter outlines the procedures used to create a realistic three-dimensional digital model of a maize canopy that can be used in the simulation of rainfall interception. The procedure entails preparing and photographing plants, creating a digital model of individual leaves, integrating the leaves to form a plant, and finally replicating the model to comprise the full canopy.

We used the commercial short range photogrammetry software PhotoModeler 6 (EOS Systems Inc., 2008a) to create three-dimensional digital models of individual plants, based on pictures and measurements of plants in different stages of development that were taken in the years of 2008, 2009, and 2010.

In 2008, we photographed the same plant at 2 different ages: when the plant had 6 leaves and was 53 cm tall (18 June 2008) and when the fully developed plant had with 10 leaves and was 248 cm tall (16 July 2008). The two models were presented by Frasson and Krajewski (2009) and the proposed procedure published by Frasson and Krajewski (2010). On 20 July 2009, we photographed a fully developed plant (Pioneer 36V75Hx, RR2 cultivar, planted on 24 April 2009) that was 239 cm tall and had 13 leaves. In 2010, we built two more models, the first of a plant that had 7 leaves and was 45 cm tall (29 May 2010) and the second of a plant had 11 leaves, was 200 cm tall, and had ears that were beginning to develop (13 July 2010).

Background

We open this discussion with a review of previous measurement techniques used to describe the geometry of grasses, beginning with the methodology presented by Bonhomme and Varletgrancher (1978). The first stage in their methodology involves determination of leaf width variation, which is accomplished by measuring the width of

various leaves from different plants and grouping them by age and order. In the second stage, plants are cut and photographed against a flat grid, and information on leaf inclination and length is extracted from the photographed silhouettes of the plants. The silhouette method was still used with some modifications in such recent works as España et al. (1998), España et al. (1999a), and España et al. (1999b).

Another measurement technique that captures the three-dimensional structure of plants is called stereo-photography and it consists of simultaneously taking a pair of pictures of the canopy, executing image rectification, and marking and matching points on the modeled objects. As the distance between cameras is known, the positions of the points can be calculated from the rectified images. The rectification process depends on parameters that are unique to the photography setup and that are determined through calibration.

Ivanov et al. (1994) describe an application of stereo-photography in the reconstruction of a maize canopy. They used two synchronized film cameras, fixed on a 7.80 m tall post and positioned horizontally 0.75 m away, to obtain pairs of pictures of maize plants (each 2.50 meters tall with 11 leaves, planted with a 0.8 m separation between rows, and spaced 0.15 m along rows). The pictures were then developed and enlarged to a 18 cm by 18 cm format (a second format of 40 cm by 40 cm was also tested but with no gain in accuracy) and fixed to a digitizing table where the operator marked four to five points per leaf per photograph. The next step involves stereo matching, where the corresponding points on different pictures are linked, allowing the calculation of their coordinates. This method has the disadvantage of only being able to describe the top layers of the plants, as the lower levels are obscured by them.

Ivanov et al. (1995) extended their previous method, enabling them to describe the whole plant canopy by photographing it in stages. In each stage, a set of stereo-photographs captures images of the upper leaves, which are subsequently removed. As the upper leaves are cut from the plant, the layer immediately beneath is revealed and the

process is repeated. However this approach has the disadvantage of being destructive and prohibiting the observation of the plant's development.

More recently, Biskup et al. (2007) developed their own stereo imaging system and showed its applicability by digitizing the upper layer soybean canopy leaves covering an area of 1.20 by 0.80 meter. The idea is similar to that of Ivanov et al. (1994), where two photographs from the canopy are simultaneously taken and corresponding points on each picture are matched, allowing the estimation of their coordinates. The great improvement introduced by this technique is the automatic marking and matching of points, which greatly hastens the process of digitally constructing the plant. However, as with the earlier methodology, only the leaves that are visible to both cameras can be digitized.

Sinoquet et al. (1991) introduced the use of a sonic digitizer and compared it to the silhouette method to estimate the three-dimensional geometry of the maize plant with the intent of studying light interception. The sonic digitizer consists of an emitter that is placed on the point to be digitized and a set of four coplanar microphones fixed at known positions. The distance from the emitter to each of the microphones is calculated as a function of the travel time of the emitted sound and the speed of sound for a given air temperature.

To demonstrate their results, the authors simulated a crop by placing 51 maize plants that were planted in plastic pots in three rows 80 centimeters apart and with an in-row distance of 25 centimeters. They made two observations of their crops: first when the plants had an average of 10.1 visible leaves and again when they had an average of 14.7 leaves using the sonic digitizer and the silhouette method. They found that both methods led to similar estimates for leaf inclination and vertical leaf area density function, but they diverged in the horizontal area distribution. The authors attributed the disagreement to the silhouette's planarity assumption, which overestimates the foliage overlap and thus limits the use of the method.

Bussière et al. (2002) used the same methodology proposed by Sinoquet et al. (1991) to create a three-dimensional model of a maize plant in order to study the partitioning of rainfall by the canopy. They proceeded with the digitizing indoors, as the ultrasonic digitizer is sensitive to wind and is therefore not suitable for outdoor use. They used between 6 and 60 points to describe each leaf, which resulted in a model of an 11-leaf plant containing about 1000 triangles.

Guo et al. (2006) published a work on the optimization and field validation of a model called GREENLAB, which was previously described by Yan et al. (2004). The original GREENLAB model is not plant specific and can use field measurements to optimize the simulation of the geometry of a species. In Guo et al. (2006), a commercially available electromagnetic digitizer was used to digitize the edges and mid-ribs of the leaves and other organs. The digitizer consists of a hand held transmitter, a receiver, and a central unit. Both the transmitter and the receiver have a set of three coils. The coils in the transmitter are fed with alternating current, which creates varying magnetic fields that induce voltages in the coils mounted on the receiver. By measuring the induced voltages, the instrument is able to locate the position and orientation of the transmitter. Other studies that utilized the electromagnetic digitizer were conducted by Sinoquet and Rivet (1997) and Sinoquet et al. (1998).

Chambelland et al. (2008) also used the electromagnetic digitizer in their work, but they found the device too imprecise to delineate leaves. To overcome the instrument's imprecision, Chambelland et al. (2008) employed an electromagnetic digitizer only to capture the leaf position and orientation and while using a laser scan digitizer to derive the leaf geometry. In a third step, the length and curvature of the mid-rib, the maximum leaf width and area, and other geometric parameters were extracted from the images obtained by the laser scan digitizer. In the fourth and final step, the information obtained by both digitizers was combined. They exemplified their procedure by creating a three-dimensional digital model of a beech tree.

Another promising technique for creating three-dimensional models of plants is light detection and ranging (lidar). Omasa et al. (2007) discussed the use of lidar created models for evaluating the response of the plants to environmental changes. Their system could resolve distances with a range accuracy of 0.5mm, and its use was demonstrated by the digitizing of a tomato plant (*Lycopersicon esculentum Mill.*) and an aubergine (*Solanum melongena* L.), both of which are not as tall or complex as a maize canopy. The shortcomings of this technique are similar to the ones presented by stereo-photography. Lidar is also limited by occlusion and requires either the removal of outer leaves after they are scanned or that the scan be taken from multiple locations.

Lidars have also been used to create three-dimensional models of trees. For example, Hosoi and Omasa (2006) used a fine resolution portable scanning lidar, and Omasa et al. (2008) used a combination of airborne and ground-based lidar. More examples can be found in the forestry literature (Hosoi and Omasa, 2007); however, not many are found in the agricultural community, possibly due to the difficulty of employing the system inside a dense crop.

Dornbusch et al. (2007) created an automated method to transform three-dimensional sets of points (point clouds) into plant organs. They created a set of Matlab® scripts able to read point clouds and create architectural plant models composed of triangulated surfaces, with the capability of assigning topological information to each plant organ. To demonstrate their setup, they used a three-dimensional optical digitizer, the Digiscan 2000 (RSI GmBH, Oberuser, Germany), to scan a sample plant (*Hordeum vulgare L.*) and create a three-dimensional model. In principle, their scripts can be applied to point clouds created by other methods such as (ultra)sonic digitizing or lidar.

Recent improvements in the quality and affordability of digital single lens reflex (SLR) cameras along with the availability of commercial photogrammetry software have motivated us to create a more detailed model of a maize plant, one that would be more suitable to the mechanistic modeling of rainfall partitioning by its leaves.

Materials and methods

Creation of three-dimensional models of individual plants
through photogrammetry

Camera calibration

Camera calibration allows the correction of optical distortions present on the photographs. During calibration, the user takes 9 to 12 pictures of the calibration paper from different angles covering as much of the camera sensor as possible. The calibration paper consists of black circles placed on a regular grid of 10 rows by 10 columns or 12 rows by 12 columns and four coded targets placed on the four corners of the paper. We printed a 12 by 12 grid of targets on a 44.2 by 44.2 cm paper and photographed it from a distance of approximately one meter, which is about the same distance held between camera and targets during the field image acquisition.

The photogrammetry package uses this set of pictures to calculate camera and lens parameters, namely the principal point and digitizing scale of the camera corresponding to a certain focal length (EOS Systems Inc., 2008b). The calibration should be done once per each camera/lens setup. If done successfully, it does not need to be repeated for the same setup.

Plant preparation and image acquisition

During this stage, the user attaches coded targets to the leaves and stem of the plant. These targets consist of known geometric shapes printed on white paper, creating distinguishable points on the edges, mid rib, and stem of the plant. During the image processing phase, the photogrammetry software scans the photographs for shapes that match those of the targets. Each coded target has a unique pattern imprinted on the intermediate ring that allows the photogrammetry program to recognize its identity. Targets with known identities are automatically linked between pictures, eliminating the

laborious step of manually matching them. Figure V-1 shows an example of a coded target.
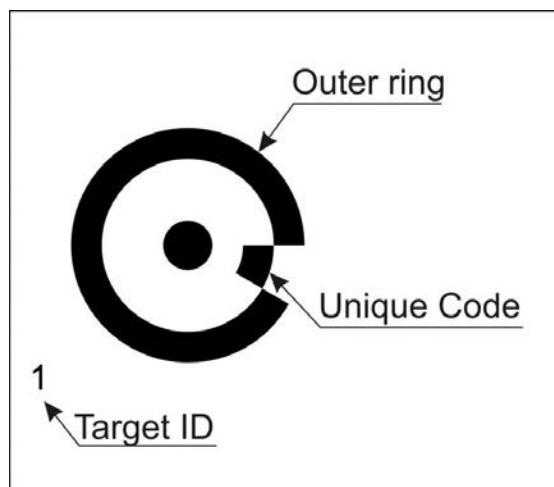
Figure V-1. Example of a coded target created with the PhotoModeler 6 in its most current version as of 11 August 2010. The inner circle is the target itself, the intermediate ring contains the target identity and the outer ring aids the program in finding the target.

For shorter plants, we found that having a grid of targets under the plant allows for quicker image acquisition and processing than placing targets on the stem and leaves. Figure V-2 shows two examples of such photographs. This technique will work when the plants are short enough to be entirely framed in each picture, including the grid of targets under them.

In order to properly calculate the relative position of two pictures, the photogrammetry software requires a number of common reference points between them. Taller plants will not allow the reference grid placed on the ground to be visible in all pictures, making it unfeasible to use the described faster procedure. In the case of tall plants, the targets must be placed on the edges and mid-rib of the leaf currently being digitized, on the stem, and on the immediately inferior and superior leaves. This allows

the user to combine the individual leaf models. Figure V-3 shows an example of a leaf
ready for image acquisition. A sheet with coded targets can still be placed under the
plant to identify the location of the ground.

Figure V-2. 2 of the 18 pictures used in the creation of a three-dimensional digital model
        of a 7-leaf maize plant (29 May 2010).

With the targets in place, the next step is photographing. Pictures must be taken
from multiple angles, with each detail that the user wants to depict present in at least two,
and preferably three, pictures. The PhotoModeler's instruction manual (EOS Systems
Inc., 2008b) suggests a circular pattern as shown in Figure V-4. As the leaves are
digitized individually and combined later, points on other leaves and on the stem must

also be digitized in order to create common points across individual leaf models. These common points are called cross-referencing points and are also shown in a real picture in Figure V-3 and schematically in Figure V-4.

Figure V-3. Leaf ready for image acquisition. (A) points to the mid-rib of the leaf that is currently being digitized, (B) indicates targets on the edges of the leaf and (C) points to targets on other leaves that are used to combine individual leaf models (cross-referencing points). Photography used in the digitizing of the leaves on 13 July 2010.
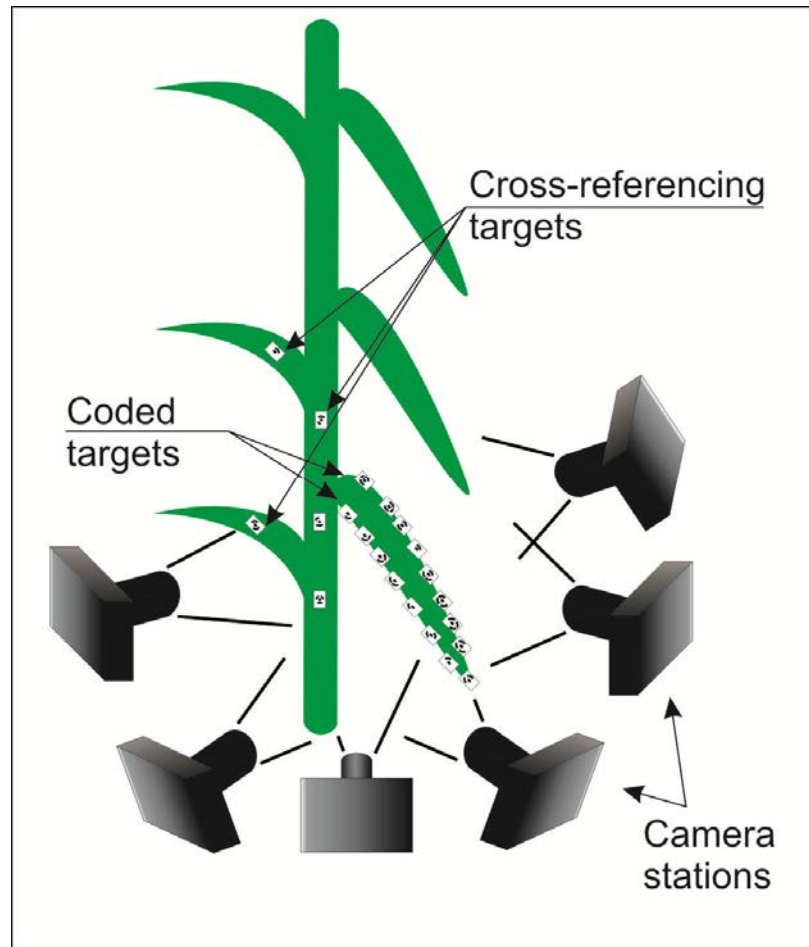
Figure V-4. Illustration of the picture taking pattern, circulating the plant. It is important to ensure that each detail that will be present on the final three-dimensional model can be seen from at least two different angles.

The main purpose of the circular movement around the plant is to ensure good separation angles between camera stations. The separation angle is the angle formed between the line connecting a point being digitized and each of the camera stations from which the point is visible. Points that are solved based on low separation angles are more susceptible to positional errors, as shown in Figure V-5. This scheme illustrates the positional error caused by a distortion of one degree for two cases: the first with a separation angle of 10º and the second with a separation angle of 90º degrees. The

positional error shown in the first case is more pronounced than the corresponding error in the second case.
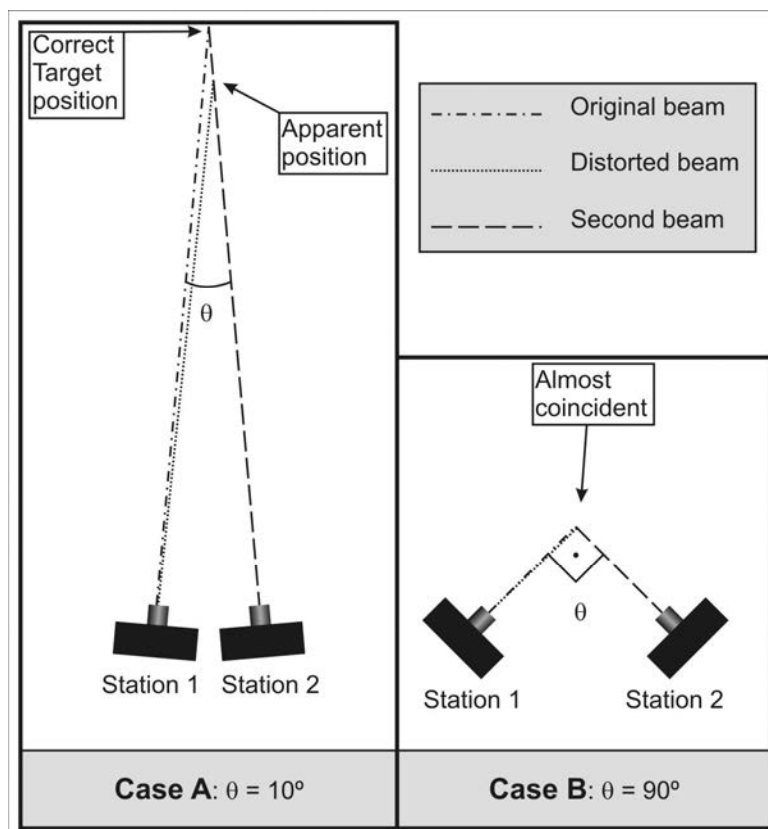
Figure V-5. Comparison of the positional error of a point caused by distortions in the pictures, at two distinct separation angles. This illustrates the importance of maintaining higher angles between stations. Reproduced from Frasson and Krajewski (2010).

The number of pictures necessary to build a model is highly variable. It depends on the level of detail required by the user, the number of leaves on the plant, the camera setup, and the canopy density. Detailing areas that are easily obscured by other elements of the plant, such as leaf attachment points, increase the number of required photographs. The number of leaves is directly related to picture requirements. The more leaves to be digitized, the higher the number of pictures needed in the project. Lenses with a wider

field of view can potentially decrease the number of pictures. Image distortions caused by fish eye lenses can, in principle, be removed by the image idealizing routine included in the photogrammetry software. At this point, however, we have only worked with 28mm (focal length) lenses in a digital camera with a 1.6x crop factor. Finally denser crops limit movements around the plant, which affects the distance that the photographer can be from the currently digitized leaf. This can increase the number of pictures that are necessary. Table V-1 shows the number of pictures, plant heights and number of leaves on each one of the models that we built.

Table V-1. Number of pictures used in the creation of each of the described models and number of leaves and heights of each digitized plant.

Year		2008	2009	2010	
Date	18 June	16 July	20 July	29 May	13 July
Number of pictures	48	119	140	17	68
Number of leaves	6	10	13	7	11
Plant height (cm)	53	248	239	45	200

Digitizing individual leaves

With the pictures taken, the next step is the leaf digitalization. This step consists of importing the pictures into the photogrammetry package, identifying the targets and matching them in the different pictures, calculating the camera orientation, "idealizing" the picture and adding extra details, and finally exporting the results.

This can be the most time consuming stage of the single plant three-dimensional model creation as identification errors can be difficult to spot and can cause the picture orientation procedure to fail. Figure V-6 and Figure V-7 show the most common causes

of identification errors that we encountered while processing the 2008's photographs.
Figure V-6's errors were mitigated by introduction the outer ring (please refer to Figure
V-1), which delimitates the area where the target code is located. If the photogrammetry
package does not see the whole outer ring, it assumes that the target has no specific id
and matching is done manually to avoid identification errors.
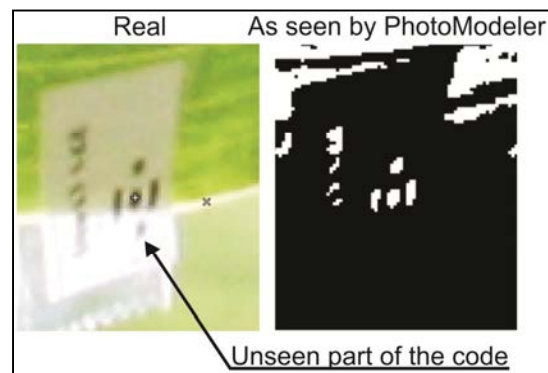
Figure V-6. Identification error due to bleeding of light through the paper. The lack of
contrast between the bar code associated with the target and the paper where it
is printed prevented its correct identification. Reproduced from Frasson and
Krajewski (2010).
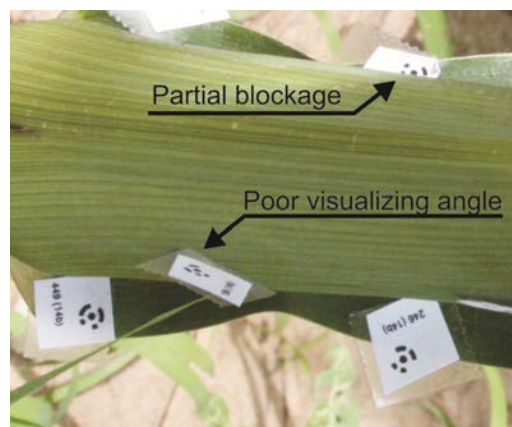
Figure V-7. Identification errors caused by an excess of distortion due to viewing angle
and partial blockage of the code. Adapted from Frasson and Krajewski
(2010).

When at least four points are simultaneously present in two different photographs, the photogrammetry package can attempt to orient the two pictures. Throughout the picture orientation process, the program calculates which relative picture plane configuration produces the arrangement of points displayed in them. The presence of misidentified targets can cause this procedure to fail, or lead to erroneous calculations of the camera orientation. The more unoriented pictures are processed at a time, the harder the identification of errors. Orienting more than four pictures at a time is not recommended (EOS Systems Inc., 2008b).

Once all of the pictures are imported to the photogrammetry program, and oriented, the next step is picture idealization. This procedure reduces distortions caused by the camera lenses using parameters found during calibration. The user can then add extra details, marking points at the edge and mid-rib of the current leaf, until the desired level of detail is achieved. After completion, the points are exported to allow the combination of models and assembly of the whole plant.

Assembling the whole plant

At this stage, the user combines each isolated leaf model, such as the one shown on Figure V-8, with other leaves until the plant is complete. The process involves choosing one leaf to serve as the base model and another leaf to serve as the imported model. The base model is the one that will retain its arbitrary coordinate system, causing the imported model to be rotated and rescaled until its cross-referencing points match the arrangement of the corresponding cross-referencing points present in the base model. A strategy that allows the creation of this study's five models entails working from two fronts, the first beginning with the highest leaf, and the second beginning from the lowest leaf. In the former, the highest leaf (first leaf) is brought into the second leaf and subsequently the two combined leaves are brought into the third leaf. Meanwhile the lowest leaf is brought into the immediately upper leaf. The last combination will merge

the upper and lower sets of leaves, resulting in a complete plant. Figure V-9 shows an example of a combination sequence.
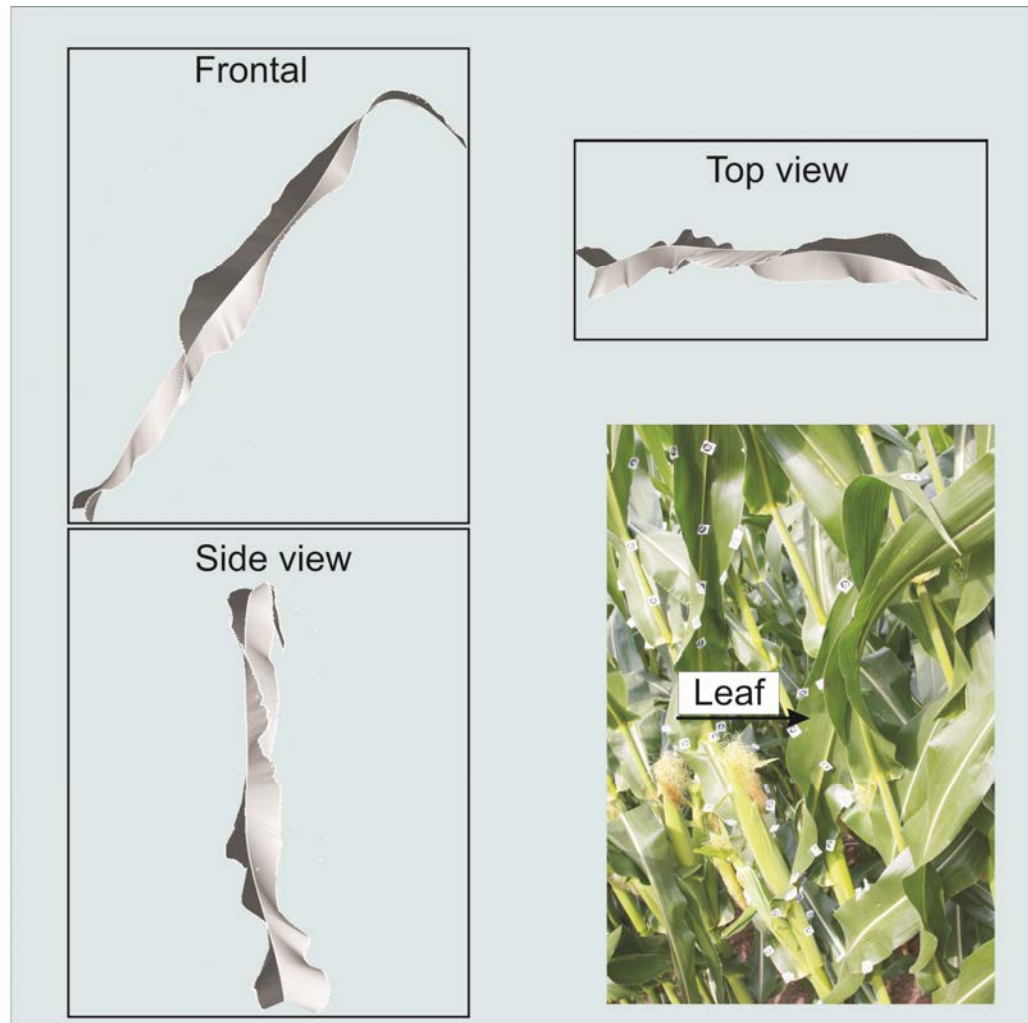
Figure V-8. Example of a completed leaf.

Once the plant is complete, it is time to adjust the model's coordinate system to match meaningful directions and real world measurements. The photogrammetry model provides a routine for axis rotation. It uses two pairs of points to indicate axis direction, with one pair being dominant (*i.e.* the axis will be parallel to a vector derived from this

pair). The second and third axes are derived from the second pair of points, such that all axes are perpendicular, and the component of the second pair of points in the third axis direction is zero. The user defines the model scale by entering the real world distance between two selected points. Extra measurements can be used to assess the model's error.
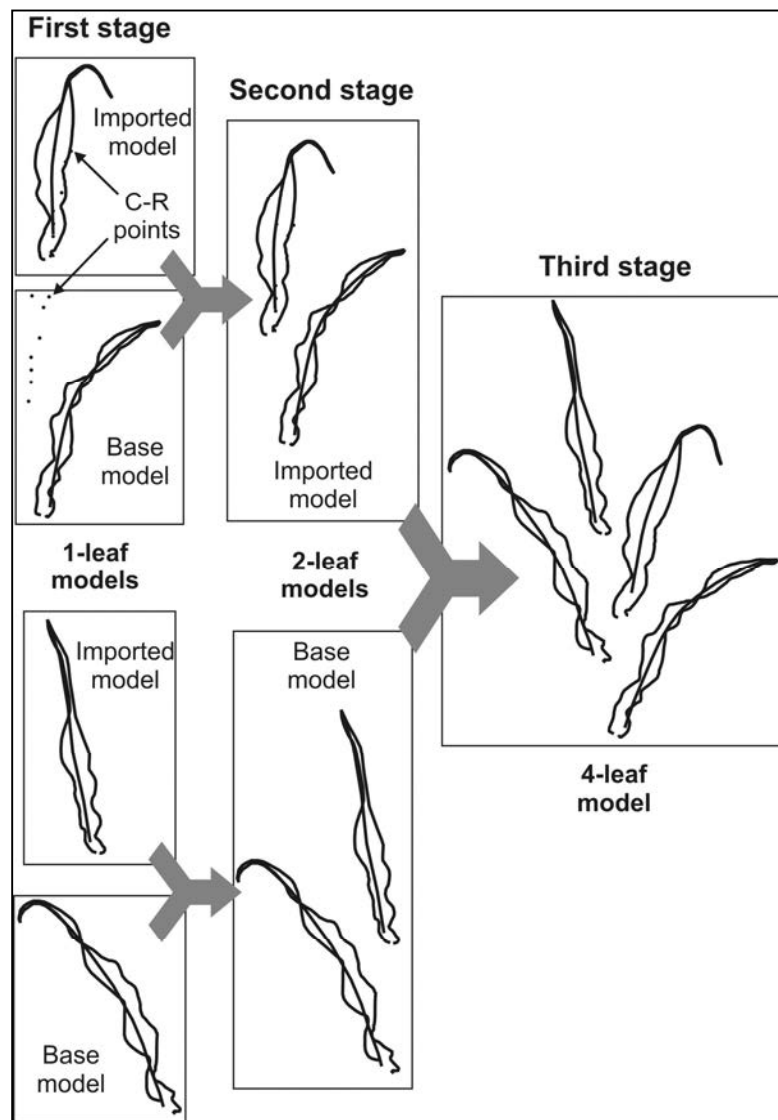
Figure V-9. Schematics showing the combination of individual leaf models. This procedure is repeated until the whole plant is completed. Reproduced from Frasson and Krajewski (2010).

Visual and quantitative assessments of the model error

The user can visually validate the model by projecting it onto the plane of one of the pictures and then superpose the lines that form the edges and mid-rib of the leaves. Although the current version of the photogrammetry software (as of 16 August 2010) does not allow for the superposition, it can export the model at any given plane. Combining the exported lines with the photograph was done using a commercially-available graphics editor. Older leaves and the tips of leaves are more susceptible to errors, as they are more flexible and easily disturbed by the wind. Figure V-10 shows an example of this validation. The edges and the mid-rib derived from the three-dimensional digital model of the plant are superposed on the picture in white.
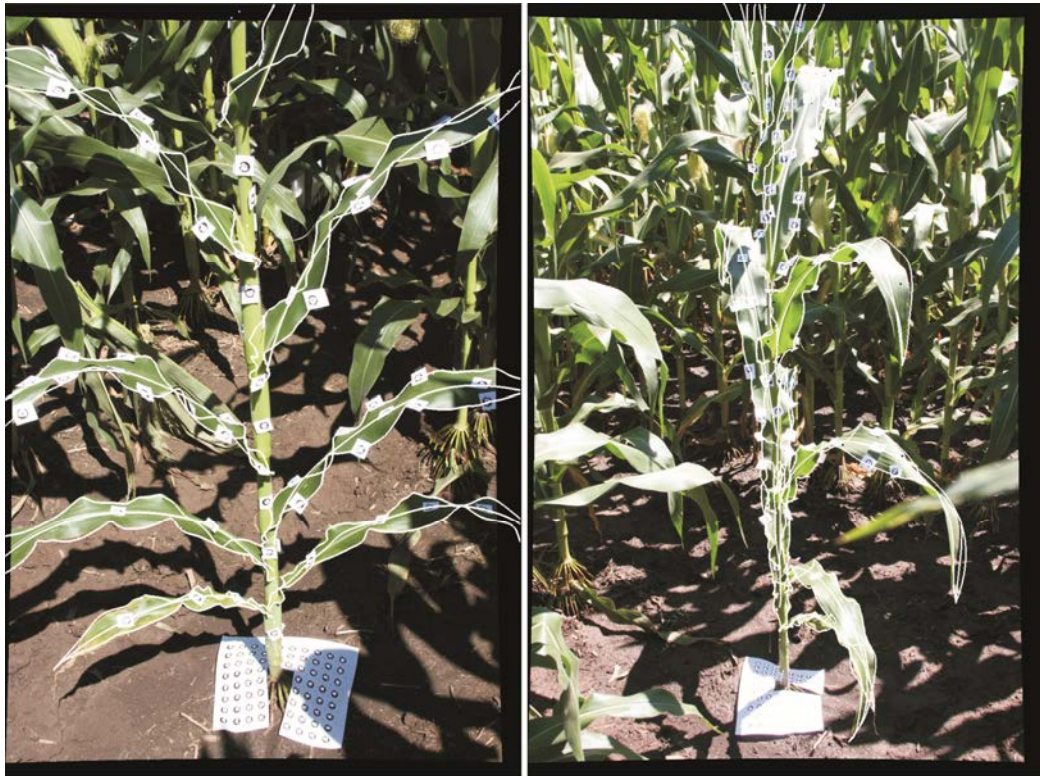
Figure V-10. Example of the visual validation. The 13 July 2010 model is presented superimposing one of the photographs used in its creation. The curved edges on the pictures are caused by the removal of lens distortion.

Bringing the digital models into Matlab®

The photogrammetry package can export the plant model in several formats which are optimized for use in computer graphics and animation software. We chose to export the surfaces that represent the leaves in the raw format, with each file containing only one leaf. In this format, the photogrammetry program creates a file with the coordinates of the vertices of the triangles that form a leaf. Each line contains nine numbers, (*i.e.* the x-, y- and z-coordinates of the vertices of one triangle), separated by tabs and ending in a carriage return character. Although the data in this format is easy to read, it does not contain any information on the topology of the triangles.

We wrote a Matlab® script to read the individual leaf files and organize the information into three different classes in increasing order of complexity. The most elementary class is the vertex class, which contains the vertex id and its x-, y-, and z-coordinates. The next class is the triangle, which contains the triangle id, the id of its three vertices, the id of the neighboring triangles, whether or not each one of its three edges are also edges of the leaf or are on the mid-rib of the leaf, and the area of the triangle. The last class is the leaf, which stores in a vector the ids of the triangles forming each one of the leaves as well as the leaf azimuth and the leaf zenith.

Establishing topology

As the triangle topology is not included in the raw file, we had to recreate it as follows. First we read a line of data and extract from it the coordinates of the three vertices forming the new triangle. These vertices are temporarily stored in an auxiliary vector and compared to the previously read vertices to check for their uniqueness. If a vertex coincides with an existing vertex in the database, the point is not new and the id of the originally read vertex is assigned to one of the vacant vertices of the new triangle. If the vertex is new, it is added to the database and receives an id which is assigned to one

of the vertices ids of the new triangle. This procedure assures that each vertex contained in the vertex database is unique.

Once all triangles are read, we move to the search for neighbors. Each triangle can share up to three sides. In this procedure, we compare the ids of the vertices of each triangle to the vertices of the others. If two triangles share two vertices, this means that they also share an edge. If in the first triangle the shared vertices are *A-B*, then the *Neighbor A* field receives the id of the second triangle. If the shared vertices are *B-C*, then the *Neighbor B* field receives the id of the second triangle. Alternatively, if the shared vertices are *A-C*, then the *Neighbor C* field of the first triangle receives the id of the second one. At the same time, depending upon what vertices of the second triangle are shared, either *Neighbor A, B,* or *C* of the second triangle receives the id of the first, thus reducing the number of loops needed to cover all of the triangles forming a leaf. Those sides that are not found to be shared by another triangle remain with an initial value of zero, indicating that they are on the edge, or mid-rib of the leaf.

Tracing the mid-rib and the leaf edges

Another important piece of information that cannot be simply retrieved from the raw leaf data is the collection of points forming the mid-rib and leaf edges. This information serves not only to calculate the azimuth and zenith of the leaf, but also is helpful to route the movement of water droplets on the plants. We use the neighborhood property established earlier to trace the mid-rib and leaf edges, as detailed in the following paragraphs.

With the exception of the older, smaller, and frequently damaged lower leaves, each leaf is described by two surfaces. The first surface extends from the mid-rib to one of the edges, and the second connects the mid-rib to the opposite edge. This arrangement causes the edges and the mid-rib of a leaf to be located on unshared sides of triangles, *i.e.*, the triangle sides marked with a zero in the triangle neighborhood property as

illustrated in Figure V-11. It also causes the mid-rib to be located on two nearly coincident lines, which Figure V-11 shows as the two sequences of points 1-3-5-9-11-13 and 1-16-18-20-22-24-26-28-13.

The edges and mid-rib of a leaf converge only on the tip and on the end of the leaf. The convergence of the mid-rib and a leaf edge is marked by triangles featuring two unshared sides. Due to the geometric constraints of this technique, such triangles are bound to happen only in such convergences. This represents a convenient way to locate the tip and the end of the leaf. In Figure V-11, the four triangles that feature only one neighbor are 1-2-3, 1-15-16, 12-13-14, and 13-28-29.
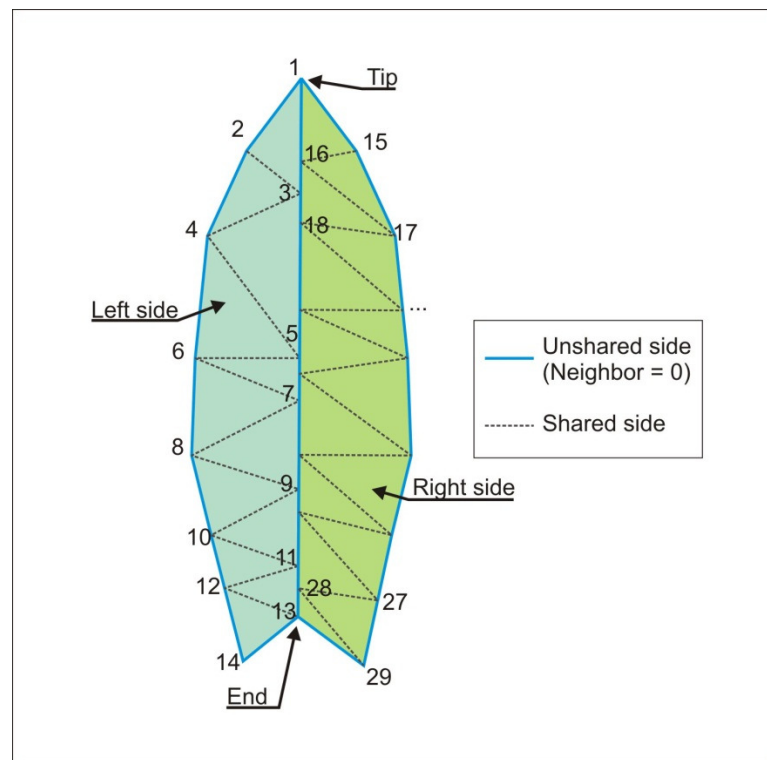
Figure V-11. Schematics of a leaf after the establishment of triangle neighborhoods. Shared sides are represented as a dashed black line while unshared sides are identified as solid blue lines. The numbers in the figure represent the vertices ids. The left and the right sides are independent and only share two vertices, in this fictitious case the vertices 1 and 13, *i.e.* the tip and the end of the leaf, respectively.

The first step in tracing the edges and mid-rib of the leaf is to find the two triangles that share the tip of the leaf as a vertex (in Figure V-11, the triangles 1-2-3 and 1-15-16) and the two triangles that have the end of the leaf as a vertex (in Figure V-11, the triangles 12-13-14 and 13-28-29). These triangles define the two first points of the two edges and two almost coincident lines located on the mid-rib, although at this point it is not possible to say which points belong to a leaf edge or the mid-rib.

As an example, let us trace the left edge. The initial triangle is 1-2-3. As the side 1-2 has no neighbor, hence the blue color, it is on the edge or the mid-rib. Since the vertex 1 is shared by another triangle, the correct order is 1-2. To find the next point, we examine the triangle that neighbors the triangle 1-2-3 and shares the vertex 2, *i.e.* the triangle 2-3-4. If the edge that we are tracing is one of the sides of this triangle, the triangle must contain the last recorded vertex, in this case vertex 2, and the side must have no neighbors. Two sides contain the vertex 2: the side 2-3 and the side 2-4. Since 2-4 is not shared by any other triangles, the next vertex on this edge is the vertex 4.

In order to find the next triangle in the sequence, we check the triangle that neighbors the currently examined polygon (2-3-4) that shares the vertex 4, which leads us to use the triangle 3-4-5. Now the two sides that share the vertex 4 are 3-4 and 4-5. However both sides are shared by another triangle; hence, it cannot be an edge of the leaf. We then investigate the triangle that neighbors the triangle 3-4-5 on the side 4-5, which takes us to the triangle 4-5-6. Examining this triangle, we see that the side 4-6 contains the last vertex found to be part of the edge of the leaf (4) and not shared by any other triangles, so vertex 6 must be the next one.

This procedure is repeated until we reach point 13, which was found to be the common point between the other two triangles of interest (12-13-14 and 13-28-29), or until there are no more triangles to examine, which might indicate something particular in the leaf geometry that must be investigated. This procedure is repeated for the four edge candidates, and we decide which of the four are on the edge of the leaf or on the mid-rib

by looking at their lengths. As the mid-rib of the leaf is necessarily shorter than the two edges, we compute the length of all four edge candidates. The two shorter ones are attributed to be on the mid-rib and the other two are the edges.

Calculating the leaf orientation

We chose to define the leaf orientation by calculating the azimuth and zenith of its mid-rib. Typically, the azimuth is the angular distance between the North and the direction of a fixed point with respect to the origin of the adopted coordinate system. Similarly, the zenith is the angular distance between the vertical and the direction of a fixed point with respect to the origin of the coordinate system. However, the leaf's curvature, in both horizontal and vertical planes, may lead to ambiguities in the selection of a point in the mid-rib that defines its direction.

To avoid such ambiguities, we decided to select the highest point of the leaf's mid-rib and a point on the base of the leaf to define its direction. The azimuth (Az) and the zenith (Ze) are calculated with the use of equations V-1 and V-2, where x_{max}, y_{max}, and z_{max} are the three dimensional Cartesian coordinates of the highest point of that leaf and x_{base}, y_{base}, and z_{base} are the coordinates of the base of the leaf.

$$Az = \tan^{-1}\left(\frac{x_{max}-x_{base}}{y_{max}-y_{base}}\right) \tag{V-1}$$

$$Ze = \tan^{-1}\left(\frac{z_{max}-z_{base}}{\sqrt{(y_{max}-y_{base})^2+(x_{max}-x_{base})^2}}\right) \tag{V-2}$$

There isn't a single criterion to choose two points that define the direction of a leaf. A different way would be selecting multiple points along its mid-rib, building vectors connecting the leaf base to each of the chosen points, determining their direction, and subsequently adopting their average as the leaf direction. Due to the increased flexibility of the maize leaf past its highest point and its lack of representativeness of that portion of the leaf on its direction, we chose to use the highest point on the leaf's mid-rib to compute its direction.

Projecting the leaves and creating a coverage matrix

Leaf area index, gap fraction, canopy coverage factor, leaf overlap, and other plant and canopy parameters are derived from projected areas. Once the leaves are projected on the chosen plane, we build a coverage matrix for each leaf. The matrices allow rotation, translation, and superposition of leaves, which are inputs in the evaluation of the before mentioned plant and canopy parameters.

Originally, we have a right handed orthogonal coordinate system, with axis *x*, *y* in the horizontal plane and *z* in the vertical direction. Let the axes *x'-y'-z'* be the product of the rotation of the *x-y-z* axes by an angle of   degrees around y and beta degrees around   . By applying equation V-3, one can find the coordinates of a given point with coordinates x_a, y_a, z_a on the arbitrary *x'-y'-z'* coordinate system. Finally, each vertex of the leaf can be projected on the *x'-y'* plane by applying equation V-3 and disregarding the z' coordinate.

$$\begin{bmatrix} x' \\ y' \\ z' \end{bmatrix} = \begin{bmatrix} \cos\alpha & 0 & -\sin\alpha \\ \sin\alpha\sin\beta & \cos\beta & \sin\beta\cos\alpha \\ \sin\alpha\cos\beta & -\sin\beta & \cos\alpha\cos\beta \end{bmatrix} \cdot \begin{bmatrix} x \\ y \\ z \end{bmatrix}$$ (V-3)

With the projected coordinates, we built the coverage matrix. First we divide the *x'-y'* plane into pixels with associated coordinates. We compare the coordinates of the center of each pixel to those of the projected leaf. If the central coordinate of the pixel is inside any of the triangles that form the leaf, the corresponding element on the coverage matrix is incremented by one. For each leaf we created a matrix, illustrated by equation V-4, whose elements correspond to the number of leaf elemental triangles covering each one of the pixels and are associated to coordinates $X_{i,j} = \begin{bmatrix} x_i & y_j \end{bmatrix}$.

$$L_1 = \begin{bmatrix} 0 & 0 & 0 & 0 & \dots & 0 \\ 0 & 1 & 1 & 0 & 0 & 0 \\ 0 & 1 & 1 & 1 & 0 & 0 \\ 0 & 0 & 1 & 1 & 0 & 0 \\ \vdots & 0 & 0 & 0 & \ddots & \vdots \\ 0 & 0 & 0 & 0 & \dots & 0 \end{bmatrix}$$ (V-4)

We created each leaf's projection using the same coordinate system, allowing the use of equation V-5 to superpose the leaves and build the full plant matrix as exemplified in Figure V-12. This figure shows the visual representation of a coverage matrix of a full plant. The darker colors in Figure V-12 indicate a higher degree of superposition. In equation V-5, L stands for the individual leaf matrix, k for the leaf's number, N for the number of leaves of each plant, and m and n indicate the position in the canopy, which will be discussed in the next section.

$$P_{m,n} = \sum_{k=1}^{N} L_k \qquad\qquad (V\text{-}5)$$
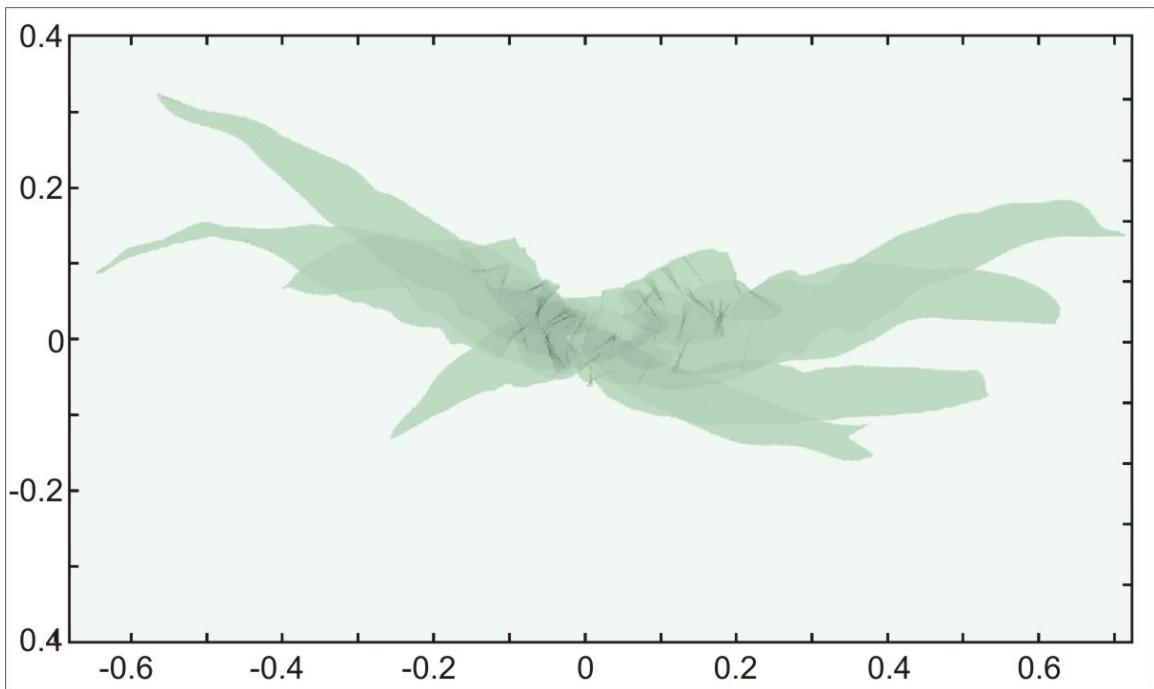
Figure V-12. Example of a single plant coverage matrix. This coverage matrix is produced by superimposing (adding) the single leaf matrices.

Creating more plants

We pursue two avenues to create the digital canopy. First, we replicate the original digital plant model and position them according to the field row and in-row

distances. However, replicating the plant density doesn't necessarily result in a digital canopy with the same characteristics as observed in the field. In order to achieve a more realistic representation, we adjust each plant's azimuth until the digital model reproduces the canopy characteristics observed in the field.

Since we observed in CHAPTER III that the canopy gap fraction is an important factor in the partitioning of rainfall into direct and indirect throughfall, we modify the orientation of each plant until the model's gap fraction approaches the value measured in the field. Although this technique allows more control of the gap fraction, it yields a canopy composed of identical plants.

The second approach leads to more varied canopies by calculating different individual leaf orientations. In this approach, individual leaves are the building blocks of the canopy. The initial step is to align all leaves with the row direction. To do so, we first move the leaf to the origin of the coordinate system, placing the leaf's base a half stem diameter away from it. Equations V-6 and V-7 display how many pixels the leaf has to go in the i (across rows) and j (along the row) directions for a general Δx or Δy translation. In both equations, p stands for the precision used to create the axes and \ to the integer division rounded towards -∞.

The next step is to rotate the leaf by applying **V-9** to the central coordinates of each once of its pixels. In this equation, X represents the x and y coordinates of the pixel i,j, Δx and Δy are the distances across rows and along the rows that the particular point has to travel, and R is the rotational matrix given by V-8, where θ is the clockwise rotational angle, in this case the azimuth of the leaf k in the negative direction. With Δx and Δy calculated, they are translated to an integer number of pixels by V-6 and V-7.

$$\Delta i = \Delta x \backslash p \qquad\qquad\qquad\qquad\qquad\qquad\qquad\qquad \text{(V-6)}$$

$$\Delta j = \Delta y \backslash p \qquad\qquad\qquad\qquad\qquad\qquad\qquad\qquad \text{(V-7)}$$

$$R = \begin{bmatrix} \cos\theta & \sin\theta \\ -\sin\theta & \cos\theta \end{bmatrix} \qquad\qquad\qquad\qquad\qquad\qquad \text{(V-8)}$$

$$\begin{bmatrix} \Delta x_{i,j} \\ \Delta y_{i,j} \end{bmatrix} = \boldsymbol{R} \cdot \boldsymbol{X_{i,j}} \hspace{4cm} \textbf{(V-9)}$$

The original leaves, with azimuth 0 and a base located at (0,10) mm, are a template to create the plants. We create the canopy by replicating these leaves from the lowest leaf to the highest, respecting their order of occurrence in the original plant. Plant by plant, we place the first leaf at a random azimuth with its base located at 10 mm away from the center of each plant's stem, resulting in a 20 mm diameter stem. We tested three different azimuth generating functions, all based on the uniform distribution or a linear combination of two values drawn from uniform distributions. Equations V-10, V-11, and V-12 show the three generator functions. In the following equations, $Az_{1,m,n}$ stands for the azimuth of the first leaf of the n-th plant located in the m-th row and U for the uniform distribution.

$$Az_{1,m,n} \sim U[0,360] \hspace{4cm} \text{(V-10)}$$

$$Az_{1,m,n} = 45° \cdot (1 + 2 \cdot U[0,1] + 4 \cdot U[0,1]) \hspace{2cm} \text{(V-11)}$$

$$Az_{1,m,n} = 22.5° \cdot (1 + 6 \cdot U[0,1] + 8 \cdot U[0,1]) \hspace{2cm} \text{(V-12)}$$

Azimuths generated by the function V-10 vary from 0 to 360° and allow the superposition of the first leaf and the stem of neighboring plants, which is unrealistic. To prevent this superposition, we created two other azimuth generators, shown in V-11 and V-12. The first, more restrictive, only allows the placing of first leaves between the angles of 45° and 135° and 225° and 315°. The second (equation V-12) is less restrictive and allows the location of first leaves between 22.5° and 157.5° and also 202.5° and 337.5°. Equation V-10 tends to produce canopies with lower gap fraction, while V-11 leads to lower leaf overlap. We chose to work with equation V-12, which is less restrictive yet offers reduced probability of overlap between neighboring stems and the first layer of leaves.

Once the first layer of leaves is in place, we create the second layer. These leaves are identical copies of the second leaf of the original plant. Their placement depends

upon the azimuth of the first leaf and also the location of the neighboring plants' second leaves. We initially place the second layer of leaves with an angle of 180° with respect to the first leaf of each plant. However, as shown by Frasson and Krajewski (2010), the maize leaves are not perfectly aligned with a vertical plane. To allow this misalignment, we added a deflection to the leaf's azimuth.

We assume that leaves, while competing for resources, such as sun light or rain water, reposition themselves to minimize overlap. We also assume that once a leaf is fully grown, it can't move any further. Since the procedure for the calculation of the second leaf's azimuth is identical to the procedure used to compute the alignment of all succeeding leaves, we refer to the currently considered leaf as leaf k of a plant located in the row o in the position p.

To recreate this behavior, we initially construct a template coverage matrix (TC) with the footprint of all leaves at the considered level, excluding the current leaf, as in V-13. Leaves with known azimuths, *i.e.*, $m<o$ and $n<p-1$ represented by the first summation in equation V-13, are oriented accordingly. Subsequently, leaves that lack a calculated azimuth ($m>o$ or $n>p$ represented by the second summation of equation V-13) are positioned at their plant's preferential plane given by V-14, that is with no deflection.

$$TC_{o,p,k} = \sum_{m=1}^{o-1} \sum_{n=1}^{p-1} L_k + \sum_{m=o+1}^{N_R} \sum_{n=p+1}^{N_{IR}} L_k \tag{V-13}$$

$$Az_{k,m,n} = Az_{k-1,m,n} + 180 - Deflection \tag{V-14}$$

Finally, we add the missing leaf to a temporary coverage matrix built from the template coverage matrix oriented at the maximum deflection. Using this temporary coverage matrix, we recalculate the coverage factor. We repeat the procedure, but this time with the deflection decremented by one degree until the minimum deflection is achieved. The azimuth of this leaf is the angle that maximizes the canopy coverage.

Results

Single plant models

We created five digital plant models, two of fully developed plants (Figure V-14 and Figure V-15) and three of plants in intermediate stages (Figure V-13, Figure V-16, and Figure V-17). To assess the accuracy of the models, we compared the extra distances measured during the picture taking process, with distances measured in the three-dimensional models following the methodology that are described in Frasson and Krajewski (2010).

Figure V-13 shows the first digital model that we created. The full model made use of 48 pictures to recreate the geometry of 6 leaves described by a total of 348 points, as detailed in Table V-2. The total leaf area of this plant was 1459 cm^2, which translated to 772 cm^2 when projected onto a horizontal plane. If only the non-overlapping area is considered, the full plant's projected area is reduced to 632 cm^2. These numbers result in a leaf overlap ratio of about 18% at this stage of development. Table V-3 summarizes the model's geometrical features.
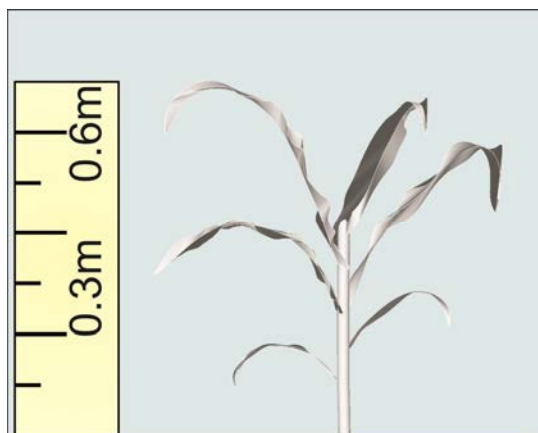
Figure V-13. Side view of the model derived from the pictures taken on 18 June 2008 in Iowa City, Iowa. This same plant was photographed on 16 July, when it was fully developed. Reproduced from Frasson and Krajewski (2010).

Table V-2. Number of pictures used to create the digital model displayed Figure V-13 and the resulting number of points digitized on each leaf.

Leaf number	Number of pictures	Number of points
1	8	111
2	12	112
3	5	29
4	3	43
5	10	34
6	10	19

Table V-3. Summary of the digital model's geometric properties.

Leaf number	Mid-rib length (cm)	Width (cm)	Area (cm^2)	Projected area (cm^2)
1	42	8	257	201
2	64	7	440	205
3	56	7	371	123
4	47	5	237	121
5	36	4	93	77
6	28	3	62	45
Total	-	-	1459	772

We conducted a simple uncertainty assessment by comparing measurements of leaf width taken on the real plant with corresponding measurements taken on the digital model. With the exception of the third leaf, all deviations were less than one centimeter, as shown in Table V-4. Unfortunately, there were no full plant pictures that could be oriented to assess how the digital leaf orientation compares to the real plant.

Table V-4. Uncertainty assessment regarding the 18 June 2008 plant model.

Leaf number	Measured width (cm)	Model width (cm)	Error (cm)	Relative error (%)
1	7.5	7.8	0.3	3.9
2	7.2	7.8	0.6	7.9
3	7.4	6.2	-1.2	-16.2
4	5	4.8	-0.2	-4
5	3.5	3.6	0.1	2.3
6	2.7	2.7	0.0	-0.4

Note: The average error was -1.1 cm, and the standard deviation of the error was 8.5cm, excluding the point used for calibration.

Next is the model built using the pictures taken on 16 July 2008. Figure V-14 shows a digital plant model featuring 10 leaves constituting a 2.47 m tall plant. Table V-5 shows the number of pictures used to create this model and the resulting number of points, illustrating the level of detail displayed by this model. The projected area of the whole plant is 1902 cm^2, while the summation of the projected areas of all leaves is 3340 cm^2, which corresponds to a leaf overlap ratio of 43%. Table V-6 shows the width, area and projected area of each one of the leaves.

While we prepared the modeled plant to be photographed, we measured the distance between at least three pairs of targets per leaf. This allowed a better uncertainty assessment, which is presented in Table V-7. Positive and negative differences are distributed throughout the leaves do not suggest the presence of systematic errors.

The largest relative difference between measurements taken on the real plant and those calculated for the model was 14% and occurred on the 7th leaf. It corresponded to an absolute difference of 2.7 cm, which is not reproduced by the other two measurements taken from that same leaf. The highest absolute difference was 3 cm, present in the 9th leaf. The only other residue that approached 2 cm happened in the 6th leaf. All measurements were taken along the leaf, which could have been caused by the mid-rib curvature. This made measuring the distance more difficult and was not taken into account in the model's measurements.
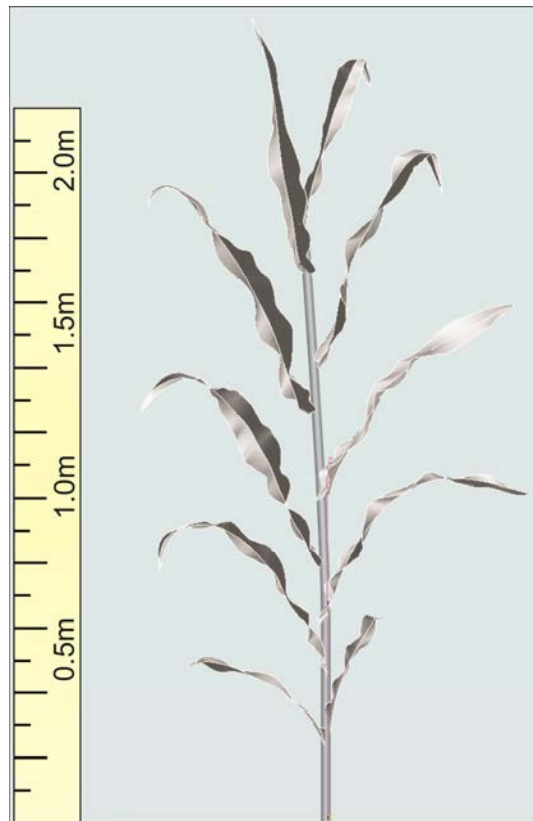
Figure V-14. Side view of the model derived from the pictures taken on 16 July 2008. Reproduced from Frasson and Krajewski (2010).

Table V-5. Number of pictures used to create the digital model displayed Figure V-14 and the resulting number of points digitized on each leaf.

Leaf number	Number of pictures	Number of points
1	17	213
2	16	369
3	7	34
4	17	176
5	13	163
6	10	161
7	18	108
8	7	116
9	6	133
10	8	80

Table V-6. Summary of geometrical properties calculated from the model derived from the pictures taken on 16 July 2008 in Iowa City, Iowa.

Leaf number	Mid-rib length (cm)	Width (cm)	Area (cm^2)	Projected area (cm^2)
1	77	12	582	254
2	83	13	727	163
3	84	12	893	351
4	81	12	1046	519
5	91	10	832	401
6	81	11	984	562
7	79	10	682	374
8	62	9	690	390
9	33	7	270	102
10	49	6	300	223
Total	-	-	7004	3340

Table V-7. Uncertainty assessment regarding the 16 July 2008 plant model.

Leaf number	Target ID		Measured distance (cm)	Model distance (cm)	Error (cm)	Relative error (%)
1	9	518	10.3	10.3	0.0	-0.4
	247	296	22.3	21.6	-0.7	-3.0
	401	404	23.5	23.0	-0.5	-2.2
2	106	501	22.0	22.0	0.0	-0.1
	6	304	11.0	12.7	1.7	15.6
	503	245	23.8	24.8	1.0	4.1
3	394	536	7.2	7.4	0.2	2.5
	338	394	14.5	14.7	0.2	1.3
	400	525	5.5	5.8	0.3	5.9
4	319	346	8.0	7.9	-0.1	-1.6
	499	559	23.0	23.0	0.0	0.0
	466	505	8.9	8.7	-0.2	-2.1
5	118	393	22.5	23.5	1.0	4.6
	28	178	8.5	9.2	0.7	8.8
	150	372	6.0	6.5	0.5	8.8
6	435	193	12.7	14.2	1.5	11.8
	20	290	10.0	10.8	0.8	7.9
	171	128	20.0	22.0	2.0	10.0
7	423	87	19.2	21.9	2.7	14.0
	279	413	12.0	12.8	0.8	7.0
	85	110	9.7	10.4	0.7	7.6
8	481	194	28.5	27.5	-1.0	-3.7
	222	384	12.0	11.2	-0.8	-6.8
	122	526	10.2	10.0	-0.2	-2.1
9	306	500	25.0	22.0	-3.0	-12.0
	104	447	11.3	10.1	-1.2	-10.9
10	252	425	18.0	19.1	1.1	6.3
	199	538	6.7	7.4	0.7	9.9
	73	252	12.7	13.6	0.9	7.2

Note: The average error was 0.3 cm and the standard deviation of the error was 1.1 cm, excluding the point used for calibration. Adapted from Frasson and Krajewski (2010)

In 2009, we moved our experimental setup to Shueyville, Iowa. In that location, maize plants of the variety Pioneer 36V75Hx, RR$_2$ were planted on 24 April 2009. Figure V-15 shows the 2.39 m tall, 13-leaf model that resulted from pictures taken on 20 July 2009. This is the model selected to populate the virtual canopy presented in the next section. Table V-8 shows the number of pictures used to recreate the plant's geometry and the resulting number of points that delineate the edges and the mid-rib of the leaves that form this model.
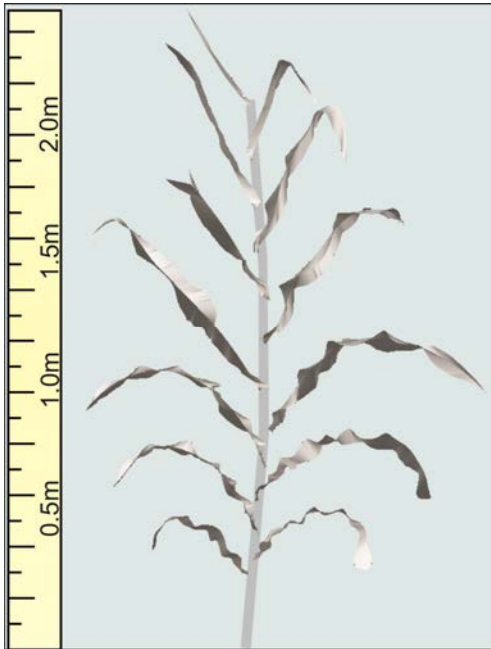
Figure V-15. Side view of the model derived from pictures taken on 20 July 2009 in Shueyville, Iowa.

The lower number of points per leaf shown in Table V-8 suggests that the 20 July 2009 model's leaves are less detailed than those belonging to the 16 July 2008 model. However, this actually reflects better positioning of the points, decreasing their spacing in

areas where the leaf edge or the mid-rib's geometry is more complex and distancing them

where the geometry is simpler.

Table V-8. Number of pictures used to create the digital model displayed Figure V-15
and the resulting number of points digitized on each leaf.

Leaf number	Number of pictures	Number of points
1	6	58
2	20	159
3	16	186
4	11	147
5	11	76
6	14	132
7	11	248
8	16	153
9	10	139
10	8	117
11	14	154
12	8	89
13	5	76

Table V-9 shows some of the geometrical properties of the 13 leaves that form the

2009 digital plant model. For this model, the plant's footprint was 1906 cm^2, which is

similar to the 16 July 2008 digital model. The sum of each leaf's projected area is

4126 cm^2, which leads to a leaf overlap ratio of 0.54. Similarly to the model portrayed in

Figure V-14, the intermediate leaves concentrate more area than the new leaves on the

top and the old and frequently damaged lower leaves. For this model, the 6th to the 9th

leaves accumulate 45% of the total leaf area of the plant. Although the former model has

fewer leaves (10 versus 13), if the three upper or the three lower leaves from the latter

model were added to it, their total leaf areas would be quite similar, with the difference between the 2 totals on the order of 1%.

Table V-9. Summary of geometrical properties calculated from the model derived from the pictures taken on 20 July 2009 in Shueyville, Iowa.

Leaf number	Mid-rib length (cm)	Width (cm)	Area (cm^2)	Projected area (cm^2)
1	47	6	239	115
2	63	10	444	176
3	73	11	583	263
4	80	11	773	277
5	49	8	579	231
6	82	10	893	488
7	97	13	862	326
8	107	11	1144	673
9	93	9	818	469
10	82	9	702	436
11	78	7	512	315
12	74	5	414	245
13	25	6	224	135
Total	-	-	8187	4126

We assessed the model's uncertainty in a similar fashion as with previous model. Table V-10 shows the comparison between the physical measurements and those obtained from the digital model. The average discrepancy and its standard deviation were less than 1 cm. The largest disagreements happened in the 10th leaf, where the magnitudes exceeded 1 cm. Other than these two examples, only one other measurement was more than 1 cm off. We measured distances between pairs of points using a measuring tape graded in millimeters and, often in uncomfortable positions. For this reason we believe that the observed discrepancies are reasonable.

Table V-10. Uncertainty assessment of the 20 July 2009 plant model.

Leaf number	Target ID		Measured distance (cm)	Model distance (cm)	Error (cm)	Relative error (%)
1	371	370	6.8	5.9	0.9	14.0%
	371	415	11.8	12.0	-0.2	-1.7%
	422	2	9.5	9.5	0.0	0.0%
2	189	249	12.1	12.3	-0.2	-1.7%
	366	4	10.0	9.4	0.6	6.0%
3	457	72	9.7	9.9	-0.2	-2.1%
	442	138	9.1	9.4	-0.3	-3.3%
	138	451	15.5	15.9	-0.4	-2.6%
4	154	276	8.9	8.9	0.0	0.0%
	444	188	11.0	10.7	0.3	2.7%
	253	337	17.9	18.1	-0.2	-1.1%
5	485	375	11.2	11.4	-0.2	-1.8%
	418	404	13.4	13.5	-0.1	-0.7%
	3	281	12.1	12.4	-0.3	-2.5%
6	309	376	18.0	19.2	-1.2	-6.7%
	177	482	10.0	10.4	-0.4	-4.0%
	386	238	9.0	9.6	-0.6	-6.7%
7	408	314	28.0	28.0	0.0	0.0%
	350	111	25.9	26.7	-0.8	-3.1%
	459	374	15.9	16.6	-0.7	-4.4%
8	456	363	9.5	9.8	-0.3	-3.2%
	389	191	21.5	22.3	-0.8	-3.7%
	456	222	13.5	14.1	-0.6	-4.4%
10	414	443	16.0	14.8	1.2	7.5%
	290	453	18.0	16.5	1.5	8.3%
12	352	50	10.6	9.8	0.8	7.5%
	172	50	6.5	6.4	0.1	1.5%
	397	40	7.4	6.7	0.7	9.5%

Note: The average error was -0.7 cm and the error standard deviation was 0.6cm, excluding the point used for calibration. Validation measurements for leaves 9, 11 and, 13 were not available due to difficulties in matching the pair of targets with their digital counterparts.

In the following year we constructed two digital models. The first was based on pictures taken on 29 May 2010 and shown in Figure V-16 and the second was constructed from pictures taken on 13 July 2010 and presented on Figure V-17. The first depicts a young plant. Despite having eight leaves, it is quite smaller than the six-leaf model built in 2008. The size of the five lower leaves, all smaller than 70 cm^2, and their height, all below 25 cm, indicates that they probably fall off the plant and are not present at later ages.
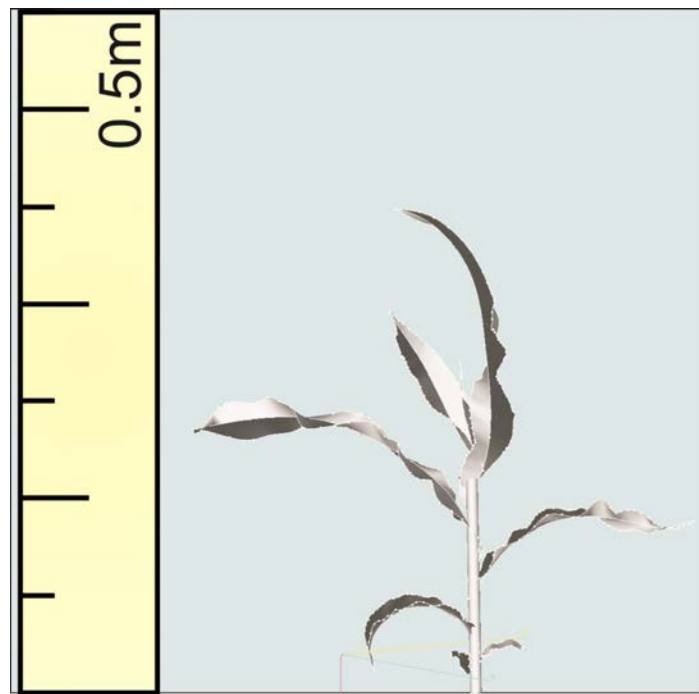
Figure V-16. Side view of the model derived from pictures taken on 29 May 2010 in Shueyville, Iowa. 20 pictures were used to calculate the coordinates of 515 points that describe the leaves and stem of this model.

This plant footprint accounted for 162 cm^2, while the sum of the leaves' areas was 204 cm^2. This resulted in a leaf overlap ratio of 0.26, the lowest observed in this study.

Table V-11 shows the mid-rib length, leaf width, area and projected area of each leaf of this model.

Due to the size of this plant, targets needed to be smaller than usual, which made them hard to visualize. Therefore, we chose to print a grid of targets and place them under the plant. This grid allowed us to orient various pictures. The leaves were manually traced. Although this change in procedure allowed the digitizing of young plant, it prevented a quantitative validation.

Table V-11. Summary of geometrical properties calculated from the model derived from pictures taken on 29 May 2010 in Shueyville, Iowa.

Leaf number	Mid-rib length (cm)	Width (cm)	Area (cm^2)	Projected area (cm^2)
1	9	1	7	2
2	24	4	68	29
3	33	4	122	34
4	34	3	121	68
5	24	2	69	43
6	16	2	39	17
7	4	2	7	5
8	2	2	8	7
Total	-	-	436	204

Figure V-17 shows the last model that we created. It is based on pictures from 13 July 2010. Table V-12 shows the number of pictures used in the digitizing of each leaf, and the resulting number of points. As with the 2009 model, the absolute number of points shaping the leaves is not as high as the 16 July 2008 model. Nevertheless, the level of detail of this model is not lower, as it reflects better positioning of points. The digital plant has 11 leaves, is 2 m tall, and has a total leaf area of 4675 cm2. The plant

footprint covers 1620 cm^2, which results in a leaf overlap ratio of 0.38. Table V-13 shows some geometric properties of each leaf of this model.

The qualitative validation of this whole model was possible due to the increased canopy opening around this plant. Figure V-10 shows the good agreement between the digital model and two pictures of the plant. This agreement is also visible in the quantitative validation shown in Table V-14, where the largest discrepancy between physical measurements and those obtained from the digital model is 5 mm. In relative terms, the highest variation is slightly above 6%.
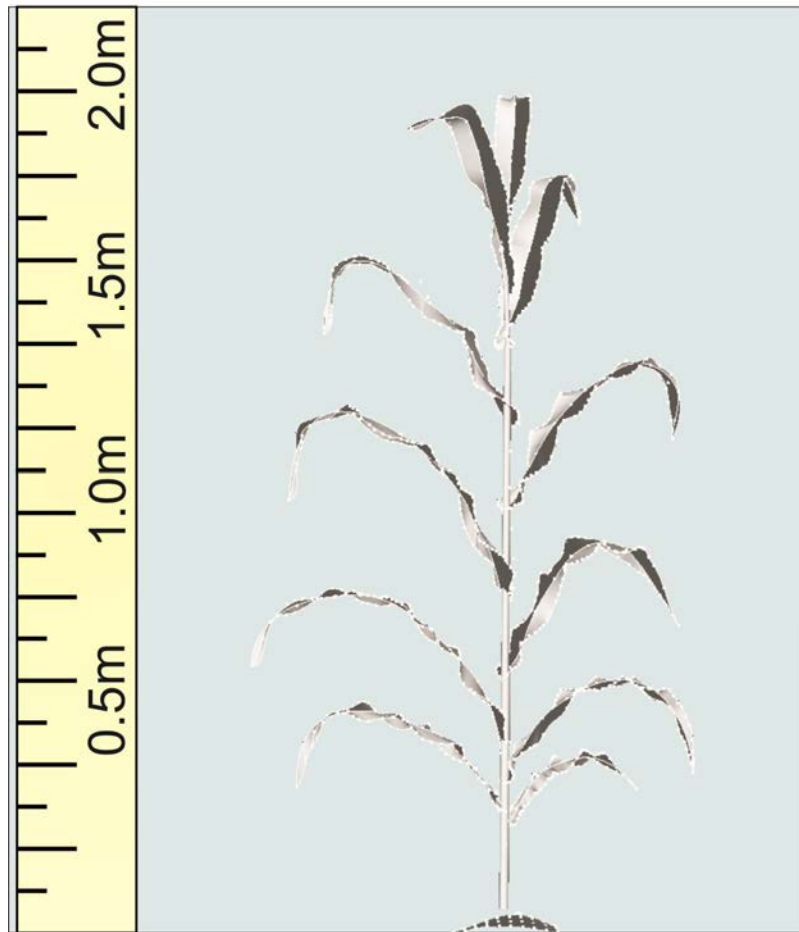
Figure V-17. Side view of the model derived from pictures taken on 13 July 2010 in Shueyville, Iowa.

Table V-12. Number of pictures used to create the digital model displayed in Figure V-17 and the resulting number of points digitized on each leaf.

Leaf number	Number of pictures	Number of points
1	7	89
2	7	90
3	7	90
4	11	90
5	12	90
6	11	110
7	11	112
8	11	110
9	11	111
10	3	90
11	3	82

Table V-13. Summary of geometrical properties calculated from the model derived from the pictures taken on 13 July 2010 in Shueyville, Iowa.

Leaf number	Mid-rib length (cm)	Width (cm)	Area (cm^2)	Projected area (m^2)
1	53	7	305	54
2	63	9	427	237
3	59	7	417	175
4	70	9	529	298
5	74	8	549	344
6	81	8	579	328
7	83	7	520	338
8	81	7	472	296
9	70	6	369	239
10	63	5	324	191
11	45	5	182	122
Total	-	-	4675	2622

Table V-14. Uncertainty assessment regarding the 13 July 2010 plant model.

Leaf number	Target ID		Measured distance (cm)	Model distance (cm)	Error (cm)	Relative error (%)
1	87	295	16	15.7	0.3	1.9%
	162	88	6.5	6.5	0	0.0%
	162	87	12.1	11.9	0.2	1.7%
2	98	86	11.5	11.6	-0.1	-0.9%
	256	145	8.7		N/A	
	245	85	6.5		N/A	
3	111	100	20.7	20.5	0.2	1.0%
	240	293	8.4	8.3	0.1	1.2%
	133	112	22.1	21.7	0.4	1.8%
4	123	84	14.1	13.9	0.2	1.4%
	125	153	13.4	13.5	-0.1	-0.7%
	125	113	8.7	8.5	0.2	2.3%
5	43	63	8.1	8.1	0.0	0.0%
	221	288	8.5	8.3	0.2	2.4%
	223	137	8.9	8.7	0.2	2.2%
6	71	90	12.6	12.5	0.1	0.8%
	11	17	8	7.9	0.1	1.3%
	90	289	11.4	11.1	0.3	2.6%
7	89	56	8.2	7.9	0.3	3.7%
	114	281	18	17.5	0.5	2.8%
	108	218	8.2	7.7	0.5	6.1%
8	74	115	14.9	14.6	0.3	2.0%
	103	104	7	6.8	0.2	2.9%
	94	200	15.5	15.2	0.3	1.9%
9	109	205	16.1	15.9	0.2	1.2%
	251	276	14.5	14.6	-0.1	-0.7%
	246	300	12.2	12.3	-0.1	-0.8%
10	251	276	14.5	14.6	-0.1	-0.7%
11	2	146	20.3		Calibration	

Note: The average error was -0.2 cm, and the error standard deviation was 0.2cm, excluding the point used for calibration.

In the next section we discuss the use of the leaves taken from the 13 July 2009 model as the building block of the digital canopy. Canopies at different stages of development and different number and sizes of leaves can be created by selecting the appropriate template model. The choice of models is also guided by leaf geometric characteristics such as leaf area and zenith, here used indirectly by considering the projected area.

<div align="center">Canopy models</div>

The first virtual canopy is a result of the simpler methodology presented earlier in this chapter in which we create several copies of the single plant model keeping the orientation of the leaves as in the original model. We locate the digital plants to mimic the field's density and calculate their orientation to reproduce the desired gap fraction. We attempt to recreate the gap fraction of 0.22 calculated from the top view of the 2008 canopy (right hand side of Figure V-18) by creating replicas of the 16 July 2008 model. We arrange the virtual plants in rows, placed them 0.90 m apart and featured an in-row separation of 0.13 m.

The left panel of Figure V-18 shows the resulting simulated canopy with the color shades representing the overlap between leaves and with darker colors indicating more overlap. This digital canopy reproduces the field gap fraction, demonstrating that the present methodology offers great control over the canopy coverage. Nevertheless, the canopy is composed of identical plants and doesn't look realistic. Furthermore, enforcing the condition that two leaves, or a leaf and a plant's stem, cannot occupy the same space would be challenging to implement and would come at the cost of control over the canopy gap fraction.

Alternatively, we chose to calculate the horizontal orientation of each leaf separately, based on the rule that, for each generated layer of leaves, the upper leaves will grow in angles that will minimize overlap with other neighboring leaves located at the

same height. Although this method doesn't allow direct control over the gap fraction, it creates unique and more realistic canopies. Different gap fractions can be achieved by changing the plant density and, to a lesser degree, the maximum deflection that a leaf is allowed to have from the plant's preferential plane.
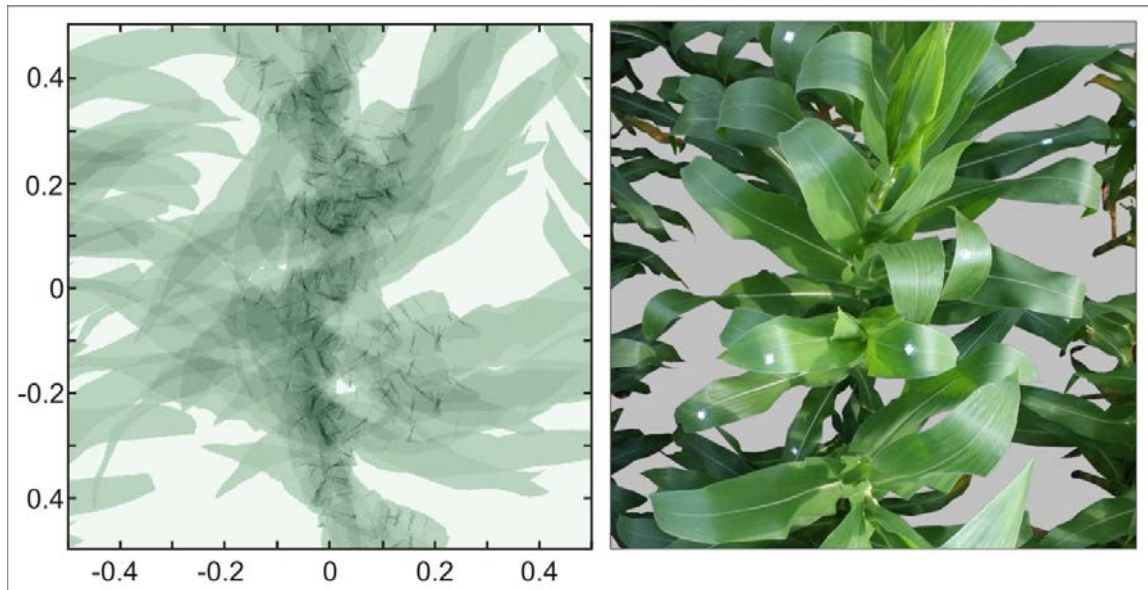
Figure V-18. The right panel shows the top view of the canopy used to calculate the ratio between visible soil surface to plant area. Taken on 25 July 2008. The gray areas are polygons traced manually where the soil surface was visible. The gap fraction for this example is 0.22. The left panel shows a simulated canopy with equivalent plant spacing. The simulated gap fraction was also 0.22.

We created 10 canopies with a 15° maximum deflection from the preferential plane and the same number of canopies with a 30° angle. We kept the plant density the same for both sets of canopies to isolate the effect of the maximum deflection. The average canopy coverage of the 10 canopies created with a maximum deflection angle was 0.87 with a standard deviation of 0.021, while the average canopy coverage of the 10 canopies whose leaves were allowed to vary within ±30° from each plant's preferential plane was 0.92 with a standard deviation of 0.017. The difference between the averages

is statistically significant, showing that the maximum deflection angle has an influence on the canopy coverage.

Being more restrictive in how a leaf can deviate from a plant's preferential plane leads to higher leaf overlap and lower canopy coverage. However, the canopy coverage generated with this method, even when using identical properties, is a random variable as illustrated by Table V-15. Therefore, searching for one specific canopy coverage value is a trial and error process. If the computer's available memory during canopy calculation allows it, a more efficient procedure to create a canopy with the desired gap fraction is to generate a larger canopy and look within it for an area that fulfills the requirement.

Table V-15. Canopy coverage of the canopies created to investigate the influence of the leaf maximum deflection angle into the canopy coverage factor.

Canopy #	Canopy Coverage	
	15°	30°
1	0.88	0.93
2	0.90	0.92
3	0.86	0.91
4	0.85	0.96
5	0.85	0.94
6	0.91	0.91
7	0.86	0.94
8	0.86	0.91
9	0.85	0.92
10	0.88	0.94

Note: All canopies featured a row distance of 0.94 m, and plants in the same row were 0.14 m apart.

To avert the superposition of leaves and stems of neighboring plants, we added a constraint that leaves can only be created with azimuths inside [22.5°, 157.5°] and [202.5°, 337.5°]. Figure V-19 shows the top view of the final canopy. This canopy

contains 27 plants organized in 3 rows with 9 plants per row. Each plant comprises 13 leaves, which are identical copies of those digitized from the 20 July 2009 pictures and presented in Figure V-15. As the plants and leaves located on the fringes of the coverage matrix may be affected by the absence of neighbors, their orientation may be unreliable. Therefore, we defined as useable area, *i.e.*, the area that we intend to use for hydrologic modeling, the section comprised between -0.5 m $\leq$ x $\leq$ 0.5 m and -0.5 m $\leq$ y $\leq$ 0.5 m.
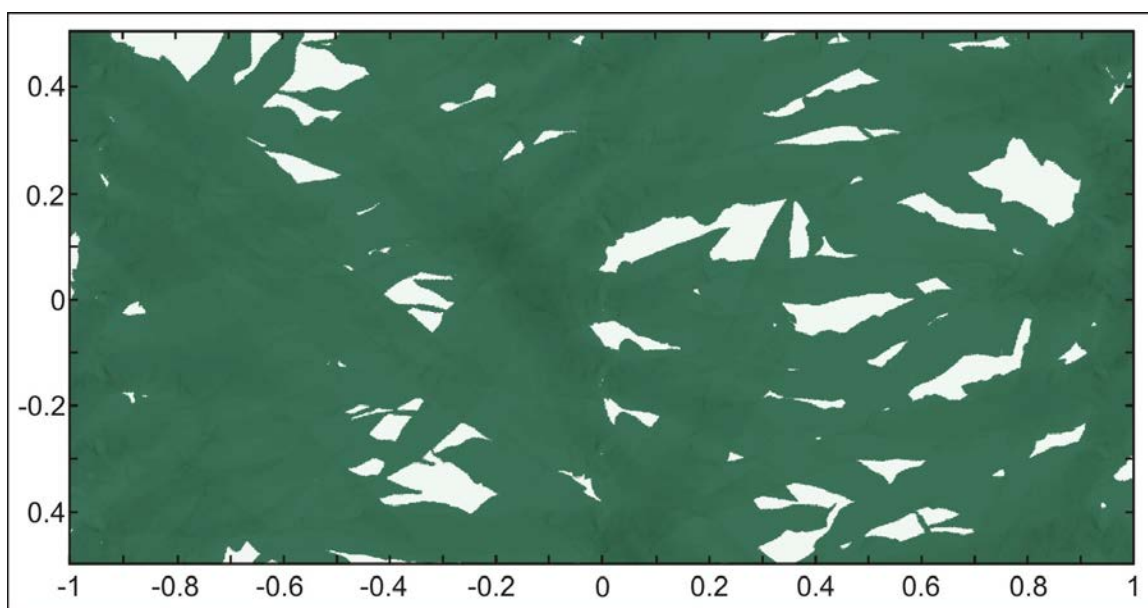
Figure V-19. Simulated top view of the final canopy. The plant density was 7.5 plants m^{-2}. The calculated gap fraction of the useable area (-0.5 m $\leq$ x $\leq$ 0.5 m and -0.5 m $\leq$ y $\leq$ 0.5 m) is 0.09,

The total leaf area inside the useable area was 5.04 m^2, which translates to a LAI of 5.04. The total projected leaf area, including leaf overlap, is 2.68 m^2, while the footprint of the plants is 0.91 m^2. This leads to a leaf overlap of 1.94 (defined here as the difference between projected leaf area and plant footprint divided by the plant footprint). The canopy coverage calculated for the canopy in the useable area is 0.91. Consequently,

the gap fraction is 0.09, which is approximately the same as the gap fraction above the disdrometer observed during the 2009 data acquisition campaign.

Figure V-20 shows the vertical leaf area distribution of the digital canopy. The cumulative leaf area, in this case defined as the plant area above the designated height, increases with decreasing height in a quasi-linear pattern from approximately 2.20 m to 0.5 m (the height of the lowest layer of leaves that remained attached to the plants).
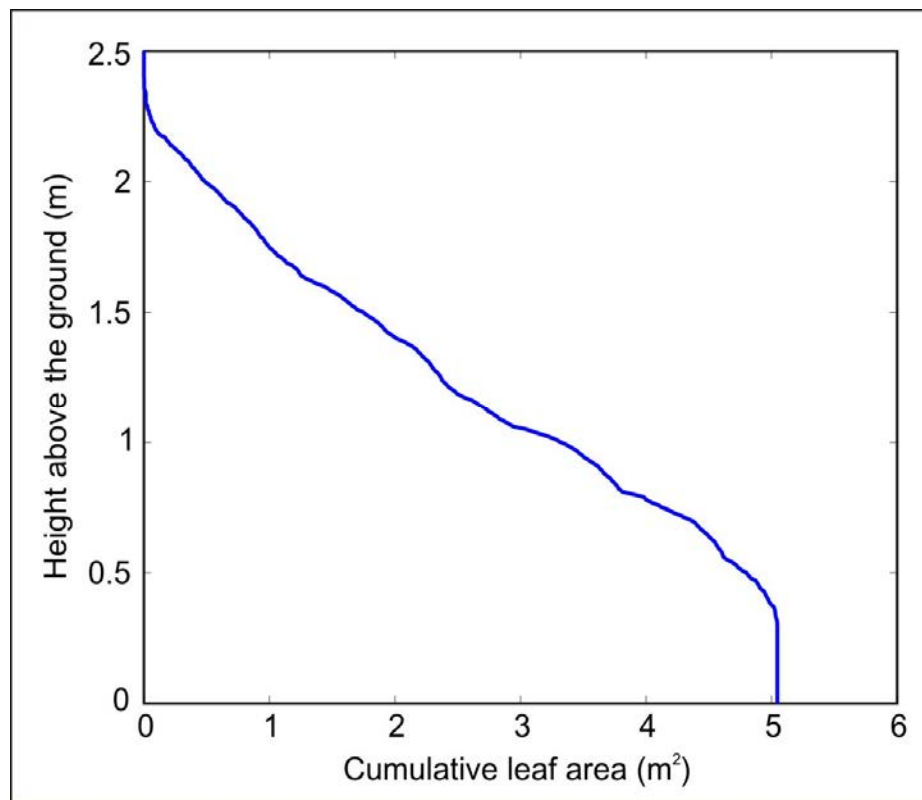
Figure V-20. Vertical leaf area profile. The curve shows accumulated leaf area located above the corresponding height inside a section of the canopy with 1 m^2.

Future Work

Although the photogrammetry based method presented here allows the creation of a realistic maize canopy, it is time consuming. Using this method to digitize a large

number of plants at different developmental stages would require great effort. Alternatively, Lidar has been used to digitize more complex canopies (Henning and Radtke, 2006; Hosoi and Omasa, 2006; Hosoi and Omasa, 2007; Omasa et al., 2007; Omasa et al., 2008; Van der Zande et al., 2010). This technology allows denser sampling of canopies with great accuracy; however, due to beam blockage, scanning must be done from multiple locations in order to fully cover the plants from all angles.

Point-clouds obtained with Lidar also need to be translated into leaves, stems, and other plant organs. Dornbusch et al. (2007) presented a methodology to delineate leaves and the stem from a cloud of points and demonstrated it on a barley plantlet (a 30 cm gramineous plant called *Hordeum vulgare L.*). Adapting their methodology to work with multiple plants and also recognizing that other plant organs such as the tassel and the ears could present an improved methodology to create three dimensional models of canopies.

In the development of this work, we used an arbitrary value for the maximum allowed deflection from the plant's preferential plane. Other techniques, such as the electromagnetic digitizing used by Sinoquet and Rivet (1997) are available but may lack the accuracy to trace the edges of a leaf. They may also have problems resolving difficult access areas, such as around the stem, which is the case for the Lidar based measurements. As demonstrated by Chambelland et al. (2008) a combination of techniques can be used to measure leaf orientation and the leaf geometry.

Following this line of thought, electromagnetic or sonic digitizing (Sinoquet et al., 1991) or other techniques can be used to measure the orientation of the leaves of many plants, allowing the study of the distribution of leaf azimuths and zeniths within a canopy. Azimuth limits taken from these measurements could lead to more realistic canopies than the ones created here. Alternatively, instead of calculating leaf orientation, we could use measured leaf orientations in an attempt to recreate a given canopy.

Another suggestion for future work is the automation of the gap fraction measurement technique and its comparison with other methods. With an automated

technique, the variability of the gap fraction within a canopy could be measured by sampling different areas of a low altitude aerial photograph. Such information is useful not only to the modeling of rainfall interception, but also to the light interception by a crop's canopy.

Conclusion

In this chapter, we described our efforts to create a three-dimensional digital representation of a maize canopy using a non-destructive photogrammetry based methodology. We produced five single plant digital models, two of them of the same plant at two different stages of development. The other three models were made from plants in the fields when we measured the partitioning of rainfall by a maize canopy during the 2009 and 2010 data acquisition campaign.

We selected the 2009 plant model and successfully created a section of the canopy containing 27 unique plants. Each plant comprises 13 leaves, which are identical copies of the 13 leaves digitized in the original single plant model. We calculated their orientation by assuming that leaves compete with neighbors that are at the same height or above and, consequently, maximize the canopy coverage. Resulting digital canopies displayed similar canopy coverage to their real counterparts.

CHAPTER VI.

MODELING THE PARTITIONING OF RAINFALL BY A MAIZE

CANOPY

Introduction

Predicting the total amounts of stemflow and throughfall based on canopy geometry and total rainfall is the first step towards understanding the partitioning of precipitation by vegetation. Modeling rainfall interception also provides insight needed to understand the collected data presented in CHAPTER III while aiding in the selection of the plant catchment area.

This chapter describes the development of a physics-based rainfall interception model capable of estimating stemflow, storage, and throughfall totals per storm and also the two-dimensional throughfall, drop-size, and velocity distributions. We present detailed results for the storm of 19 August 2009 to illustrate the model's development and capabilities. Later in the chapter, we discuss the results of the simulation of 10 storms that transpired in late July and August 2009 and compare them with data collected for that period. We end the chapter by assessing the impact of instrumental uncertainty on the model's estimates.

Methodology

The simulation works on a drop-by-drop basis and aims to predict the partitioning of rainfall into stemflow, throughfall, and canopy storage. Each hydrometeor is initially generated in a random location above the canopy, with its size and velocity taken from the corresponding set of disdrometer observations. Simulation steps entail drop generation, determination of interception, the tracing of potential drop trajectory, evaluation of re-interception, and the mapping of the location and drop characteristics of the hydrometeors that reach the soil surface. The flowchart presented in Figure VI-1 shows the general steps followed by the simulation.
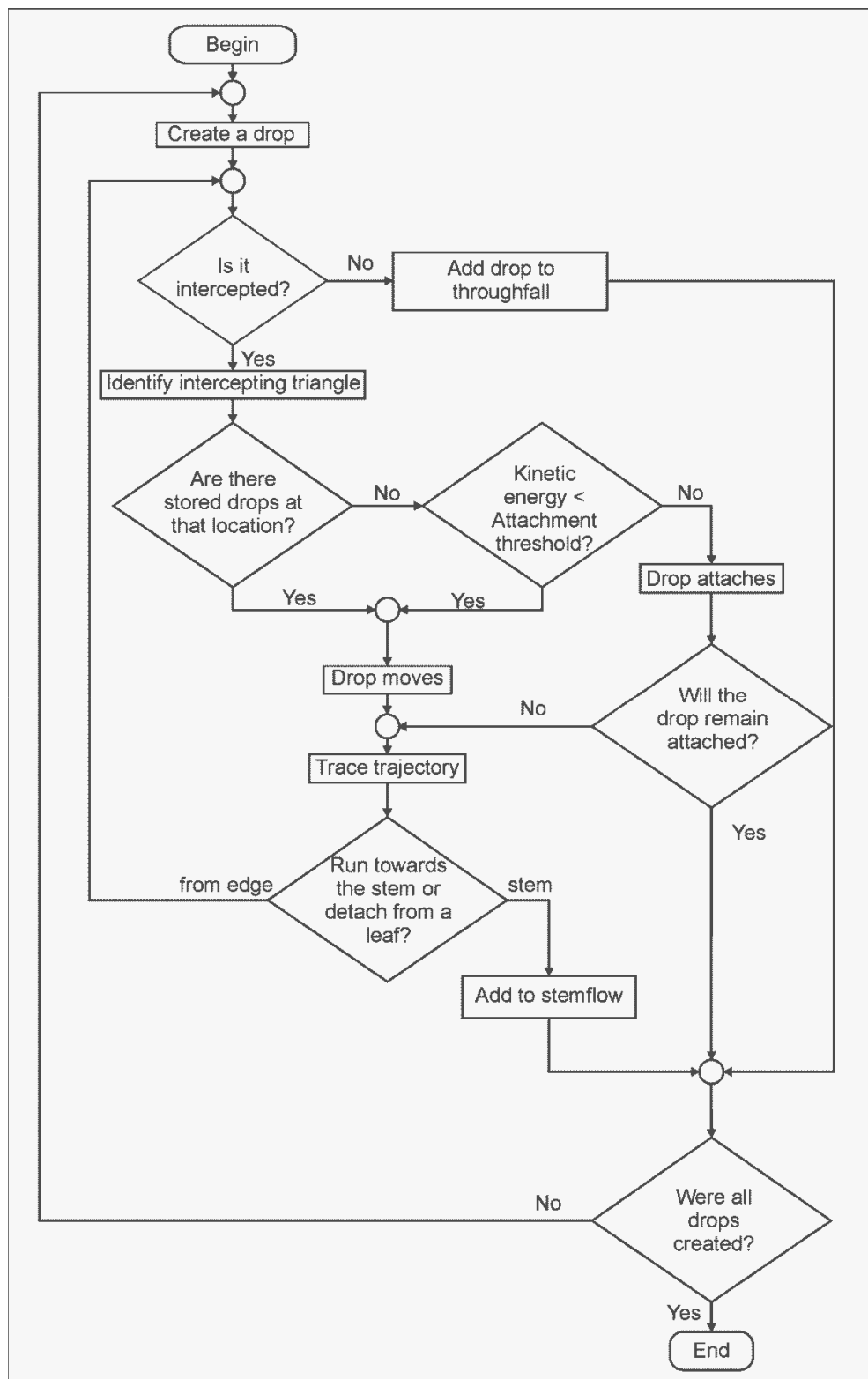
Figure VI-1. Simplified simulation flowchart showing the major steps of the interception process.

Raindrop interception

Deciding whether or not a drop is intercepted is a critical step in modeling rainfall partitioning by the canopy. This step could be as simple as comparing the coordinates of the raindrop to the coordinates of the vertices of each triangle in the canopy until we find the highest triangle that could intercept the drop. Even though the implementation of this procedure is straightforward and yields correct results, it can be optimized to reach the same products with fewer calculations by using pre-generated coverage matrices.

As defined in CHAPTER V, a coverage matrix is the matrix representation of a plant's or leaf's projection. Each element corresponds to a location on the chosen projection plane with its value dependent upon whether or not that location coincides with one of the projected triangles that forms the considered plant or leaf. Since the plants share leaf geometry and differ only in the coordinates of their stems and leaf orientation, there are only 13 unique leaf coverage matrices.

We created coverage matrices for the 13 original leaves and 1 for each plant. The local coordinate system associated with each leaf's matrix was centered on the middle of the stem and the leaves aligned with the north direction, *i.e.* the y-axis. We kept the full canopy coordinate system for the plant matrices and adjusted them to tightly fit the portrayed individual plant.

Drop interception evaluation takes place on two levels. First, we identify the plants that could intercept the drop; secondly, we pinpoint the leaf, which also provides us with the triangle id. Given the coordinates of the drop, we calculate the corresponding indices on each plant matrix. If the corresponding element has a value greater than one, that plant can intercept the drop. If none of the plants intercepts the drop, it is identified as direct throughfall.

If the drop is intercepted, we inspect the leaf matrices. For each examined leaf, we calculate the drop's local coordinates, which allows the identification of the corresponding element on the leaf's matrix. The coordinate transformation is achieved

by equation VI-1, where x_L and y_L are the local x- and y- coordinates, x_p and y_p are the drop's projected coordinates, $Az_{m,n,o}$ is the azimuth of the leaf o of the "nth" plant located on the row m, and , $x_{S,m,n}$ and $y_{S,m,n}$ are the coordinates of the stem of the plant m,n. Subsequently, we calculate the indices of the leaf's coverage matrix that correspond to x_L and y_L. If the matrix's value is greater than one, at least one of this leaf's triangle covers that point. As in the previous step, if the leaf matrix has a value of zero at the drop's location, the hydrometeor is not intercepted.

$$\begin{bmatrix} x_L \\ y_L \end{bmatrix} = \begin{bmatrix} \cos -Az_{m,n,o} & \sin -Az_{m,n,o} \\ -\sin -Az_{m,n,o} & \cos -Az_{m,n,o} \end{bmatrix} \cdot \begin{bmatrix} x_L - x_{S,m,n} \\ y_L - y_{S,m,n} \end{bmatrix} \tag{VI-1}$$

A triangle must fulfill three conditions to be selected as the drop's interceptor. First, when the drop and the triangle are projected on the horizontal plane, the drop must be inside the area defined by the three sides. The second condition is that the drop must be above the triangle plane. The third condition is that the selected triangle is higher than all triangles that meet the other two criteria. If no triangle meets these conditions, the drop is not intercepted by the canopy.

Tracing the drop trajectory on a leaf's surface

The trajectory of a drop moving on a leaf begins at the interception point and ends at the exit point. The exit point can be the stem of the plant, where it creates stemflow, the edge of the leaf, from which it can detach and be re-intercepted by a lower leaf, or the ground, where it becomes throughfall. A multitude of factors such as leaf geometry, drop size, and initial velocity, the leaf's trichomes' number, dimension, and current state, and other macro and microscopic leaf and drop characteristics contribute to the determination of a drop's trajectory. In our model, however, we assume that the drop's path is determined solely by the location where it was intercepted and by the geometry of the leaf.

To further simplify the calculation of the trajectories, we made two assumptions: we approximated the initial drop position by the centroid of the intercepting triangle, and we neglected drop inertia. Due to these two assumptions, there will be as many unique trajectories per leaf as there are elemental triangles delineating the leaf's surface. The limited number of trajectories allows their pre-calculation. Lead and intercepting triangle ids are the indices used to retrieve the trajectory of a drop once the conditions for its movement are met. Figure VI-2 shows the block diagram of the routine that calculates drop trajectories.

As a result of neglecting inertia, drop movement follows the direction of the steepest downward slope until the drop leaves the triangle through one of its sides. This direction is parallel and opposite to that defined by the gradient of the plane passing through the three vertices forming the examined triangle. To evaluate the plane's gradient, we first derived the equation of the plane (equation VI-2), whose parameters a_1, a_2 and a_3 are the components of the normal vector in the i, j, k directions (presented on equation VI-3), obtained through the cross product of the vectors that share vertex A as their origin and point to vertex B and C, respectively. The remaining terms of equation VI-2 are x_A, y_A and z_A, which are the coordinates of a point in the plane, in this case the coordinates of vertex A.

$$z = -\frac{a_1}{a_3}x - \frac{a_2}{a_3}y + \left(\frac{a_1 \cdot x_A + a_2 \cdot y_A + a_3 \cdot z_A}{a_3}\right) \tag{VI-2}$$

$$\boldsymbol{V_{AB}} \times \boldsymbol{V_{AC}} = [(y_b - y_a) \cdot (z_c - z_a) - (z_b - z_a) \cdot (y_c - y_a)]\boldsymbol{i} +$$

$$+[(z_b - z_a) \cdot (x_c - x_a) - (x_b - x_a) \cdot (z_c - z_a)]\boldsymbol{j} +$$

$$+[(x_b - x_a) \cdot (y_c - y_a) - (y_b - y_a) \cdot (x_c - x_a)]\boldsymbol{k} \tag{VI-3}$$

Finally, we calculate the vertical gradient of the plane described by equation VI-2, which is shown in VI-4.

$$\boldsymbol{\nabla z} = -\frac{a_1}{a_3}\boldsymbol{i} - \frac{a_2}{a_3}\boldsymbol{j} \tag{VI-4}$$
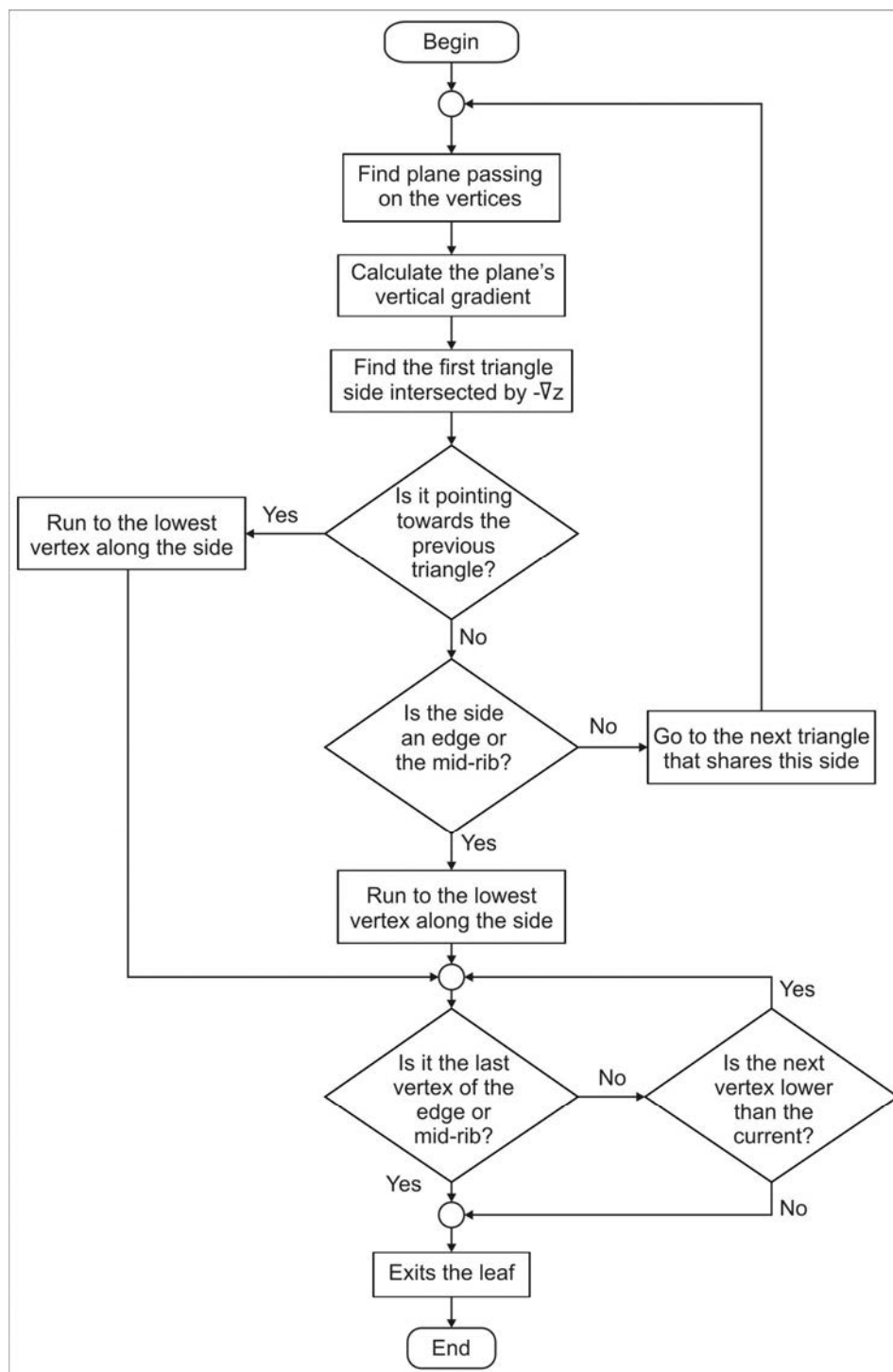
Figure VI-2. Block diagram of the routine that determines drop trajectories based on the initial position.

The steepest descent has the same direction and opposite sense of the vertical gradient, *i.e.* $a_1/a_3\,\boldsymbol{i} + a_2/a_3\,\boldsymbol{j}$. The next step is to determine which side of the triangle this direction points to. Figure VI-3 illustrates this process. The vector $-\nabla z$ (shown as the blue arrow) is located at the centroid of the triangle ABC, defining the curve (dashed blue line) represented by the parametric equation VI-5. Next, we find the parameters $t_{g\text{-}1}, t_{g\text{-}2}$, and $t_{g\text{-}3}$, which are the scalars that, when multiplied by the vector $-\nabla z$ and added to the point CG, will lead to the points P_1, P_2, and P_3, which lie on the sides AB (equation VI-6), BC (equation VI-7), and AC (equation VI-8), respectively. Since, for each set of equations, there are only two parameters to be determined, $t_{g\text{-}i}$ and t_i, equalities are two dimensional.
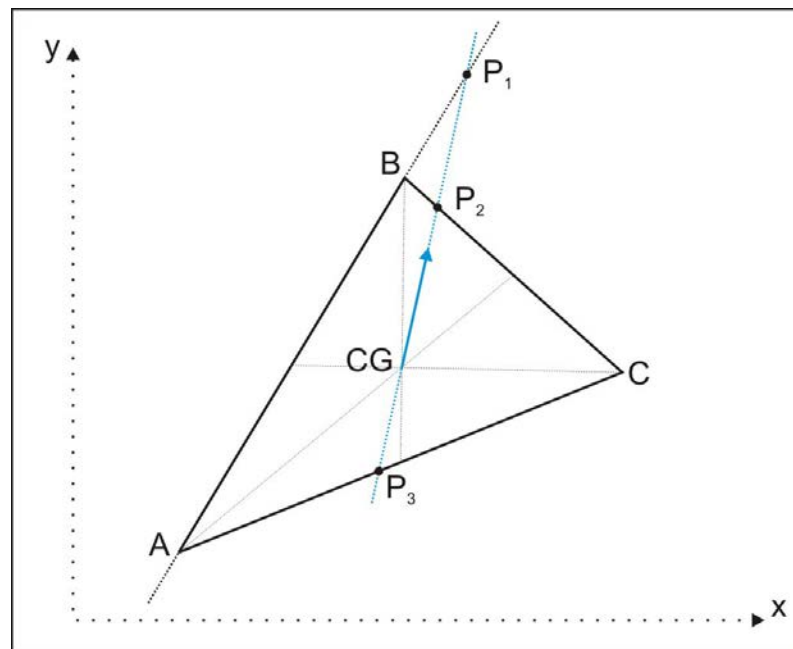
Figure VI-3. Illustration of the process of finding the exit side of the current triangle. The blue vector represents the direction of the steepest descent ($-\nabla\boldsymbol{z}$). The exit side is the one reached first when moving along the positive direction of $-\nabla\boldsymbol{z}$, in this example, side BC.

$$P = CG - t_g \cdot \nabla\boldsymbol{z} \qquad\qquad\qquad (VI\text{-}5)$$

Working on the x-y plane, one can find the points P_1, P_2, and P_3 by equating VI-5 with the corresponding two dimensional forms of equations VI-6, VI-7, or VI-8. Each pair of linear equations solved simultaneously lead to a pair of parameters, t_{g-i} and t_i. The point that requires the smallest positive multiplier t_{g-i}, is the point that is reached first, *i.e.* the point that lies on the side to which the gradient leads to. In the example shown in Figure VI-3, P_2 is the point we seek and the corresponding linear system of equations is presented on equation VI-9.

$$P = A + t_1 \cdot \left[(B_x - A_x)\boldsymbol{i} + (B_y - A_y)\boldsymbol{j} + (B_z - A_z)\boldsymbol{k} \right] \tag{VI-6}$$

$$P = B + t_2 \cdot \left[(C_x - B_x)\boldsymbol{i} + (C_y - B_y)\boldsymbol{j} + (C_z - B_z)\boldsymbol{k} \right] \tag{VI-7}$$

$$P = A + t_3 \cdot \left[(C_x - A_x)\boldsymbol{i} + (C_y - A_y)\boldsymbol{j} + (C_z - A_z)\boldsymbol{k} \right] \tag{VI-8}$$

$$\begin{bmatrix} -\boldsymbol{\nabla z}_x & -(C_x - B_x) \\ -\boldsymbol{\nabla z}_y & -(C_y - B_y) \end{bmatrix} \cdot \begin{bmatrix} t_{g2} \\ t_2 \end{bmatrix} = \begin{bmatrix} B_x - CG_x \\ B_y - CG_y \end{bmatrix} \tag{VI-9}$$

In equations VI-5 to VI-8, *P* stands for a generic point that lies on the current curve, A_x, A_y, and A_z are the x, y, and z coordinates of the vertex A. Similarly, B_x, B_y, and B_z are the coordinates of the vertex B, C_x, C_y, C_z and CG_x, CG_y, and CG_z are the coordinates of the vertex C and the centroid of the triangle, respectively. $\boldsymbol{\nabla z}_x$ and $\boldsymbol{\nabla z}_y$ are the x and y components of the vertical gradient of the plane passing through A, B, and C, and $\boldsymbol{i}, \boldsymbol{j}$, and $\boldsymbol{k}$ are unit vectors pointing on the x, y, and z directions.

Once we identify the side the drop should move to, we check to see if the current triangle has a neighbor that shares this side. If it has a neighbor on that side and the drop is not coming from there, the neighbor is assigned as the next triangle, and the drop is assumed to move to the point where the $-\boldsymbol{\nabla z}$ intersects the triangle side. The process is repeated, but this time the drop is assumed to be on the intersection point instead of the centroid of the triangle. If the direction of steepest descent points back to a triangle on which the drop was previously located, this indicates that the drop should actually flow

down the side of the triangle to the lowest vertex. This is usually caused by undulations on the edges of the leaf.

The third possibility is the $-\nabla z$ vector intersects a side that has no adjacent triangle, *i.e.* the edge or the mid-rib of the leaf. If that happens, we assume that the drop will be traveling down the mid-rib or the edge due to the channel like shape of the mid-rib or the adhesion between leaf edge and water droplet. It continues in this direction until its end for both mid-rib or leaf edge or until the next vertex is higher than the current vertex, which can happen on the edges of undulated leaves. If the drop exits from the base of the leaf, either by flowing down the mid-rib or by traveling on the edge of the leaf, we assign this drop to stemflow. If the drop flows towards the tip of the leaf or exits on the side of the leaf, we check to see if it is re-intercepted by another lower leaf. If not, this drop is assigned to indirect throughfall.

Drop breakup

Large drops can break into smaller fragments upon impacting the leaf surface, thereby altering the observed throughfall drop-size distribution. To account for this phenomenon, we implemented a drop breakup routine, with the occurrence of splashing based on the experimental work developed by Bassette and Bussiere (2008) and the droplets' size distribution based on the observations of Yang and Madden (1993).

Bassette and Bussiere (2008) describe an experiment where a 5200 mm^2 section of a banana leaf was exposed to simulated raindrops with diameters of 2.3 mm, 3.5 mm, and 6.0 mm released from varying heights and striking the leaf at varying impact angles. The analysis of the data allowed the authors to derive an empirical equation that estimates the fraction of the volume of the original raindrop that breaks into smaller droplets (K_s). Equation VI-10 gives K_s as a function of release height, h, drop diameter, D, and the parameters a, b, and c, which are function of D and the leaf inclination and are given in equations VI-11,VI-12, and VI-13.

If $2.3\ mm \leq D < 6$ and $h < 0.6\ m$, $K_s = 0$

If $2.3\ mm \leq D > 6$ and $h < 0.6\ m$, $K_s = \frac{a}{1+e^{-b\cdot[h-c]}}$ (VI-10)

$a(\theta, D) = (-0.008 \cdot D + 0.704) \cdot e^{(-0.01\cdot D + 0.004)\cdot \theta}$ (VI-11)

$b(\theta, D) = (-0.005 \cdot D + 2.956) + (-0.798 \cdot D + 8.214) \cdot e^{(0.002\cdot D - 0.018)\cdot \theta^2}$ (VI-12)

$c(\theta, D) = (-0.309 \cdot D + 1.958) + \frac{0.501\cdot D + 2.072}{e^{(0.0025\cdot D - 0.007)\cdot \theta^2}}$ (VI-13)

In Equation VI-10, the minimum release height resulting in enough kinetic energy to create splashing is 0.14 m for diameters 6 mm and above. Since our disdrometer measurements feature the size and falling velocity of drops, which is not directly compatible to the formulation of Bassette and Bussiere (2008), we used the method proposed by Wang and Pruppacher (1977) to calculate the fall height in still air that would lead a droplet to fall with the observed velocities. We precalculated the equivalent fall height of all the 440 diameter and velocity classes of the Thies disdrometer and used these heights in the computation of K_s.

After calculating the volume of the original raindrop that breaks into smaller droplets, the next step is to estimate the number and sizes of the fragments. Yang and Madden (1993) describe an experiment that evaluated the drop-size distribution of splashed droplets after hitting the ground or the surface of strawberry plants. The authors indicated that a Weibull distribution with a shape parameter of 0.296 and a scale parameter of 0.005 can represent the sizes of the droplet fragments. The distribution's parameters vary according to the leaf area index of the plants, with the median droplet diameter being 0.14 mm for a strawberry plant with a LAI of 2.2.

We attempted to simulate the breakup of drops and evaluate their interception in a realistic manner, assuming that the fragments would have diameters following the distribution shown by Yang and Madden (1993). However, considering that a single drop of 4 mm falling from 1 m could break into 800 new droplets and that for a test run

of 10 mm a total of 205,000 drops met the drop breakup criterion, the added computational cost proved to be too high.

To circumvent these calculations, we assumed that all fragments follow the same path. Their interception and redirection is evaluated in the same fashion as a regular drop, with the exception that no further breakup is allowed. If their trajectory leads to stemflow, we simply count the volume of all droplets as stemflow. If their trajectory indicates throughfall, we add all of their volume to the same location and add the number of drops to their corresponding diameter classes in the throughfall drop size counter.

Conditions for movement

Upon impact, we examine the kinetic energy of the incoming drop and the existence of a stagnant drop on the impact location. We assumed four different scenarios. In the first, the drop hits a vacant location of the leaf; however, it lacks enough kinetic energy to attach to it. In this case, the drop rolls. In the second case, the drop's kinetic energy exceeds the free surface energy, in which case Nosonovsky and Bhushan (2008) proposed that the drop attaches to the leaf. In the third scenario, the drop impacts the leaf on a location previously occupied by a stagnant drop; nevertheless, the kinetic energy of the impacting drop is not enough to overcome the adhesion force between the stagnant drop and the leaf surface. In this case, the two drops merge and remain stagnant. In the final case, the kinetic energy of the impacting drop suffices to initiate the movement of the merged drops.

Equation VI-14 defines the threshold between the first and the second scenarios. If the drop velocity is higher than the velocity limit (V_{Lim}) shown in equation VI-14, then the Cassie-Wenzel transition should occur, causing the droplet to stick to the surface. Alternatively, the drop would remain in the Cassie state, which is associated with low contact angle hysteresis and low friction that lead to drop movement. The remaining

terms of equation VI-14 are   , the surface tension between water and air, $_w$, the water density, and D, the drop diameter.

$$V_{Lim} = \sqrt{\frac{12 \cdot \sigma}{\rho_w \cdot D}} \tag{VI-14}$$

Once a drop adheres to the surface, the associated energy barrier that needs to be overcome is determined by the adhesion hysteresis. As described by Nosonovsky (2007), the energy stored when two surfaces come in contact exceeds the energy required for their separation, constituting the adhesion hysteresis. More energy is required for the front of the drop to move forward and attach to the surface than is freed during detachment on its back. Equation VI-15 gives the extra work per unit area required to break this barrier (ΔW_o). The other terms are $_{a0}$, which stands for the advancing contact angle, $_{r0}$, which stands for the receding contact angle, and   , which stands for the surface tension between water and air.

$$\Delta W_0 = (\cos \theta_{a0} - \cos \theta_{r0}) \cdot \sigma \tag{VI-15}$$

We used the values of 143° and 135° for $_{a0}$ and $_{r0}$, measured by Watanabe and Yamaguchi (1993), to calculate ΔW_o. Furthermore, we assumed that when a falling drop collides with a stationary one, if the kinetic energy for the descending hydrometeor is equal to or greater than $A_0 \cdot \Delta W_o$, where A_0 is and the contact area between the stationary drop and the leaf surface, the combined drops will move. Otherwise, the two drops will merge and remain stagnant at the impact's location. We employed the contact area formulation of Hartley and Brunskill (1958), which we show in equation VI-16:

$$A_0 = \left(\frac{4}{3}\right)^{2/3} \cdot \pi \cdot r^2 \cdot \left[1 - \cos \theta + \frac{1}{3}(\cos^3 \theta - 1)\right]^{-2/3} \tag{VI-16}$$

In equation VI-16, r stands for the drop radius and   for the equilibrium contact angle.

Conditions for drop coalescence

Since we do not keep track of the stationary drops' coordinates, but only on which elemental triangle they are located, we base the drop coalescence test on triangle ids. Whenever a moving drop crosses a triangle containing a stagnant drop, we calculate the probability of drop coalescence by comparing the diameter of the moving drop to the free space on the triangle's surface, *i.e.* the difference between the maximum triangle dimension, measured perpendicularly to either the mid-rib or the leaf edge and depending on which of the two coincides with a triangle side, and the stagnant drop's diameter.

Equation VI-17gives the merging probability (P_m), where h is the referred triangle height, D_s is the diameter of the stagnant drop, and D_m is the diameter of the moving drop. If the two added diameters are larger than h, then we assign a value of one to P_m.

$$P_m = \frac{D_m}{h - D_s} \qquad\qquad (VI-17)$$

For each occurrence, we draw a random number from a uniform distribution bounded to the [0,1] interval. If this random number is lower than or equal to P_m, the two drops merge.

Results and discussion

Partitioning of rainfall into stemflow and throughfall

neglecting water retention

In order to check the validity of the assumption that drops begin their trajectory in the centroid of the intercepting triangle and to assess the potential impacts of this assumption on the partitioning of rainfall into stemflow and throughfall, we implemented simplified calculations that neglect plant water storage. We executed two simulations, one that retraced the drop trajectory for each drop, using the location where the initial triangle intercepted the drop as the starting point, and another that placed hydrometeors at the centroid of the intercepted triangles. This test not only allowed the assessment of the

impact of the simplification on the accuracy of the simulation, but also resulted in a noticeable decrease in computation time.

The two simulations used identical canopies comprising an area of a 1 m^2. We created a regular grid of square elements with 5 mm sides and released a drop from the center of each of these elements. We evaluated the interception and re-interception of the drops and traced their trajectory using the methodologies described earlier in this chapter to evaluate which drops resulted in stemflow and which resulted in throughfall. The latter was subdivided into throughfall that fell inside the study area and throughfall that was redirected out of bounds. We also estimated the location where throughfall drops reached the ground and their counts at each position in order to provide contrast with the canopy cover and search for dripping locations.

We generated the first set of results without the assumption that drops always begin their trajectories in the centroid of the intercepted triangle in 8076 seconds. From the 40401 examined locations, 4431 resulted in drops being carried outside of the study area, 25104 in throughfall drops falling inside of the 1 m^2 plot, and 10866 in drops redirected to the stem of the plants. Percentagewise, throughfall corresponded to 62% of the incoming drops and stemflow to approximately 27%.

Figure VI-4 shows the spatial distribution of the areas that resulted in inbound throughfall, stemflow, and out of bounds throughfall. As expected, most of the area that removed water from the study area was located on the periphery of the plot, with the exception of a section in the mid-south of the figure that was caused by a long north-south lying leaf. Figure V-5 shows what happens beneath the canopy. By contrasting the simulated top view of the canopy with the throughfall locations, we see that the calculations correctly predicted that uncovered areas would coincide with single drop throughfall locations. We can also observe several isolated points showing considerably higher throughfall drop counts. These are the locations of indirect throughfall, where drops detach from leaves.
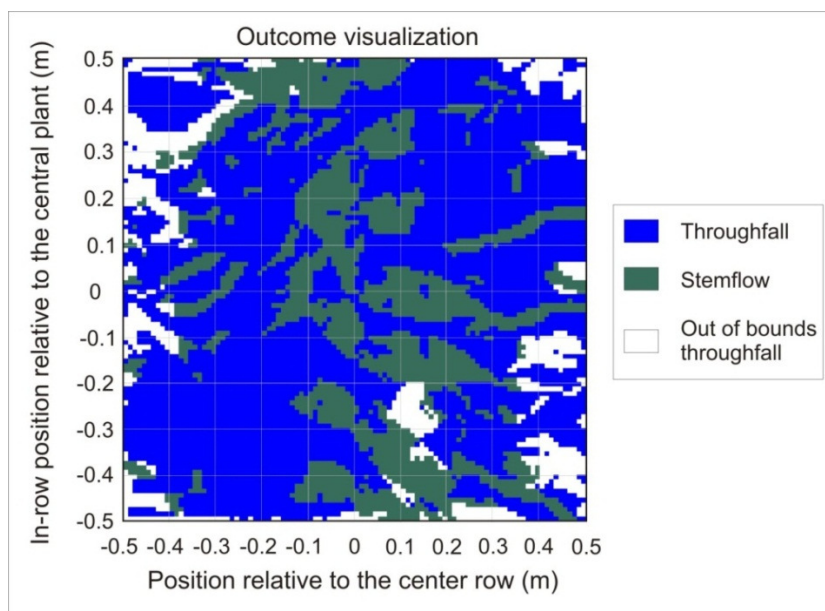
Figure VI-4. Spatial distribution of the locations resulting in stemflow, throughfall and out of bounds throughfall. Drop trajectories were recalculated depending on the interception location. Pixels correspond to 5 mm by 5 mm squares.
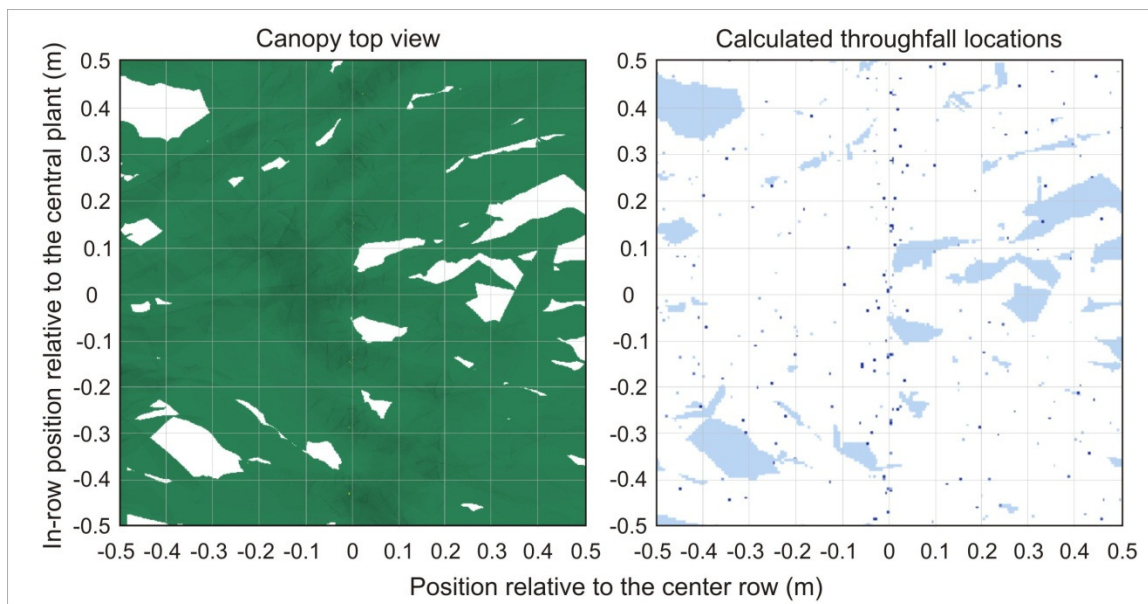
Figure VI-5. The right panel shows the spatial distribution of the throughfall under the canopy. Lighter colors stand for lower drop counts, while darker shades of blue are associated with higher counts. The left panel shows the corresponding canopy cover.

Finally, Figure VI-6 shows how the stemflow varies along the row located in the center of the study area. The lower percentage displayed by the first and the last two plants are primarily due to most of their area being located outside of the plot where rainfall was simulated. In the next simulations, we generate rainfall over a larger area to minimize edge effects.
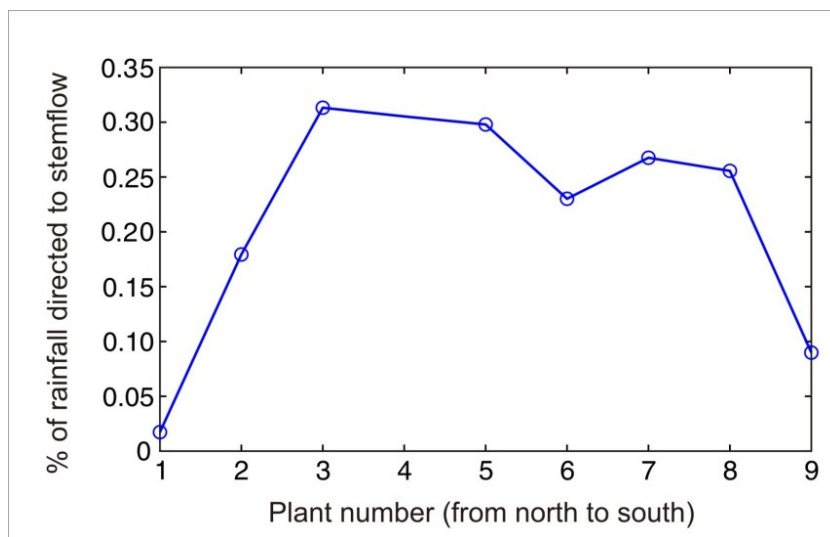
Figure VI-6. Counts of drops reaching each plant stem in the center row. The low counts of the first and the last two plants are due to most of their area being outside of the study location. Therefore, they did not receive rainfall.

The second set of results was generated in a shorter time, 6878 seconds. This computation employed precalculated routes indexed by the id of the intercepting triangle. Throughfall counts for the second simulation totaled 25185, which corresponds to a difference of 0.3% with respect to the previous model. Stemflow counts were also quite close, with the simplified version leading to 10814, while the previous result was 10866. The similarity in the results indicates that the simplification is acceptable.

Evolution of the model

As we proceeded to simulating entire storms, we noticed that the computation time was still too high. Even when assuming that drops always begin their trajectory in the centroid of the intercepting triangle and ignoring drop splashing, the time to process a single drop was on average 16 ms using a personal computer featuring an Intel i7-920 processor® set at 2.8GHz running Matlab 2011a. Most of this time was devoted to the routine that identifies the intercepting triangle. When simulating a storm with approximately 15 mm of rainfall in a plot of 1 m by 1 m, we would have approximately 27 million drops. This would take 120 hours to process.

We have two possible avenues: the first is to parallelize the routine that identifies the intercepting triangle; the second is to modify the leaf coverage matrix to hold the identity of the intercepting triangle on each of its pixels. This way the task of identifying the triangle is reduced to identifying which pixel corresponds to the drop position.

While parallel computing has the potential to decrease the computation time in this routine, foreseeing the performance gain is not straight forward. We identified a loop in the routine that is a good candidate for parallelization. This loop determines whether a point's projection is inside the projection of a given elemental triangle forming a leaf. Since each triangle of a given leaf is examined independently of the others, this task can be assigned to multiple processor cores. One shortcoming is that once the highest intercepting triangle is located, all other triangles in the current leaf still have to be checked since the iterations are independent and cannot be flagged to stop. Although assigning parts of the loop to run in multiple cores will save calculation time, it comes at the expense of having to pass the information multiple times.

Without considerable changes, the vectors cannot be sliced due to the way we chose to store the information on leaves by using triangles and vertices, *.i.e.* we passed only the sections of the vectors that will be used to each of the workers in order to avoid

replication of information. The time expenditure could outweigh the performance gain promoted by the division of the task.

These reasons led us to pursue the other alternative of modifying each leaf coverage matrix. Since the importance of these matrices grows with this new use, we refined their resolution and rebuilt their pixels to cover an area of 0.5 mm by 0.5 mm. In each pixel, we saved the id of the highest triangle that included the pixel's centroid. We reconstructed the 13 matrices with each leaf pointing to the north and with the stem centered at the origin of its local coordinate system. With this modification, the task of identifying which triangle intercepts the given drop is simplified to a coordinate system transformation followed by determining which pixel includes the drop. Finally, we retrieved the id of the triangle from the matrix.

Although this change decreased the computation time to 3 ms per drop, it could have rendered some triangles unreachable. Nevertheless, each pixel is as small as 0.5 mm by 0.5 mm, which is smaller than the expected uncertainty of the photogrammetry method. Therefore, we chose this approach for our simulations.

To demonstrate the evolution of the interception model, we present the partitioning results using three versions of the simulation for the 19 August 2009 storm. During this event, the reference disdrometer recorded 102,000 drops. When scaled to the simulation area, this totals over 27 million drops resulting in 16 mm of accumulated rainfall. The second disdrometer installed under the canopy recorded 5.86 mm of throughfall coming from 11 million drops after scaling to the simulation area.

In the first version, we did not simulate drop breakup and used simpler conditions for drop movement and coalescence than the ones described in the methodology. In this initial version, the drop movement criteria was that if a drop impacted an elemental triangle that contained another drop, the two drops would merge and move. If the triangle was not currently holding a drop and if the fall velocity was high enough to promote attachment, the drop would adhere to the leaf. If the drop moved, we assumed

that it would merge to any drops stationed on triangles located along its trajectory. Figure VI-7 shows the drop count in each diameter bin obtained with the reference disdrometer, the throughfall disdrometer, and this version of the simulation.
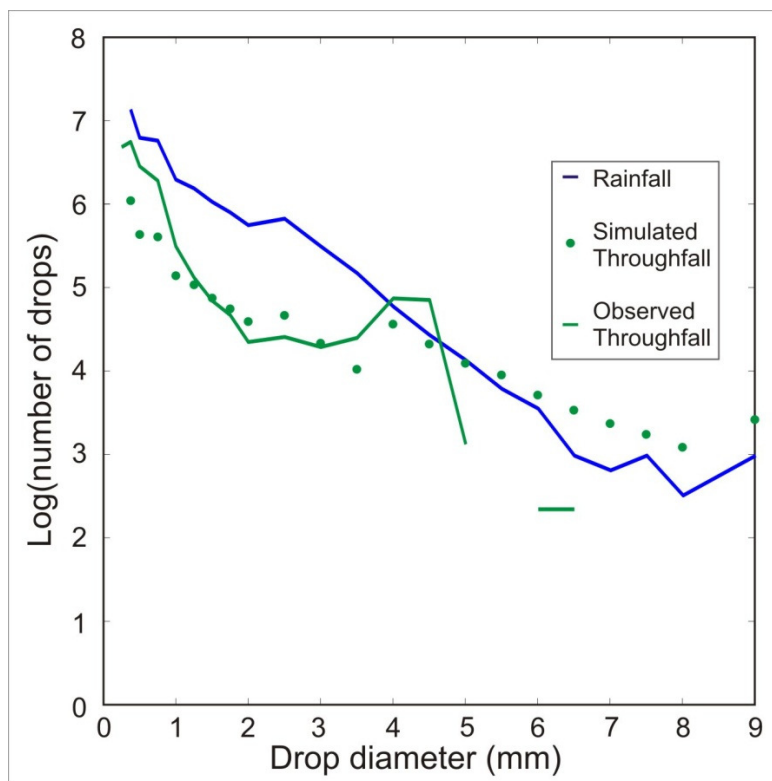
Figure VI-7. Drop count in each diameter class observed in the simulated throughfall, measured rainfall, and measured throughfall for the 19 August 2009 storm. Simulation results generated with the first version of the interception model neglected drop breakup and used simplified movement rules.

Even though the first version of the model already included a drop attachment threshold based on the drop's kinetic energy, the number of small drops predicted by the model was considerably lower than the number observed. This motivated us to look at drop breakup routines, which ultimately led us to the works of Yang and Madden (1993), who studied the distribution of drop fragment sizes produced by the splashing of drops on

leaf surfaces, and Bassette and Bussière (2008), who described the conditions necessary for drop breakup to occur, as well as the volume of the fragments. Using the results of these two works, we developed the routine described in this chapter's methodology. Figure VI-8 shows the resulting counts of throughfall drops on each diameter class after incorporating drop breakup and splashing.
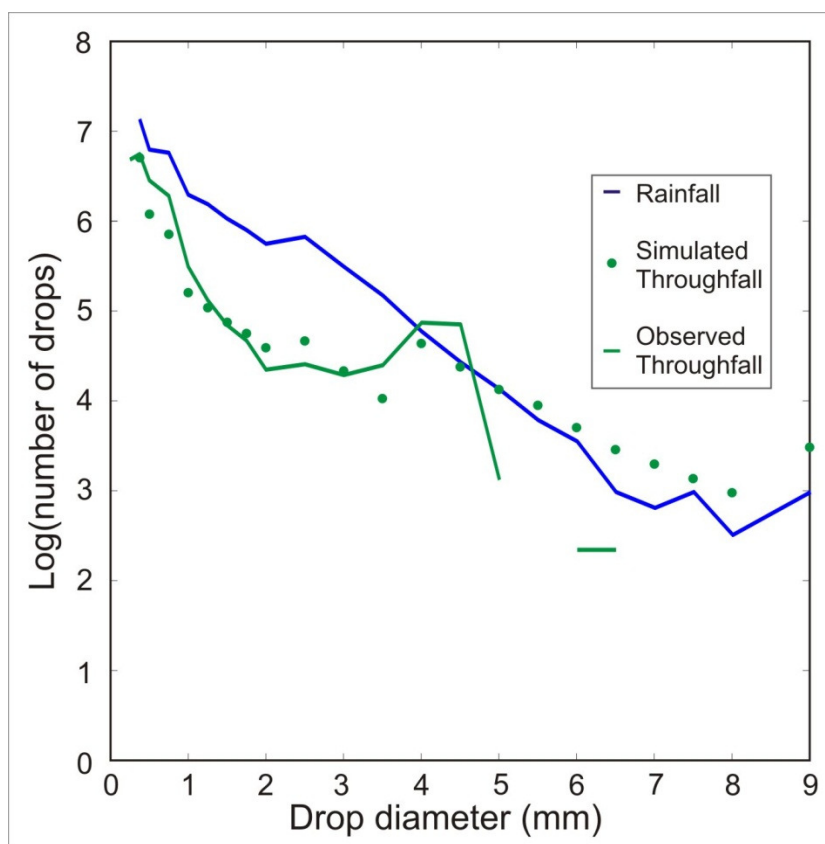
Figure VI-8. Counts of drops in each diameter class featured in observed and simulated throughfall for the storm of 19 August 2009. This model's version includes drop breakup.

Incorporating drop breakup greatly improved the estimation of the number of throughfall drops with diameters smaller than 1 mm. However, it did little to enhance the agreement between the number of drops with diameters larger than 5 mm predicted by

the model and those observed with the disdrometer during this sample storm. Furthermore, the volume of stored precipitation was only 0.12 mm, which is considerably lower than the value of 0.385 mm estimated by van Dijk and Bruijnzeel (2001b).

Comparing the drop counts with diameters in excess of 5 mm registered by the throughfall disdrometer with the simulation results indicated that we were overestimating the occurrence of moving and stationary drops merging. We attempted to address this issue by assigning a probability that two drops would come in contact according to the diameters of the drops and the dimensions of the elemental triangle that held them.

According to this methodology, the probability of a 0.2 mm drop merging with stagnant drops with diameters ranging from 0.125 mm to 9 mm while crossing a triangle 50 mm in height varies from 0.004 to 0.0048. The corresponding range of probabilities for a 1 mm drop goes from 0.02 to 0.0238, while a 5 mm moving drop faces merging probabilities of around 10%.

The low predicted storage capacity indicated that the movement conditions were too easily met. We added further constraints based on the kinetic energy of the impacting drops following the theory presented by Nosonovsky (2007). Equation VI-15, presented in the methodology section on page 105, gives the minimum kinetic energy that a falling drop requires to mobilize a stagnant one.

For example, for a surface tension of 0.072 N/m and receding and advancing contact angles of 135° and 143°, respectively, a 0.125 mm drop requires an energy of 8.3×10^{-11} J. On the other hand, for the same parameters, a 3 mm drop requires 4.8×10^{-8} J to be mobilized. Meanwhile, a moving drop 0.4 mm in diameter falling with the Gunn and Kinzer terminal velocity (Gunn and Kinzer, 1949) has a kinetic energy of 4.4×10^{-8} J, slightly below the calculated limit to mobilize a 3 mm drop.

Table VI-1 presents a comparison of the stemflow, throughfall, and storage predicted by the three versions of our model. As expected, predictions using the final model show higher canopy storage estimates. However, the model still predicts a large

number of drops with diameters in excess of 5 mm as seen in Figure VI-9. In order to

check the stability of the results, we ran the final version of the model three times. Table

VI-2 shows no significant difference between runs, indicating that the differences

observed in Table VI-1 are caused by the incorporation of new phenomena into the

simulation.

Table VI-1. Predicted storm totals using two intermediate and the final version of the
presented interception model for the storm of 19 August 2009.

	Initial version	Intermediate version	Final version
Rainfall	16.18	16.18	16.18
Stemflow	7.49	7.78	7.11
Throughfall	6.37	8.32	8.83
Storage	0.12	0.17	0.18

Table VI-2. Results of three runs using the final version of the rainfall interception
model for the 19 August 2009 storm.

	First run	Second run	Third run
Rainfall	16.180	16.180	16.180
Stemflow	7.107	7.108	7.130
Throughfall	8.830	8.834	8.811
Storage	0.184	0.191	0.185

To better compare the results of the three different rainfall interception models,

we composed Figure VI-10, which shows the ratio between the number of drops

predicted by the first and final models in the left plot and the ratio between the number of

drops predicted by the second and final models in the right. The horizontal dashed line

represents a ratio of one, which is where the two models agree. Values below this line

imply that the final version of the model predicted higher counts at that diameter class.
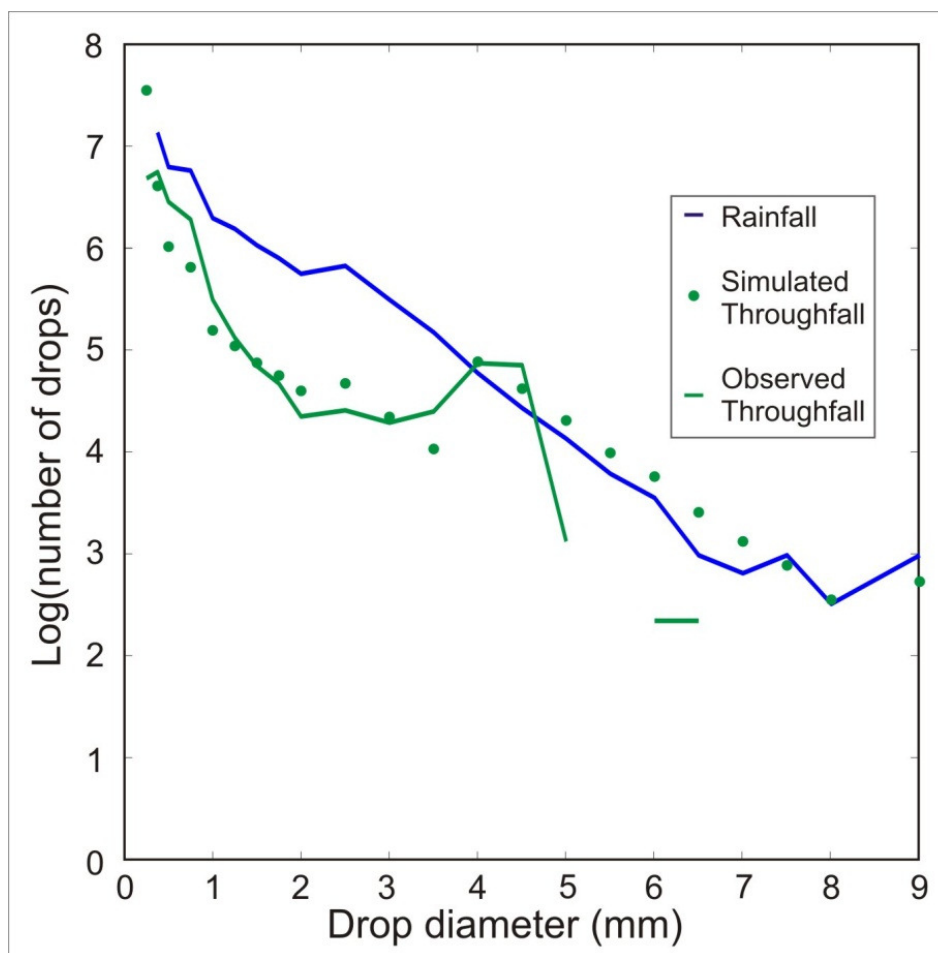
Figure VI-9. Counts of drops in each diameter class featured in observed and simulated
throughfall for the storm of 19 August 2009. This model's version includes
drop breakup, probability of coalescence calculations, and minimum energy
threshold necessary to mobilize a stagnant drop.

Upon examination of the left plot that compares the first and the final models in

Figure VI-10, we see that the final model predicted more drops with diameters smaller

than 1 mm and also in the range between 3.5 mm and 6 mm. This plot also indicates that

neglecting drop breakup and using simplified rules for drop merging and mobilization

yields higher counts of drops larger than 6 mm. Comparing the second and the final

models, we observe a sharp decrease in the number of drops with diameters exceeding

9 mm. This exceeds the decrease that occurred when comparing the first and the final

models and indicates that drop breakup is not the dominant phenomena limiting the

formation of drops in this class. However, the inclusion of the drop breakup routine

(from the first to the second versions) did cause a decrease in the number of drops with

diameters ranging from 6 mm to 8 mm.
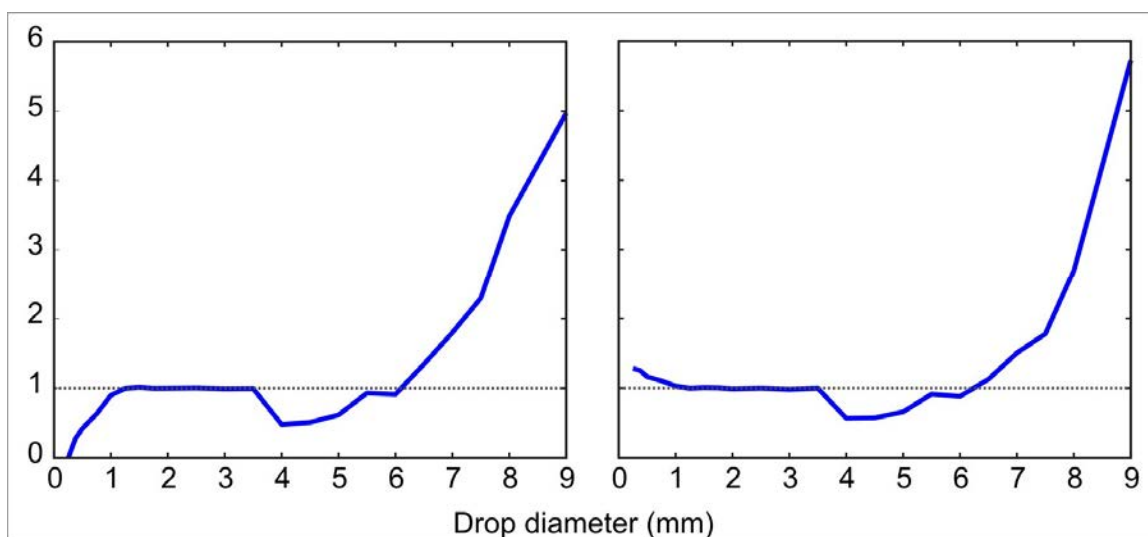
Figure VI-10. Comparisons of the predicted number of drops in each diameter class by the three models. The horizontal axis shows drop class diameter, while the vertical axis shows the ratio between the number of drops predicted by the first and final models (left plot) and the corresponding ratio for the second and final models (right plot).

Comparing the second and the last versions (right plot Figure VI-10), we observe

a small decrease in the counts of drops with diameters smaller than 1 mm in the final

model. This could be the reflex of the splashing of re-intercepted large drops. Drops

larger than 6 mm are present in lower numbers in the final version. These are the drops that can splash even after short falls, *e.g.* falling from 0.14 m instead of 0.6 m, which is the threshold for 2.3 mm drops. The splashing of re-intercepted drops should be less frequent, which would cause the slight decrease of small drops. The decrease of large drops observed from the second to the final models was caused by the introduction of the probability of drop merging. Lower frequency of merging offers fewer opportunities for drop growth, and thus leads to smaller drops.

The introduction of the minimum kinetic energy required to mobilize a drop didn't lead to a significant change in the interception capacity. The small difference observed in the storage height estimated by the second and the final models shown in Table VI-1 are comparable to differences that occur when the same run is repeated, as shown in Table VI-2.

<div align="center">

Estimating the partitioning of rainfall into stemflow,

throughfall and plant water storage

</div>

To demonstrate our model's potential, we discuss in detail the results obtained for the storm that occurred on the evening of 19 August 2009. The storm began at 16:40 and transpired until 17:40, local time, resulting in an accumulation of 16.2 mm according to our reference disdrometer. During the same period, our two stemflow and two throughfall gauges were operational, with their results shown in Table VI-3. Meanwhile, the rain gauge located outside of the canopy registered 11.4 mm of rainfall.

Also included in Table VI-3 are the simulation results for the same period. The value for total rainfall is different than those observed, as they were measured by different instruments. In order to minimize the influence of this discrepancy, we included the fraction of total rainfall for each of the components of rainfall on the canopy. Comparing the fraction of throughfall measured during the experimental stage to the

simulation result, we see that the model predicted higher throughfall and stemflow

fractions.

Table VI-3. Summary of the data collected in the storm of 19 August 2009 and
comparison with the simulated results.

	Experimental results			Simulated results	
	Total height (mm)	Fraction of total rain		Total height (mm)	Fraction of total rain
Total rainfall	11.4	1.0	Rainfall	16.2	1.00
Throughfall 1	4.7	0.4	Throughfall	8.8	0.54
Throughfall 2	3.8	0.3			
Stemflow 1	3.1	0.3	Stemflow	7.1	0.44
Stemflow 2	2.3	0.2			
Unaccounted volume	4.5	0.4	Storage	0.2	0.01

Figure VI-14 shows the two-dimensional throughfall distribution. Each pixel represents a 1 cm by 1 cm square of soil. Hotter colors represent larger quantities of rain water reaching that spot. Comparing the throughfall locations with Figure V-19, we notice a good correspondence between the openings in the canopy and the first class of throughfall accumulations. Since we assumed the raindrops fell vertically, these areas receive water solely through direct throughfall.

The model predicts that a large fraction of the area doesn't receive throughfall. Intercepted rainfall from those locations constitutes a source of water for indirect throughfall, stemflow, and storage. Higher amounts of throughfall are visible under the canopy, especially under the tips of leaves and close to the stems of the plants. The concentration of rainfall in those locations is due to dripping, *i.e.* indirect throughfall, which occurs in localized spots and could be a source of erosion under the crop foliage.
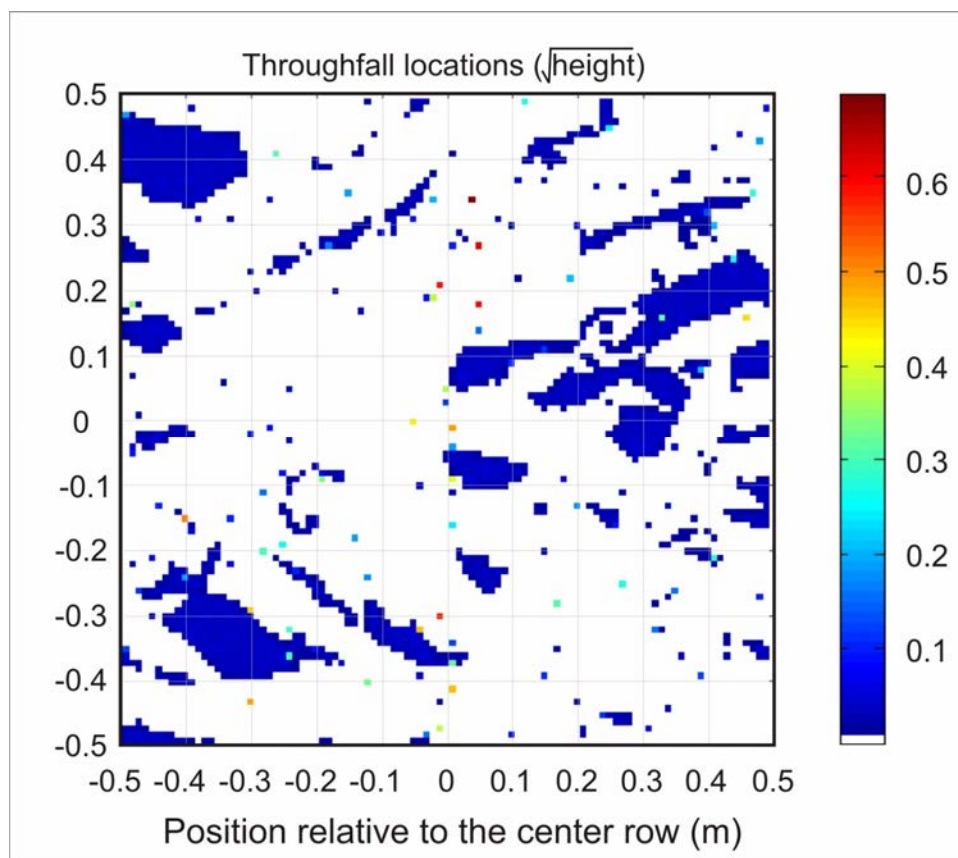
Figure VI-11. Two-dimensional throughfall map. Pixels are color coded according to the square root of the height of throughfall at their location.

The concentration of throughfall around the stems could explain some of the disagreement between simulated and measured throughfall fraction. The design of the throughfall gauges prevented the collection of water between stems. Because the canopy coverage is higher in the vicinities of the stems, we did not anticipate considerable throughfall to transpire there. However, our simulation indicated that dripping around the stem can be significant, accounting for approximately 13% of the total throughfall, as shown in Figure VI-12. This plot shows how much throughfall reaches the soil as a function of the distance from the center of the row. Each bar corresponds to 10 mm in distance. Since the stem of the plants at the height of the throughfall collectors was

approximately 20 mm, we can assume that these areas were not sampled by our gauge, which corresponds to the two bars in the center of Figure VI-12.
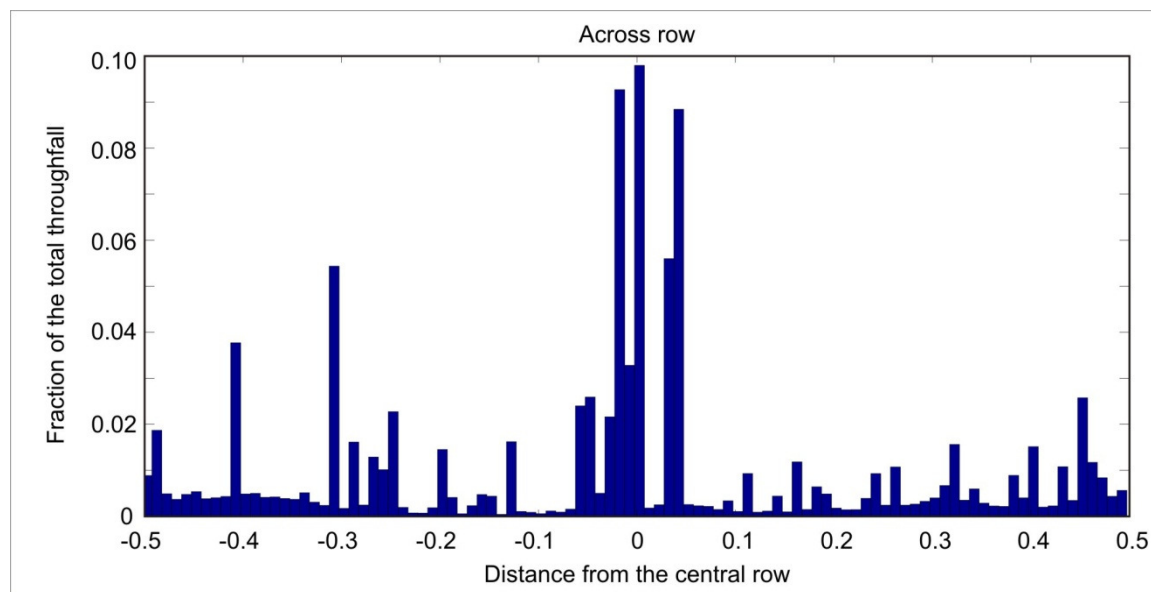
Figure VI-12. Distribution of the fraction of rainfall transformed in throughfall with respect to the distance from the center of the row.

Stemflow measurements presented in CHAPTER III shows variation from plant to plant. This variation is also predicted by the interception model. Figure VI-13 shows the fraction of rainfall transformed into stemflow for each plant in the central row. Because the first and the last plant in this row were not completely inside the study area, they should be ignored. However, we observe variation in the predicted stemflow fraction. The estimated stemflow in the first plant to the south of the central plant (numbered -1) corresponds to approximately 41% of the total rainfall in its domain, *i.e.* an area of 0.94 m by 0.143 m centered on the plant's stem. However, the stemflow of the third stem to the north of the central plant accounted for almost 50% of its rainfall.

Despite the variation observed in the simulated stemflow, it is unlikely that insufficient sampling could explain the difference between simulation and measurements. In the literature review of storage capacity methods presented by van Dijk and Bruijnzeel (2001b), the authors observed that a considerable storage volume occurs around the leaf insertion point, even though these areas are impervious to water (Kiesselbach, 1949). Because we did not model the storage of water on the leaf interception points and because storage in such areas would primarily affect the stemflow amounts, we believe that the underestimation of rainfall storage in such areas is the cause for the overestimation of the stemflow amounts.
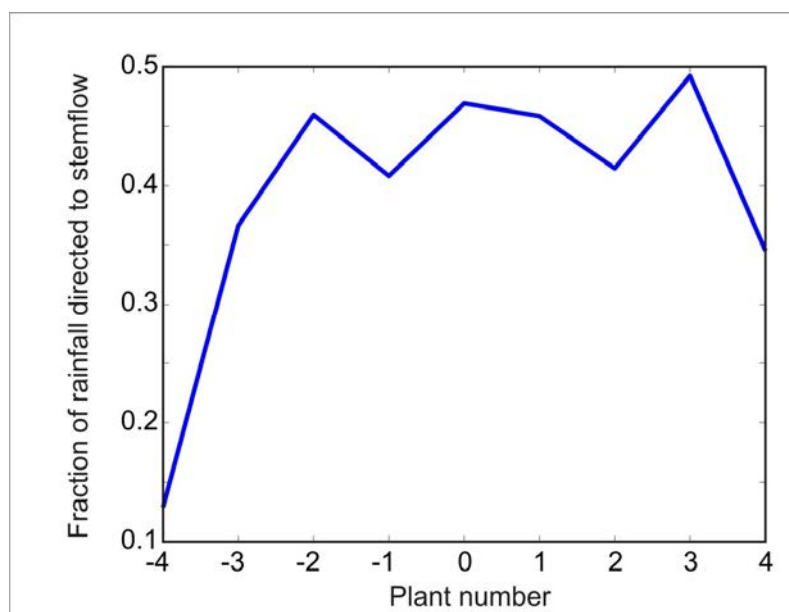
Figure VI-13. Distribution of the fraction of rainfall transformed in stemflow for each plant in the center row. The first and the last plants had considerable area lying outside of the simulation area, which explains their lower fractions. Plants are numbered in reference to the central plant of the central row.

Let us return to Figure VI-9 to examine the prediction of the throughfall drop-size spectrum. This plot shows how the distribution of simulated throughfall drop sizes

agrees with disdrometer observations. The discontinuity in the observed throughfall line stems from having no observed drops in the corresponding classes. By storing the location of drops with diameters in excess of 6 mm, we found that they are most likely to happen in the locations where leaves overlap the most. Figure VI-14 shows the predicted location of these drops during the 19 August 2009 storm.
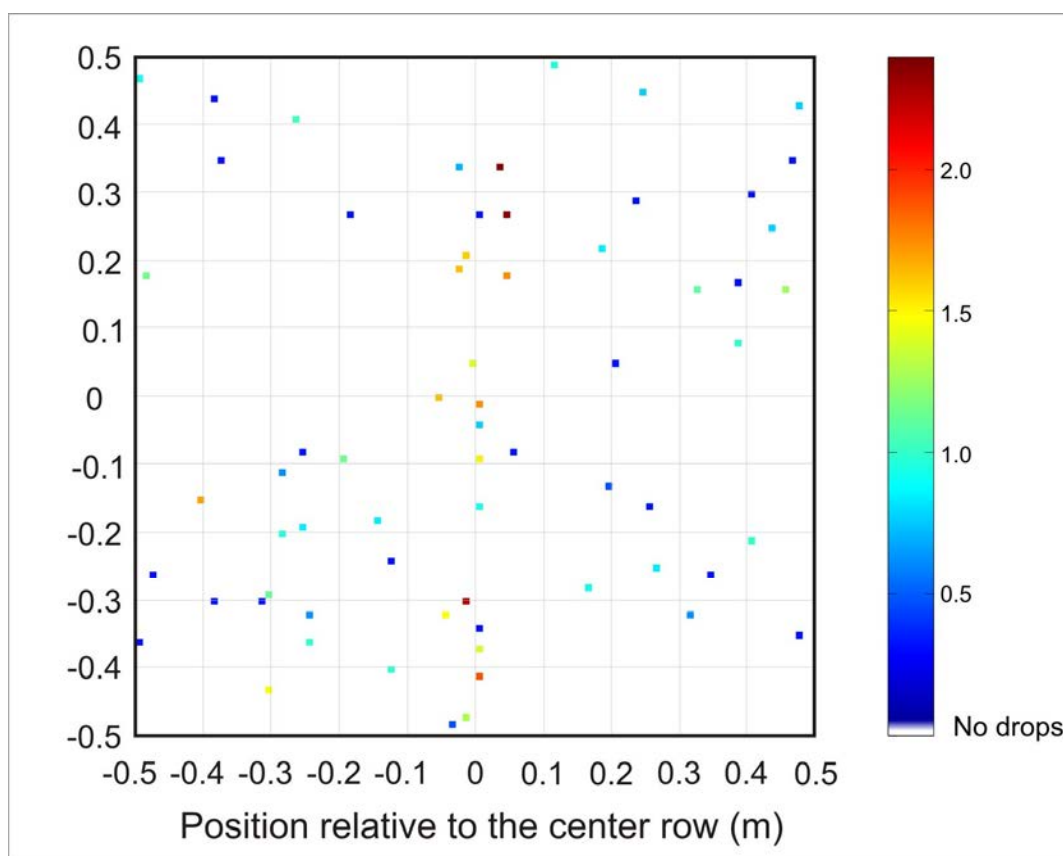
Figure VI-14. Two dimensional map of the location of throughfall drops with diameters larger than 6 mm. Colors represent the logarithm of the counts of drops for locations showing at least one drop.

Note that the pixels with the highest counts of large drops are located close to center of the plot, which corresponds to the area around the stems of the plants. Figure VI-15 shows how the fraction of the total number of large drops varies with the distance

from the center of the row. This plot indicates that most of the large drops predicted by the model for the storm of the 19 August 2009 are located within 50 mm of the center of the row. These locations are difficult to access with the disdrometer, which sensing area extended from approximately 82 mm to 243 mm measured from the center of the row. This implies that even if large drops are formed in such areas, our disdrometer cannot sample them. For this reason, the disagreement between the data and the simulations does not disqualify the model's performance.
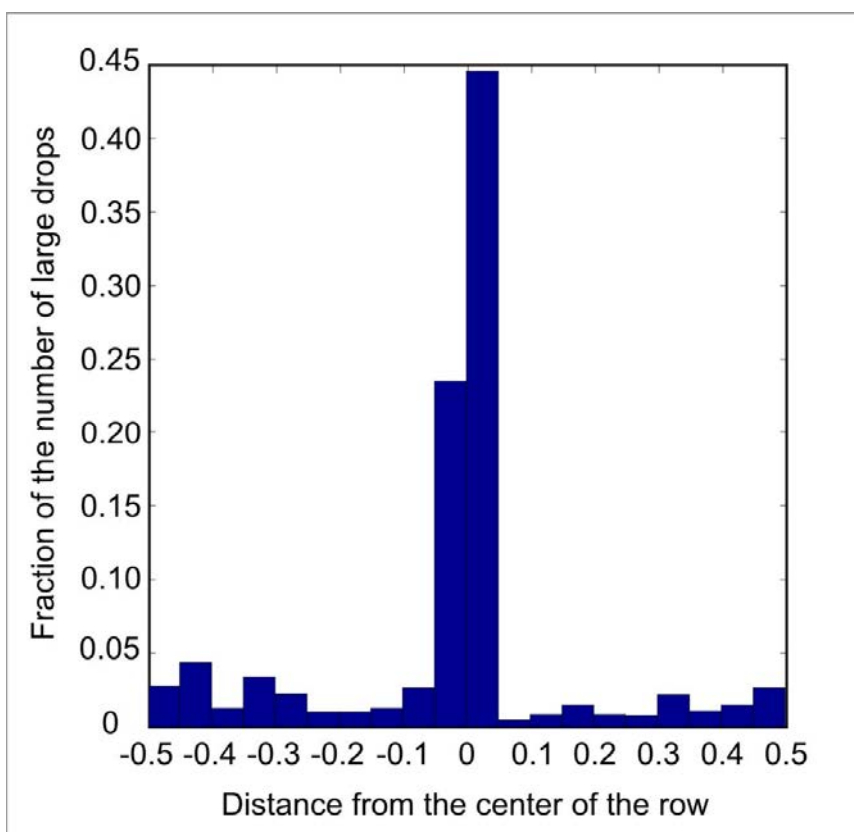
Figure VI-15. Distribution of the location of large throughfall drops with respect to the distance from the center of the row.

We simulated a total of 10 storms occurring towards the end of July 2009 (21 and 24) and throughout August 2009 (3, 7, 8, 9, 13, 16, 17, and 19). During these storms,

excluding the event from 21 July when the throughfall gauges were clogged, we measured a total of 214.3 mm of rainfall. Throughfall accounted for 60.0 mm, or 28% of the total rainfall and stemflow accounted for 65.7 mm, or 31% of the total precipitation.

Table VI-4 shows the experimental results per event, and Table VI-5 shows the simulation results for the same storms. Similarly to what we presented for the 19 August 2009 event, the simulation predicted higher percentages of throughfall (54%) and stemflow (44%).
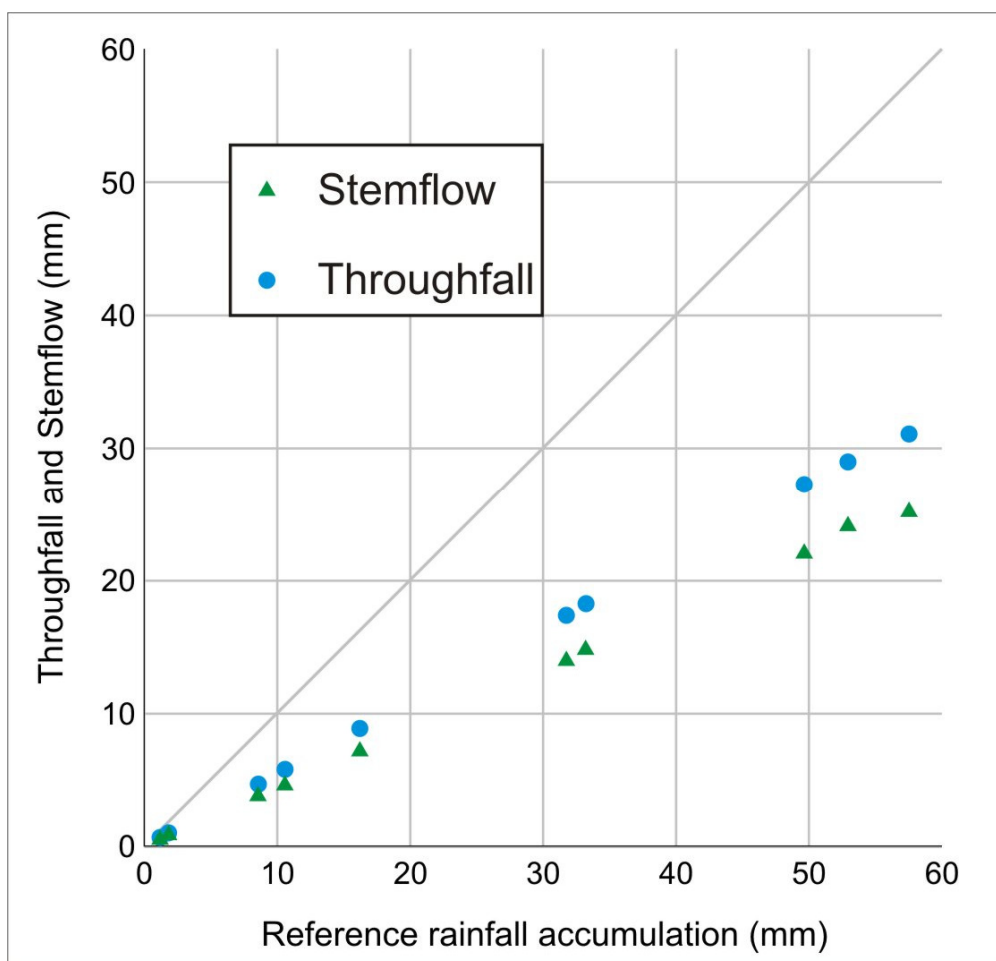
Figure VI-16. Simulated partitioning of rainfall in throughfall and stemflow for all the simulated storms. This set includes the storms of 21 and 24 July and 3, 7, 8, 9, 13, 16, 17, and 19 August 2009.

Table VI-4. Experimental results for the partitioning of rainfall by the canopy for the 10 studied storms.

	July					August				
	21	24	3	7	8	9	13	16	17	19
Rainfall	44.7	31.2	1.3	46.0	1.0	25.7	14.0	30.0	9.1	11.4
Throughfall 1	-	9.7	0.3	13.6	0.4	8.6	9.8	13.0	4.2	4.7
Throughfall 2	-	7.4	0.2	13.0	0.3	7.5	8.6	12.8	2.1	3.8
Stemflow 1	27.2	11.6	0.4	21.2	0.3	6.5	4.3	8.0	2.6	3.1
Stemflow 2	20.5	17.2	-	22.8	0.3	11.2	5.3	10.3	4.1	2.3
Storage	-	8.3	0.8	10.6	0.4	8.8	0.0	7.9	0.9	4.5

Note: All units in mm.

Table VI-5. Simulation results for the partitioning of rainfall by the canopy for the 10 studied storms.

| | July | | August | | | | | | | |
	21	24	3	7	8	9	13	16	17	19
Rainfall	53.0	57.5	1.8	49.7	1.2	40.3	22.6	33.2	10.6	16.2
Stemflow	24.1	25.1	0.8	22.0	0.5	17.7	9.7	14.7	4.6	7.1
Throughfall	28.9	31.1	1.0	27.2	0.6	22.0	12.2	18.2	5.8	8.8
Storage	0.2	0.5	0.0	0.2	0.0	0.2	0.2	0.1	0.1	0.2

Note: All units in mm.

Figure VI-17 shows the throughfall spatial distribution for the pooled storms. This figure displays a similar spatial distribution as the storm of 19 August 2009, which is shown in Figure VI-11. Dripping points are located around the stems, on the tip of the leaves, and on the periphery of open areas in the canopy. The distribution of throughfall with respect to the distance from the center of the row for the pooled data is identical to what Figure VI-12 shows for the single storm, indicating that the rainfall of the 19 August 2009 was enough to saturate the canopy when it comes to throughfall generation.
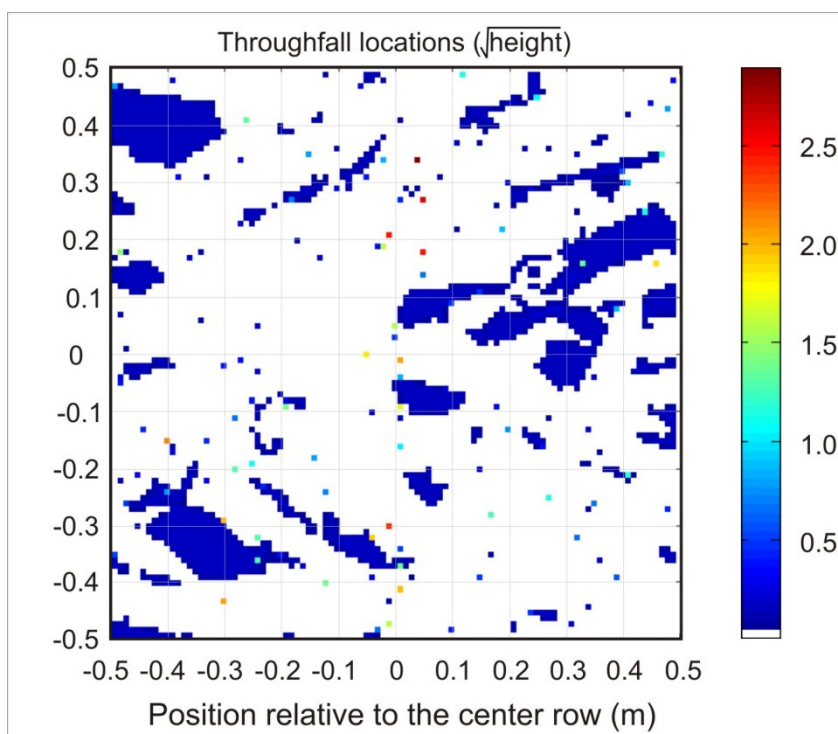
Figure VI-17. Two-dimensional throughfall map. Pixels are color coded according to the square root of the height of throughfall at their location.

The variation of the stemflow in the center row for all pooled storms (Figure VI-18) is also very similar to what we observed with the single storm (Figure VI-13). When it comes to the elements of the partitioning of rainfall by the canopy, the most

noticeable difference is the plant water storage. For all but three storms, the canopy

storage fluctuated between 0.12 mm and 0.19 mm; however, for one of the events (24

July), as much as 0.5 mm of rain remained on the leaves, and for the other two (3 and 8

August) the foliage retained as little as 0.03 mm. While the two low storage values are

likely to signify that the canopy wasn't saturated, we do not have a clear explanation for

the high storage observed on 24 July.
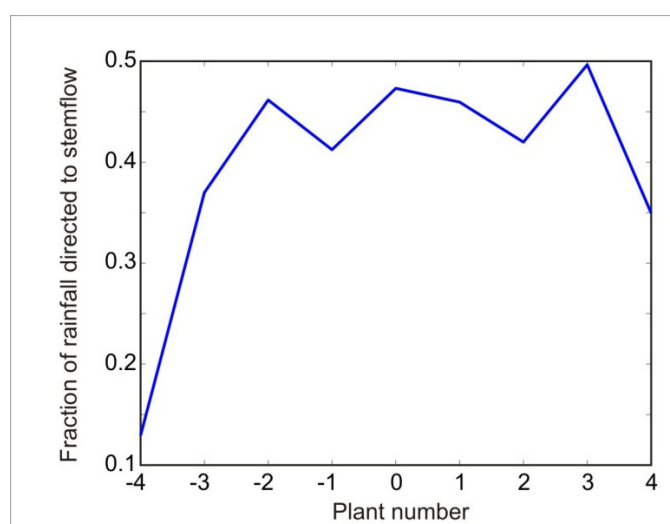
Figure VI-18. Distribution of the fraction of rainfall transformed to stemflow for each
plant in the center row. The first and last plants had considerable area lying
outside of the simulation area, which explains the lower fractions. Plants
numbered in reference to the central plant of the central row.

We initially thought that the large drops observed during the 24 July event caused

the higher capacity. However, looking back at Figure IV-3, on page 31, we see that the

vast majority of the drops with diameters between 1 mm and 6 mm have enough energy

to adhere to the leaf. In turn, once attached, larger drops require more energy to be

mobilized. More stagnant drops with larger diameters translate into more rainfall stored

on the canopy. However, when looking at the median volume diameter as an indicator of

the presence of a higher number of larger drops and a possible connection to the simulated storage, we did not find a clear pattern.

Table VI-6 shows the median volume diameter, simulated storage and measured rainfall for the simulated storms. We could not find a clear relationship between canopy storage and rainfall accumulation other than an indication that saturation occurs for accumulations between 2 mm and 9 mm.

Table VI-6. Median volume diameter (D_{50}), plant water storage (S) and total rainfall (R) for the simulated storms.

	July 2009		August 2009							
	21	24	3	7	8	9	13	16	17	19
R	52.95	57.54	1.83	49.65	1.17	8.57	31.75	33.24	10.58	16.21
S	0.18	0.53	0.03	0.15	0.03	0.12	0.13	0.12	0.14	0.19
D_{50}	1.50	3.50	2.00	2.50	1.75	3.00	3.00	2.50	2.50	2.50

Note: All units in mm.

Figure VI-19 compares the simulated and observed number of throughfall drops in each diameter class for the pooled storms. The agreement between observations and simulations is best between 0.250 mm and 3 mm. Unlike the observations from the event of 19 August 2009, the number of measured throughfall drops with diameters between 4 mm and 4.5 mm did not exceed the corresponding number in the rainfall above the canopy; however, the model successfully predicted the increased ratio for these two diameter classes.

Again, the most pronounced disagreement between the predicted and observed number of drops transpired for drops with diameters in excess of 5 mm. Figure VI-20 shows the location of drops with diameters larger than 6 mm. After the pooling of all

storms, these drops were present in the rainfall in larger numbers. A fraction of them found openings in the canopy and are now visible in the map. As with the data we presented for the 19 August storm, the locations with the higher counts of drops with diameters larger than 6 mm are still concentrated in the vicinities of the central row. Figure VI-21 shows how the counts of large drops vary with the distance from (left panel) and along the row (right panel).
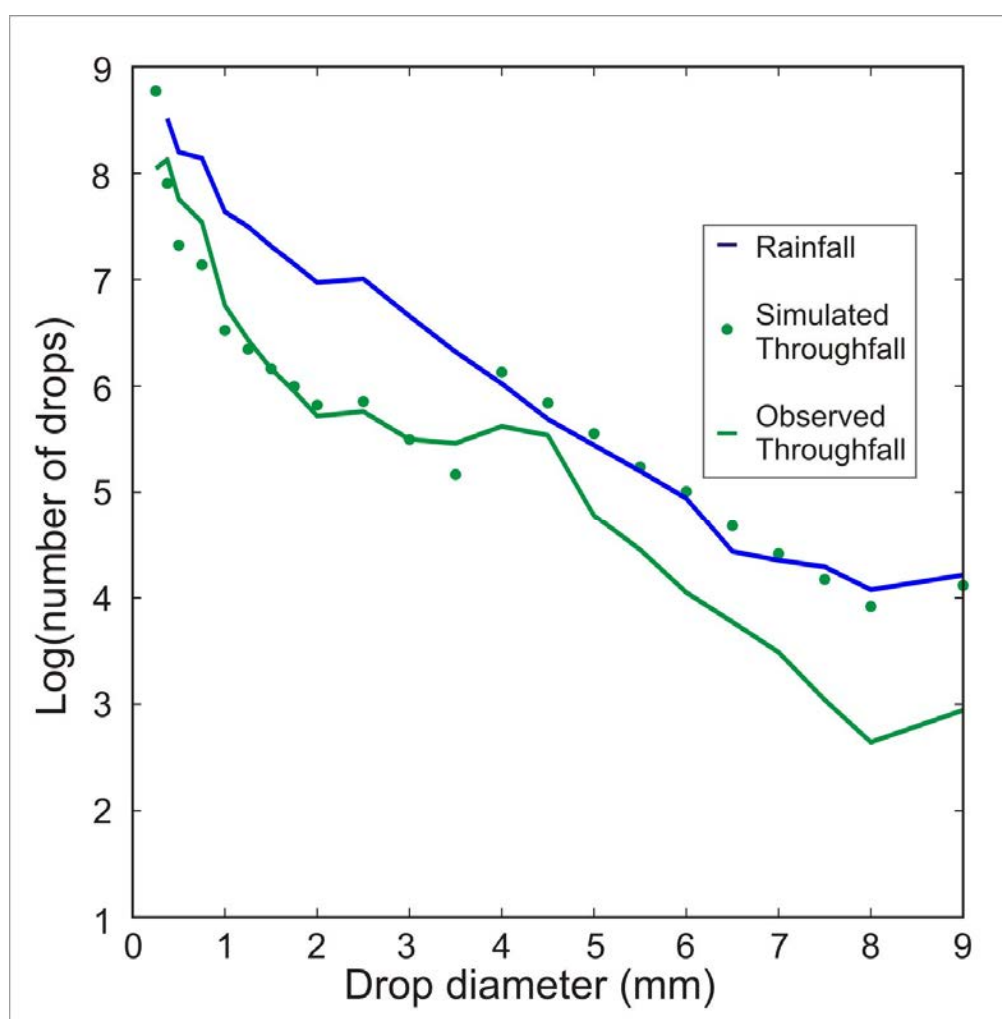
Figure VI-19. Counts of drops of each diameter class featured in observed and simulated throughfall for all the simulated storms.
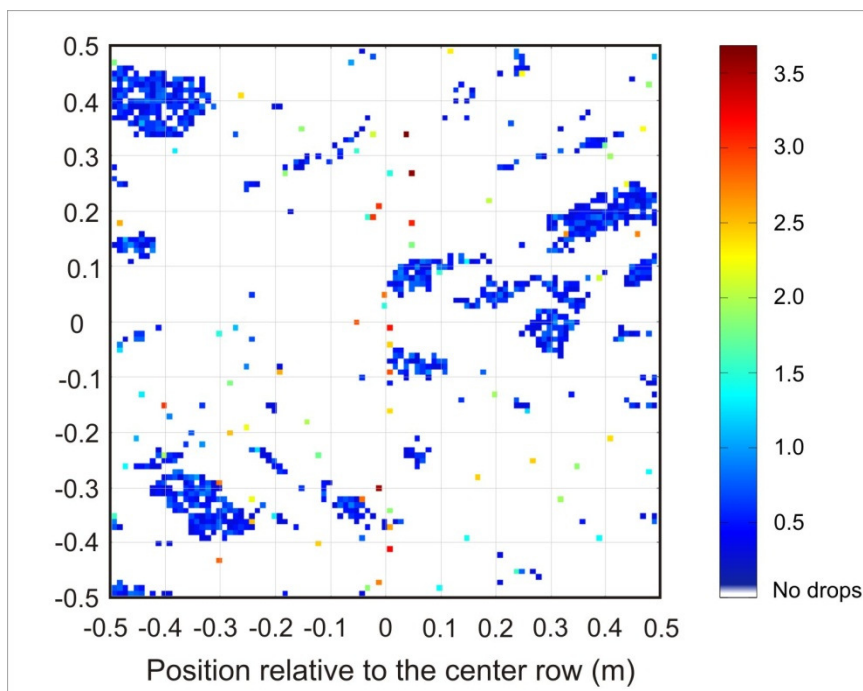
Figure VI-20. Two dimensional map of the location of throughfall drops with diameters larger than 6 mm. Colors represent the logarithm of the counts of drops for locations showing at least one drop. Results represent the accumulation of all simulated storms.
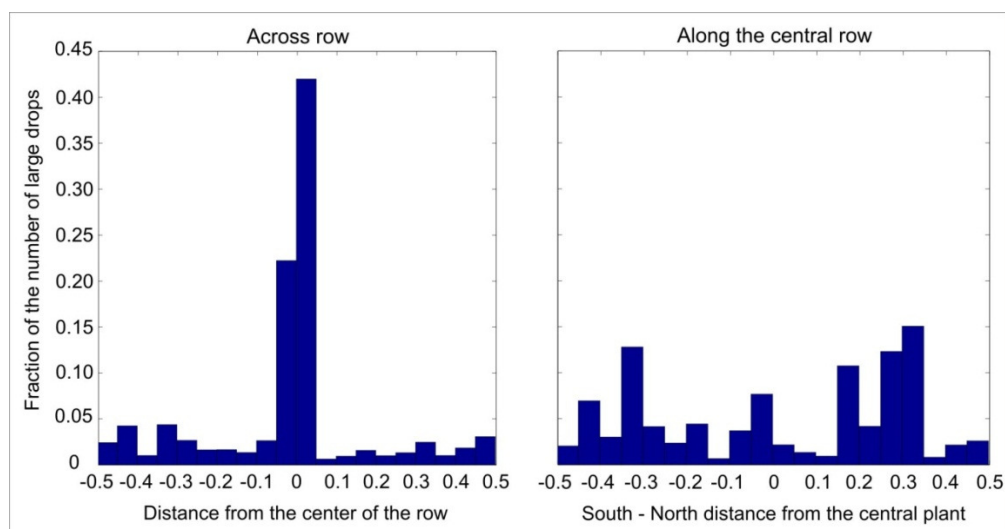
Figure VI-21. Distribution of the location of large throughfall drops with respect to the distance from the center of the row (left panel) and along the central row (right panel). Results represent the accumulation of all simulated storms.

Since we knew the distance from the locations where drops detached from the foliage to the surface of the ground, we could estimate the velocity of the indirect throughfall drops. Assuming that the drops from the direct throughfall didn't change their velocity, we computed the combined throughfall drop size and velocity distribution at ground level. Figure VI-22 shows the resulting diameter-velocity distributions for the simulated (left) and observed (right) datasets. We kept the color scheme for both pictures the same to allow for better comparison.
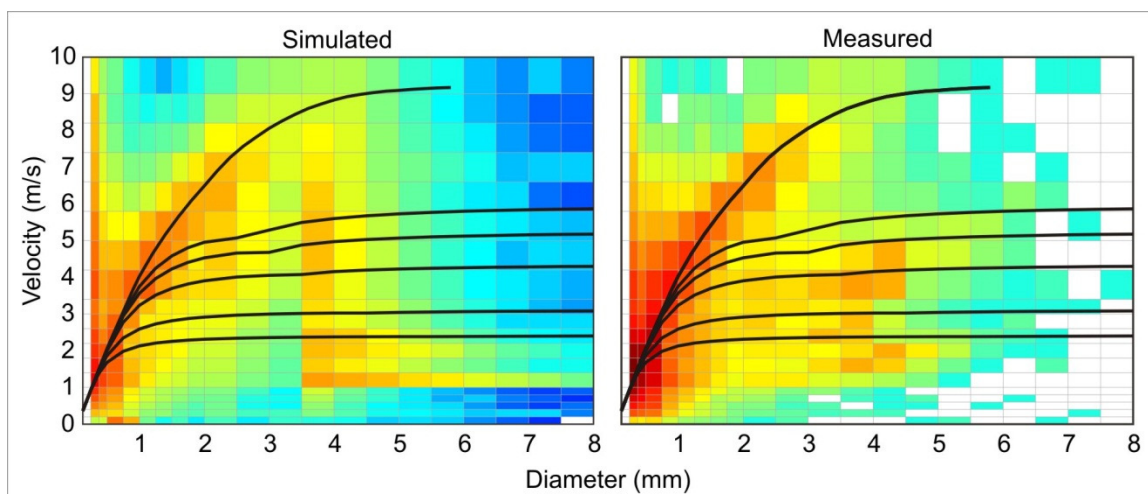
Figure VI-22. Diameter-velocity distributions of throughfall drops. The left panel shows the simulated distribution, and the right panel shows the corresponding measured distribution. The solid curves represent the velocities that drops are expected to develop after a fall of 0.3 m, 0.5 m 1.0 m, 1.5 m, and 2.0 m, respectively. The last curve shows the Gunn and Kinzer terminal fall velocities.

Both panels identify a group of drops with diameters between 3.5 mm and 4.5 mm that have velocities consistent with a fall from less than 0.3 m. This group extends for a wider range of diameters in the simulated dataset, since the disdrometer could not sample the areas around the stem where our model indicates that most of the large throughfall drops are located.

The model did not overestimate the number of large drops for all storms. For one event, the trend of better predicting the number of drops with diameters smaller than 3 mm while overestimating the occurrence of large drops was inverted. Figure VI-23 shows the size spectra of drops in the total rainfall and observed and simulated throughfall for the 13 August 2009 storm. The agreement between the simulated and observed number of throughfall drops for the range of diameters between 5.5 mm and 7 mm was considerably better than it was for the other storms.
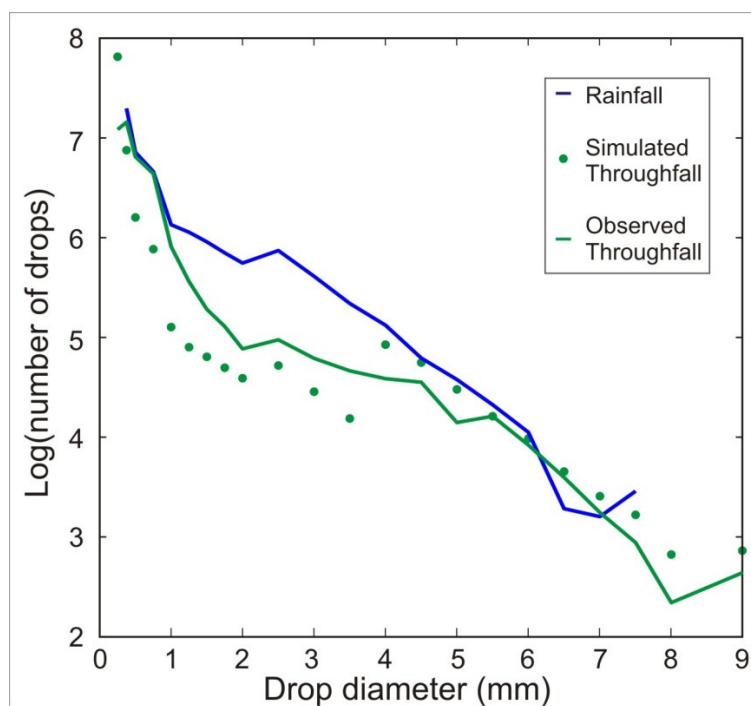
Figure VI-23. Comparison between the simulated and observed drop-size spectra for the 13 August 2009 storm.

While the disdrometer remained in the same place throughout the experimental campaign, the leaves, being flexible, could have shifted in response to external stimuli such as the wind. It is possible that leaf rearrangement could have changed the location where large drops were formed, directing more of them to the disdrometer sensing

volume. At this time, our canopy model is static and does not account for changes in leaf geometry or positioning. However, allowing changes in leaf azimuth could improve the quality of our estimations without adding considerable computational effort. Ideally, we would consider leaf flexibility and compute drop trajectories considering the surface's deformations.

<div align="center">Assessment of the impact of instrumental uncertainty on</div>

<div align="center">the simulation results</div>

Instruments are affected by uncertainty, which in turn impacts simulation results. In order to assess the potential impact of measurement error on the quality of the predictions, we used data simultaneously collected by four disdrometers that were collocated side by side at the Iowa City airport. We selected the storm of 08 August 2008 and simulated the rainfall partitioning, considering each disdrometer as a source of rainfall measurements. This data is part of the set used in Appendix A to evaluate the optical disdrometer's instrumental uncertainty.

Table VI-7 shows the resulting stemflow, throughfall, and canopy storage for the simulations that we ran using the rainfall data obtained with the four disdrometers. The values differ in absolute numbers; however, as illustrated by Table VI-8, the stemflow and throughfall fractions remained quite constant despite the 13% variation between the highest and the lowest rainfall accumulations. This indicates that the partitioning of rainfall into throughfall and stemflow is more sensitive to the canopy geometry than to rainfall characteristics, provided that you have enough rainfall accumulation to saturate the canopy.

Figure VI-24 compares the throughfall drop-size spectra from the four simulations. When we plot the ratio between throughfall and rainfall drop counts for each diameter class (left plot), we see a considerable divergence between the simulations run with data from different disdrometers. However, when we look at the logarithm of

the throughfall drop counts, the curves are much closer to each other, with the exception of the few last diameter classes. The agreement is especially good when we consider the divergence of the disdrometer drop-size spectra measured by the four instruments that is shown in Figure VI-25.

This indicates that the simulated throughfall drop-size spectrum, in absolute numbers, tends to less sensitive to differences in the rainfall drop-size distribution. Figure VI-26 shows the throughfall diameter-velocity spectra, which is also remarkably similar despite differences in the disdrometer data.

Table VI-7. Simulated partitioning of rainfall during the 8 August 2008 storm.

	Disdrometer 1	Disdrometer 2	Disdrometer3	Disdrometer 4
Rainfall	20.87	18.18	19.21	19.80
Stemflow	9.30	7.98	8.44	8.68
Throughfall	11.59	9.92	10.49	10.84
Storage	0.12	0.12	0.12	0.10

Note: All units in mm.

Table VI-8. Simulated partitioning of the 8 August 2008's rainfall.

	Disdrometer 1	Disdrometer 2	Disdrometer3	Disdrometer 4
Rainfall	1.00	1.00	1.00	1.00
Stemflow	0.45	0.44	0.44	0.44
Throughfall	0.56	0.55	0.55	0.55
Storage	0.01	0.01	0.01	0.01

Note: All terms are expressed as a fraction of the total measured rainfall.
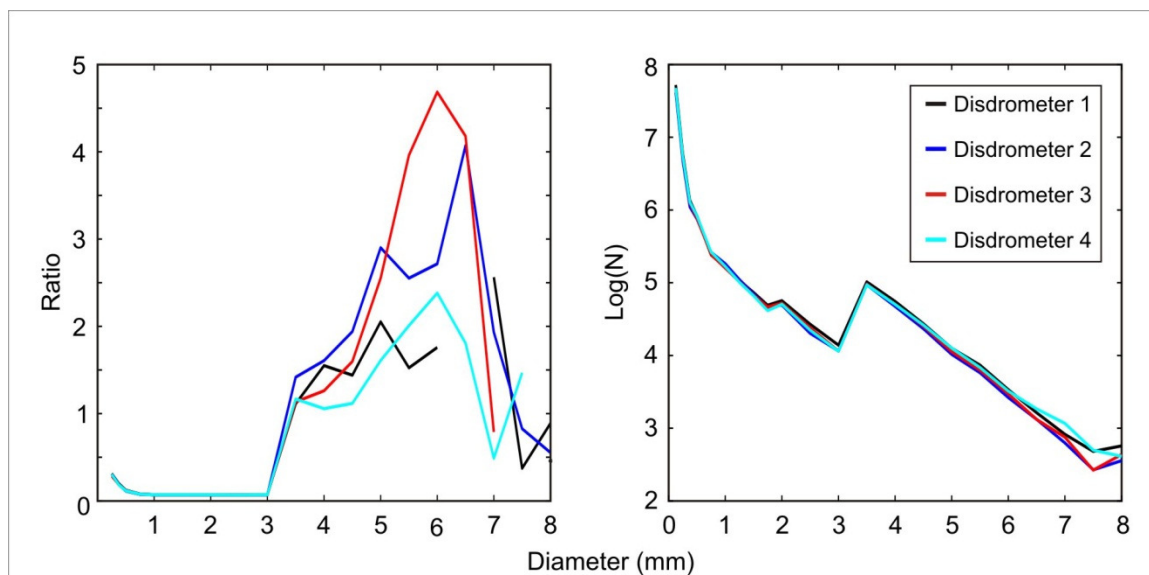
Figure VI-24. The left panel shows the ratio between throughfall and rainfall drop counts for the four disdrometers. The right panel shows the throughfall drop-size spectra simulated using data simultaneously collected by four different disdrometers.
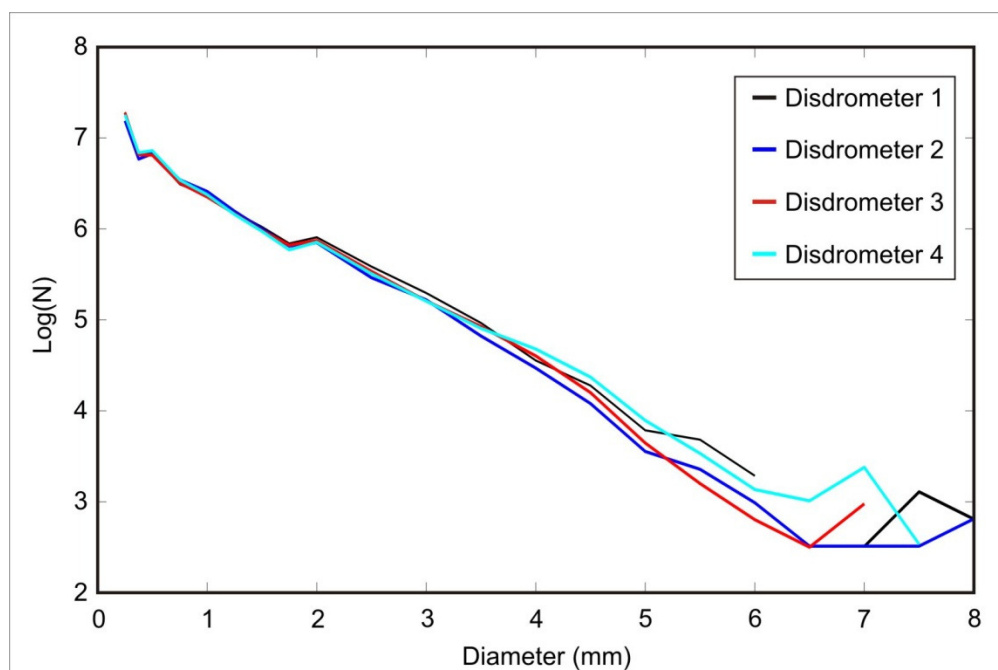
Figure VI-25. Comparison of the measured rainfall drop-size spectra measured simultaneously by four different disdrometers.
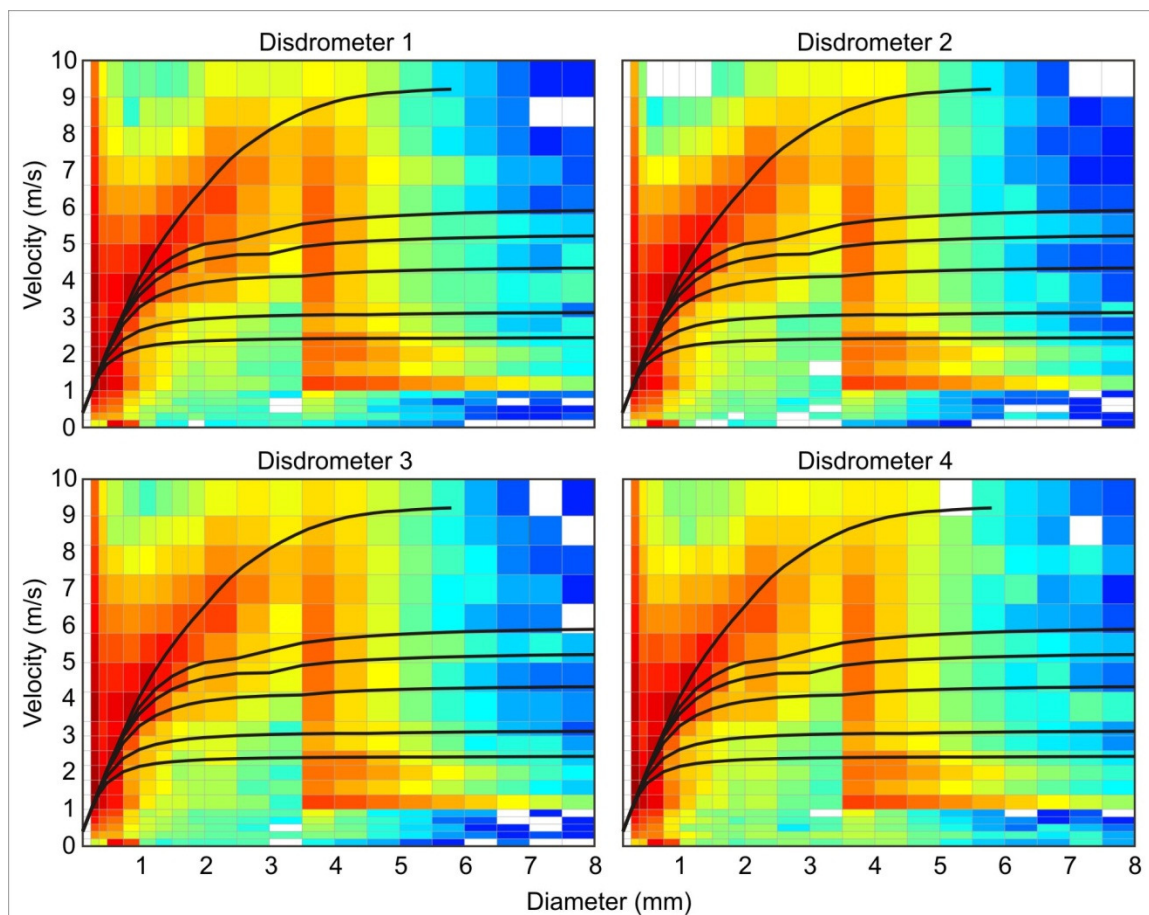
Figure VI-26. Comparison of the simulated throughfall diameter-velocity distributions using data simultaneously collected by four different disdrometers.

Future work

The movement physics used in this model can be further refined. In the model's current state of development, once a drop is moving, it will not stop. We would like to improve the model by adding stopping mechanisms to the moving drops. This could be achieved by comparing the energy that is transformed from potential to kinetic energy and the energy that is dissipated by friction (modeled here as adhesion hysteresis). Similarly, we would like to determine whether merged drops would move after they coalesce.

The leaf attachment points can also hold water. We would like to evaluate their storage potential and incorporate them as reservoirs in a future version of the model. That, along with allowing for the formation of water films on the leaves, would improve our estimation of canopy storage.

Making the canopy flexible is another improvement that we would like to implement. As we mentioned, this can be accomplished in two levels: the first would allow for changes in the azimuth of the leaves without changing the leaf's geometry; the second and more profound modification would incorporate changes in the leaves' geometries. While allowing for the rearrangement of leaves would not be expensive, changing the leaves' geometries would require the recalculation of coverage matrices and drop trajectories. This extra computational load could potentially be met by the use of parallel computing.

Since our model estimates the throughfall drop-size, velocity spectra, and dripping locations, we could use it to examine the impact of row and in-row distances on the occurrence and spatial distribution of areas with high kinetic energy flux under the canopy. Such a study would provide insight into the impact of different agricultural praxis on erosion potential, potentially leading to improvements in current soil loss models.

As is, our model is a good tool for assessing the impact of different physical phenomena on the characteristics of throughfall and the partitioning of rainfall by the canopy. However, the application of our detailed simulations to scales that are relevant to hydrological studies is unfeasible. Moving from explicit modeling of raindrop-vegetation interactions to a statistical framework could offer the improvement in performance required for the task. In the future, we would like to use the knowledge gained through our simulations to create a simplified multi-layer interception model using the framework of the two-layer stochastic model described by Calder (1996).

An alternative to abandoning the explicit drop movement framework is to simulate the interception of rainfall by various small canopies, each reproducing a set of canopy characteristics. These characteristics could be: different plant spacing, observed gap fraction, leaf zenith distribution and others. The full sized canopy could then be formed by grouping the small subsets. By considering each small canopy independent to the others, each simulation can run in one processor, in a multi-processor computer, allowing the simultaneous computation of the partitioning of rainfall by each small canopy.

Conclusions

We presented a rainfall interception model that explicitly simulates the movement of raindrops through a three-dimensional digital representation of a maize canopy. The model can predict the throughfall, stemflow, and canopy storage totals as well as the throughfall size and velocity spectra and spatial distribution beneath the foliage.

Our model estimated that, on average, 55% of rainfall reaches the ground as throughfall, while the data acquisition campaign pointed towards 35%. This indicates that our model overestimates throughfall generation. However, when we look at the spatial distribution of the throughfall, we see that a considerable fraction falls too close to the stems of the plants to be detected. This suggests that the disagreement between measured and simulated throughfall totals could be due to loss of water during the experiments.

Stemflow totals also appear to be overestimated by our model. Our simulations estimated that 44% of rainfall is directed towards the stem of the plants, with some variation between stems, while the observed value was around 39%. We believe that the inability to account for water retention around the leaf collar and the predicted variability of stemflow from plant to plant cause this divergence. Water stored at each connection

would affect only the stemflow and lead to the underestimation of canopy storage and overestimation of stemflow fraction.

Our model identified dripping locations. Such areas are receiving much more water than otherwise uncovered areas would. The repeated localized dripping could lead to increased mobilization of soil particles that could be easily carried by runoff.

Contrasting measured and simulated throughfall drop-size spectra initially indicated that we were overestimating the number of drops with diameters exceeding 6 mm. However, our model indicates that these drops mostly fall close to the stems in areas that are unreachable by our disdrometers. Consequently, at this point we cannot refute the existence of drops of such diameter in larger than detected numbers.

Finally, we used simultaneously measured data from four disdrometers to assess the impact of instrumental uncertainty on the model's predictions. Even though we detected differences in the absolute vales of throughfall and stemflow accumulations, the throughfall and stemflow fractions estimated from the different instruments were quite similar. Furthermore, the throughfall drop-size and velocity spectra estimated using the different data sources were quite similar, indicating reasonable stability of our model.

CHAPTER VII.

SUMMARY

Introduction

This chapter reviews the objectives outlined in CHAPTER II and discuss to what degree we met our original goals. Furthermore, we contrast and summarize the experimental and computational results, highlight the areas where our model results agreed with observations, and indicate limitations on the experimental and computational methods.

Revisiting the original objective

The overall objective of this thesis is to understand rainfall interception processes. As stated in CHAPTER II, our ultimate goal is to predict the stemflow, throughfall and plant storage totals and characteristics, for a given storm and canopy structure. While the uncertainties inherent to our experimental methods prevented us from confidently estimate the amount of rainfall stored on the plants solely based on the observations presented in CHAPTER III, the additional insight provided by the computer simulations (CHAPTER VI) allowed the quantification of limitations in our experimental setup. On the other hand, our model also contains uncertainties and limitations. Contrasting simulation results with observations allowed us to identify improvements that can lead to a robust tool to estimate the location and quantity of rain water stored on a canopy.

Despite the listed limitations, we successfully created a model capable of estimating stemflow and throughfall totals and spatial distribution, given a three-dimensional representation of a canopy and rainfall information. Moreover, we predict throughfall characteristics in the most fundamental level, *i.e.* the distribution of drop sizes and velocities. This unique capability allows the development of a variety of studies, *e.g.* the mechanistic modeling of erosion beneath maize canopies, the study of small scale soil

moisture heterogeneity due to the interaction of rainfall and crop canopies, and the assessment of the effects of different row configurations on the rainfall partitioning.

Conciliating experimental and computational results

By pooling the rainfall, stemflow and throughfall measurements for the 10 studied storms in CHAPTER VI, we estimate that the throughfall and the stemflow accounts for 35% and 39% of the total rainfall, respectively, whereas our model points to higher values of 55% and 44% for the same quantities. An initial comparison of the simulated and observed throughfall and stemflow fractions indicates a considerable overestimation of these two quantities by our model. However, a deeper analysis of the spatial distribution of stemflow and throughfall predicted by our model shows that the positioning of our instruments could explain the disagreement to a certain extent.

Figure VI-17 (page 128) shows the throughfall spatial distribution. By revisiting this figure, we see a considerable number of dripping points located around the stems of the central row, *i.e.* the center of the figure. Because the edges of the throughfall collector were touching the stems of the plants, which were 20 mm in diameter, all dripping points located 10 mm to the right and to the left of the stems did not reach the throughfall collector. Figure VI-12 (page 121) shows how the fraction of throughfall changes with the distance from the stems, which allows us to estimate that approximately 13% of the throughfall was lost. By adding the estimated lost throughfall to what we measured, the throughfall fraction reaches a value of 0.45, improving the agreement between simulations and experiments.

Our simulations also showed that the stemflow varies in adjacent plants. Figure VI-18 in page 129, shows the predicted stemflow on 9 plants in the center row. Even if we neglect the low stemflow fractions in the first and last plants, since a considerable part of their leaf areas were outside of the computational domain, we still see variation among plants. This variation indicates that depending on the positioning of the stemflow

collectors, we can measure different quantities. However, we believe that the cause of the stemflow overestimation by our model is due to not considering rainfall storage on the leaf collar. Intercepted rain water stored on the leaf collar would cause little change to throughfall totals, and should affect mostly the stemflow totals.

Comparison of the simulated and observed throughfall at the drop-size distribution level allowed a better explanation of the results presented in CHAPTER IV. With the knowledge gained through the computational study, we could confirm that indirect throughfall is the origin of the larger number of drops with diameter between 4 mm and 4.5 mm. The model also showed that presented drop attachment threshold cannot fully explain the elevated number of throughfall drops with diameter smaller than 1 mm and drop breakup through splashing is responsible for most of the observed increase.

Figure VI-19 (page 131) shows that the agreement between simulated and observed throughfall counts is not the same for all drop diameters, and is better for smaller drops. As with the throughfall height, lack of opportunity to sample dripping locations could explain the apparent overestimation of large drops by our model. Figure VI-21 (page 132) shows that our model predicted that more than 60% of drops with diameter in excess of 6 mm fell too close to the stems to be sampled.

<u>Conclusion</u>

The interpretation of our experimental results is not straightforward. Measurement uncertainties and limitations in our instrumentation affect the quality of our data. Therefore, calibrating our simulation results to force a better agreement can lead to an unrealistic rainfall interception model. The insight gained through the analysis of the simulation results allowed us to identify two critical improvements: one to the instrumentation, consisting of modifying the throughfall collectors to sample the area

between stems, and a second to our rainfall interception model, incorporating storage on each leaf collar.

APPENDIX

ASSESSMENT OF THE THIES OPTICAL DISDROMETER

PERFORMANCE

Introduction

The goals of the present study are to quantify the uncertainty of the drop diameter measurements obtained with Thies optical disdrometers and to determine the degree to which it explains the uncertainty of the instrument's rainfall rate and accumulation estimates. This uncertainty is represented here by the differences between the disdrometers' estimates, the disdrometers' and tipping bucket rain gauges' measurements, and the disdrometers' and Vaisala WXT510 compact weather station's measurements.

The following section discusses the experimental setup, including a description of the instruments and calibration device that we designed, followed by a description of the two computer simulations we developed. The first simulation assesses the influence of beam pattern in determining drop diameter, whereas the second simulation propagates the uncertainty of the diameter measurement to the rainfall accumulation estimates. We then discuss the results, beginning with an analysis of the calibration data. Subsequently, we present a method to filter improbable errors in the disdrometer measurements, followed by a comparison of disdrometer, WXT510, and tipping bucket rainfall accumulation results. We then examine the propagation of the uncertainty in the diameter measurements of the rainfall accumulation estimates and end with a summary of our findings and the conclusions.

Background

Improving our understanding of the spatial and temporal variability of rainfall characteristics requires a dense network of instruments that can provide drop-size distribution (DSD) measurements. The instruments must be: robust and reliable enough to withstand variable weather conditions throughout the year, easy to calibrate or

calibration-free to minimize operation costs, inexpensive, and able to measure drop sizes accurately. Optical disdrometers are relatively new instruments that have the potential to meet these requirements. Although the performance of impact disdrometers is well documented (Joss and Waldvogel, 1977; Kinnell, 1976; Licznar et al., 2008; Tokay et al., 2005; Tokay et al., 2001; Tokay et al., 2003), the error characteristics of their optical counterpart are not yet fully understood.

In an early attempt to ascertain the error characteristics of optical disdrometers, Donnadieu (1980) evaluated the performance of a photoeletric spectropluviometer in conjunction with a Joss-Waldvoguel (JW) impact disdrometer. The author compared the velocity readings with the Gunn and Kinzer velocity relation (Gunn and Kinzer, 1949) as well as with the drop-size distribution, rainfall rate, and radar reflectivity as measured by the two disdrometers and found discrepancies between the drop velocity measurements and the Gunn and Kinzer relation. They subsequently proposed corrections to the JW data to account for these deviations. The proposed corrections for the JW disdrometer in terms of the rainfall rate and liquid water content represent a decrease of 12% and 17%, respectively. However, the limitations of the optical technology were not discussed in depth.

Many other optical disdrometers can be found in the literature, and each attempts to either decrease the instrument's uncertainty by lessening its susceptibility to a perceived source of uncertainty or to increase its range of measurable drops. For example, Hauser et al. (1984) describe the optical spectropluviometer (OSP), which works similarly to the Thies optical disdrometer employed in the current study. The OSP calculates the diameter of rain drops by determining the decrease of a photo receptor's output caused by partial shading of an infra-red laser beam. Assuming that drops can be accurately measured when their signature exceeds twice the root mean square noise intensity of the system, the authors estimate that their instrument can measure drops as small as 0.14mm in diameter. However, additional unsuppressed 50 Hz rumble noise in

the power lines at the test location prohibited measurement of drops smaller than 0.3 mm in diameter.

The prismatic light beam commonly employed in optical disdrometers makes them susceptible to errors derived from non-vertical drop trajectories. Illingworth and Stevens (1987) as well as Grossklaus et al. (1998) designed disdrometers with cylindrical and annular beams, respectively. Grossklaus et al. (1998) supported the claim that the proposed geometry is less affected by non-vertical drop trajectories. Due to these instruments' larger sampling volume, the detection of simultaneous drops is an issue. The instrument described by Grossklaus et al. (1998) incorporates a correction method, but the authors do not provide details.

Even in optical disdrometers with smaller sampling volumes, the detection of simultaneous drops is a problem, especially during intense precipitation. Raasch and Umhauer (1984) discussed the problem and proposed a correction that could reduce this error in the measurement of drop-size distribution. The authors demonstrated the effect of the original size distribution's shift towards larger sizes for a given particle concentration. By assuming that particles are uniformly distributed in the air, they used the Poisson distribution to calculate the probability of encountering a particle inside the volume. The authors proposed an iterative method to retrieve the original particle size distribution and, therefore, to correct the measurements by further assuming that the shape of a single scattered light signal approaches a rectangular impulse and that this signal always exceeds the minimum measurable threshold, neglecting dead time, and assuming that signals from simultaneous drops are additive.

Loffler-Mang and Joss (2000) used computer simulations to determine the susceptibility of optical disdrometers to detect simultaneous drops and found the probability of simultaneous drops occurring to be as high as 10% during intense rainfall events. Due to this perceived potential error, the authors incorporated into their prototype device the correction proposed by Raasch and Umhauer (1984) that resembles the later

Thies optical disdrometer. Although their prototype increased the observable range of raindrop sizes, it introduced the need for calibration in order to determine the behavior of the electronic components and the optical systems.

The sensitivity of optical disdrometers to wind-induced errors motivated the use of computational fluid dynamics to study the modification of drops' trajectories by the air movement. Nespor et al. (2000) simulated the airflow around an unmodified two-dimensional video disdrometer (2DVD) in order to assess the potential of wind as a source of error in the measurement of rainfall and drop-size distribution. They tested nine different wind velocities, varying from 1 to 12 m s^{-1}, and six different angles, ranging from 0° to 45°. When the authors observed the main flow around the instrument and recirculation inside the instrument measuring chamber, they detected a complex flow pattern. The effects of the wind flow patterns on the measurement of drop-size distribution were not quantified at that time.

Concerned with the effects of the instrument's aerodynamics, Habib and Krajewski (2001) simulated airflow around the instrument to evaluate the possible impacts of the change in the raindrops' movement. The results of the simulation showed that wind effect is a potential source of error in the measurement of drop-size distribution by the 2DVD. The authors concluded that computational fluid dynamics (CFD) could be used to assess different instrumental geometries in the future design of meteorological instruments. More recently, Constantinescu et al. (2007) employed CFD to study the wind's effects on tipping bucket rain gauges and demonstrated that these instruments are also vulnerable to wind-induced errors.

Ciach (2003) used a network of 15 identical collocated gauges to analyze the error characteristics of tipping bucket rain gauges and found that random errors are dependent upon the rainfall intensity and the timescale. He used nonparametric regression to estimate and model these dependencies. The author defined the local error of single rain gauges as a relative deviation from the average of the 15 gauges at the desired time scale,

and he ultimately found that the tipping bucket's standard error decreases with increasing rain rate and integration interval. Other studies that evaluated the spatial and/or temporal sampling uncertainties of rain gauges include Nystuen (1998) and Villarini et al. (2008).

Miriovsky (2003) examined the spatial variability of the DSD on a radar sub grid scale, *i.e.* about 1 km^2. They used different disdrometers that were deployed inside an area of 1 km^2 but ultimately concluded that they could not separate the natural variability from the instrumental variability. This study motivated a later effort by Krajewski et al. (2006), who installed a 2DVD, a Dual Beam Spectropluviometer (DBS), and a Parsivel disdrometer at the Iowa City, Iowa municipal airport. By installing the instruments close together, they could neglect the natural variability, and the detected differences could be attributed to instrumental variability. The authors found significant discrepancies between the disdrometers as well as between the disdrometers and rain gauges, with higher differences occurring during heavy rainfall events.

To improve the measurement of solid precipitation, Barthazy et al. (2004) created an optical disdrometer called the Hydrometeor Velocity and Shape Detector (HVSD). It was designed to measure particles larger than 1mm, and it consists of a light source, a receiver, and a personal computer for data acquisition. Due to the trapezoidal shape of the light sheet, the position of the hydrometeor along the beam introduces error by interfering with the diameter estimate. The authors estimated the error in the measurement of the diameter of raindrops to be about +-60% for sub-millimeter particles and +-6% for particles larger than 1mm. Measurements were compared to Berry and Pranger's fall velocity calculations (Berry and Pranger, 1974) and showed slower mean velocities for drops smaller than 1mm, good agreement for drops between 1mm and 2.5mm, and higher velocities for larger drops. The comparison between the DSD measured by JW and the HVSD showed an underestimation of sub-millimeter drops by the HVSD.

Tokay et al. (2005) evaluated the error characteristics of the JW impact disdrometer. The instrumental setup varied from two to six JW disdrometers, and, for a limited time, a two dimensional video disdrometer and a tipping bucket rain gauge. During three months of six JW units working uninterruptedly, four JW units showed excellent agreement in rainfall, while the other two overestimated or underestimated the total accumulation by 15% and 11.5%, respectively. Rate-wise, the maximum difference between individual disdrometers and the average varied from 10% to 35% at the 1-minute level. The error magnitude did not appear to be correlated to rainfall intensity.

Lanzinger et al. (2006) compared three Thies Laser Precipitation Monitors (LPMs) with a pit gauge and found that the LPMs consistently measured higher rainfall amounts than the pit rain gauge, especially during higher intensities. At the end of the examined period, the three disdrometers presented average daily deviations from the pit gauge measurements of 5.3%, 15.0%, and 20.2%, respectively. The authors suggested that these consistent differences point to calibration problems. They also hypothesized that the association of higher errors with high intensity storms could be caused by the misinterpretation of multiple simultaneous drops as single large drops and indicated that the real reasons for the errors could be found through further analysis of the particle size spectra.

Varying sensitivity to specific drop sizes represents another source of discrepancy between instruments that employ diverse measurement techniques. For instance, Campos and Zawadzki (2000) compared the estimates of the radar reflectivity – rainfall rate relationship given by three types of disdrometers: (1) the impact based disdrometer (JW), (2) the optical disdrometer (optical spectro pluviometer, OSP), and (3) a radar based disdrometer called a precipitation occurrence sensor system (POSS). They found that after removing drops smaller than 0.7mm in diameter, the agreement of the drop-size distribution level was good. However, despite the good agreement of the DSD, there were significant differences between estimates of the parameters of Z-R relationships and

between parameters estimated from the same instrument with different techniques. The authors concluded that one should proceed with caution when comparing results obtained from different instruments or techniques.

Caracciolo et al. (2006) compare an X-band continuous wave disdrometer called Pludix with a 2DVD, a JW, and Tipping bucket rain gauges. The Pludix was designed to classify precipitation and measure drop-size distribution, instantaneous rainfall rate, and rainfall accumulation at a lower cost and requires lower maintenance than impact disdrometers. Pludix can detect larger drops, whereas JW can detect smaller ones. The analysis of the rainfall amounts showed that the Pludix often underestimates the light to moderate events, with respect to the tipping bucket rain gauge and the JW; however during high intensity storms, the trend is inverted, which is consistent with the difference in the range of measurable drops between the JW and the Pludix.

More recently, Brawn and Upton (2008) presented a method to estimate the parameters for gamma drop-size distribution that minimize the bias and imprecision caused by the inability to measure smaller drops with disdrometers. The authors briefly illustrate how sampling variability affects our perception of the drop-size distribution. They present a hypothetical case in which the drop-size distribution is constant over time and homogeneous in space. In this scenario, an observer would still believe that drop size varies with time and space due to the fact that disdrometer observations represent only a sample of the population of raindrops. The small-scale variations would then affect our perception of the real natural distribution. The authors used data obtained with the Joss-Waldvogel impact collected between August 2002 and June 2003 and also examined a more limited data set collected with a Thies LPM. The authors found that the optical disdrometer's capability to see a wider range of drop sizes improved the estimation of the gamma distribution parameters.

Cao et al. (2008) evaluated the use of two-dimensional video disdrometers associated with polarimetric radar to characterize rain microphysics. The authors

proposed an approach to quantify the uncertainty associated with limited sampling volume on the determination of parameters used to describe drop-size distributions. The truncated moment fit method described by Vivekanandan et al. (2004) was used to fit three gamma distribution parameters to the data retrieved by two 2DVDs.

The sampling error was described by the fractional standard deviation, which equals the error standard deviation divided by the time-average of all available data. The authors found that the fractional standard deviation (FSD) increased with the increasing moment order and that the correlation between different moment orders decreases with an increase in the distance between moments. According to Zhang et al. (2003), the FSD and the correlation coefficient between different moment orders, are important because they determine the standard errors of parameters estimated through DSD.

These works suggest that although disdrometers can offer insight into the microphysics of rain, one should recognize their limitations. Despite considerable previous work, we still need a rigorous examination of the implications that uncertainty has for drop diameter estimation, and we still don't fully comprehend how these uncertainties propagate to higher order moments.

Materials and methods

Experimental setup

Five Thies Laser Precipitation Monitors, hereafter referred as LPM, were collocated in the Iowa City Municipal Airport and placed every three meters in a north-south oriented line. A dual tipping bucket station (MRO01) and three Vaisala compact weather stations (WXT510) operate in the same area, separated by eight meters from the center of the disdrometer line. Three dual tipping bucket stations (ICA01, ICA02, and ICY13), organized in an equilateral triangle with 100m sides, also operate in the area. Figure A-1 summarizes the approximate location of the instruments and data availability.
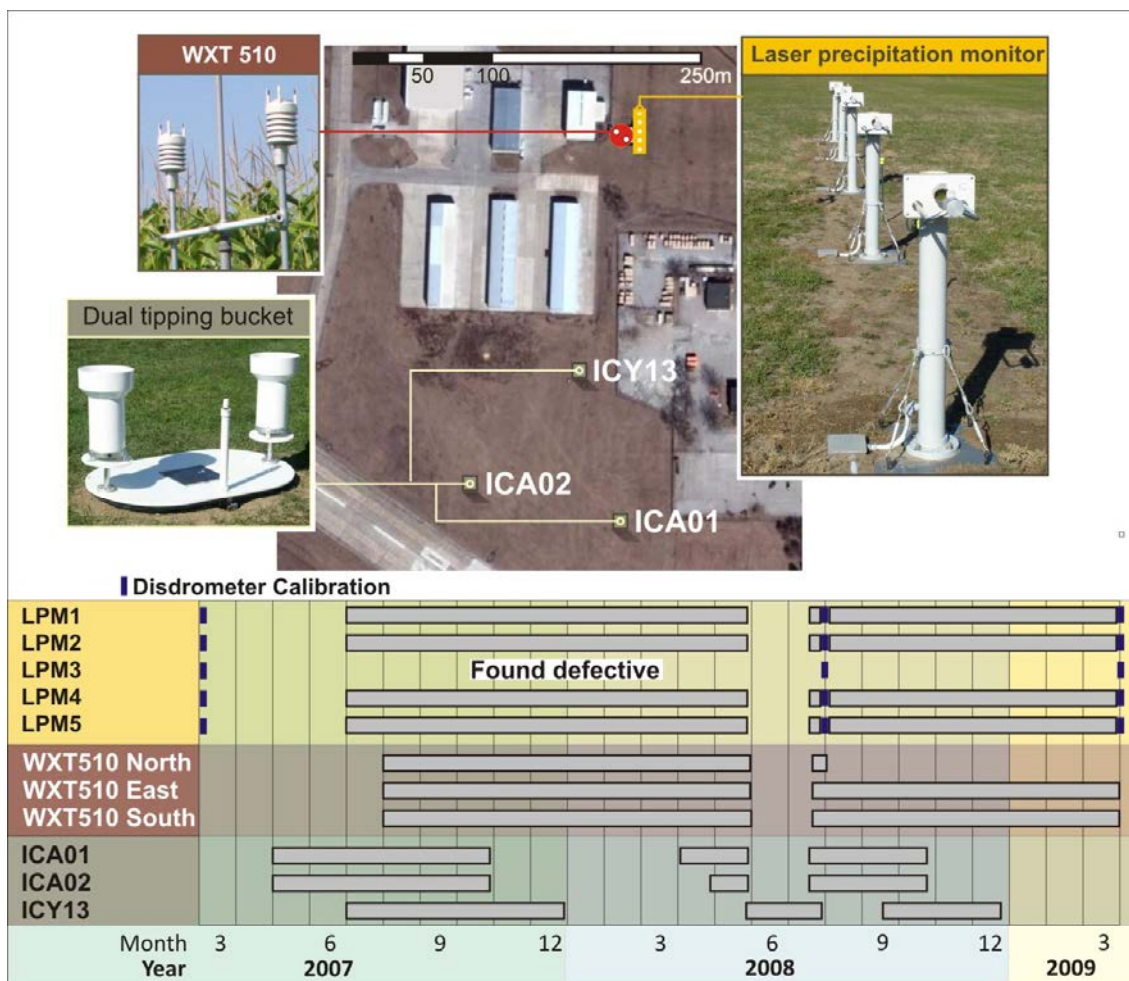
Figure A-1. Experimental setup showing the approximate location of the instruments and summary of data availability.

The disdrometers were operational from 4 July 2007 until 03 April 2009, with an interruption from 15 June 2008 to 26 June 2008, when power to some sections of the airport had to be discontinued. Interruptions for calibration occurred from 30 June 2008 to 7 July 2008 and from 21 July 2008 to 09 August 2008. The tipping buckets were removed from the field during the winter, so data was not available before April 2007 and between November 2007 and May 2008. Tipping bucket data was also not available from 13 June 2008 to 26 June 2008 due to the temporary relocation of our data servers. Two of the WXT510 stations were operational from 30 July 2007 to 03 April 2009 while

the third station was operational from 30 July 2007 to 08 August 2008. All three Vaisala Weather stations were down from 15 June 2008 to 26 June 2008 for the same reason as the disdrometers.

Timing synchronization

The LPM uses its internal clock to send one data telegram to the computer every minute. The software sold with the disdrometers disregards the instrument's internal clock and saves each block of 60 entries in a file that is named according to the computer's time in the format YYYYMMHH. As the data acquisition doesn't synchronize the disdrometers' internal clock with the computer's clock, the time derived from the file name is the only available source of data timestamp. The instrument cannot be set to work with different intervals nor can it send telegrams on demand. For this reason, the best time accuracy that can be achieved is one minute.

The four LPM's and the two Vaisala compact weather stations were connected to a single computer. Since they all used the computer time to save their data, they can be considered synchronized. The computer was connected to the internet through a wireless internet service and was supposed to synchronize with time servers, thereby keeping its internal clock as coordinated with the tipping bucket network as possible. Difficulties with internet service kept the computer from regularly synchronizing its clock with time servers. As this drift happens over time, it cannot be fixed simply by shifting the whole time series. Whenever it happened, it affected the LPMs and the compact weather stations in the same way, interfering with comparisons between tipping buckets and disdrometers. To overcome this problem with synchronization, we compared tipping bucket rain gauges and disdrometers only at one-hour accumulation levels and maximized the correlation coefficient between disdrometers and tipping bucket measurements for each storm separately.

Data binning

As mentioned, LPM can work in three different basic modes: drop-by-drop, one-minute accumulation, or tipping bucket-simulated mode. In the drop-by-drop mode, the instrument sends diameter and velocity measurements as well as status information to the computer upon an event, *i.e.* every time a drop crosses the laser beam. In the one-minute accumulation mode, the instrument sends a telegram containing the disdrometer's information, one and five minute rainfall-rate, visibility, type of precipitation and radar reflectivity, and a two dimensional matrix containing a count of all the drops recorded along the past minute.

This work uses the one minute accumulation mode, since the drop-by-drop mode requires an extremely high transmission rate because the number of drops passing the disdrometer's sensing volume can be large. For example, we recorded as many as 16,000 drops in a minute, with each telegram containing up to 50 characters. For this setup, even the maximum bandwidth might not be enough to convey all the information that could potentially result in the loss of data.

A table (22 lines and 20 columns) containing a summary of all drops recorded is provided each minute. Each element of this table is associated with a diameter and speed class. The first element stores the number of drops with a diameter between 0.125 and 0.250 mm and a speed of between 0 and 0.2m/s; the second element stores the number of drops with the same diameter but with speeds between 0.2 and 0.4 m/s. The following 20 elements encompass all velocities for the next diameter class and so on, covering diameters from 0.125 mm and 8 mm and velocities ranging from 0.2 m/s to 10 m/s. The result is a total of 440 bins. For more details, refer to the instrument's manual (Thies Clima, 2007).

Calibration Device

The uncertainty associated with the rainfall-rate measurement comes from various sources; one is the error in the estimation of the diameter of the volume-equivalent drop. The error in diameter propagates to other moments and can cause systematic and random deviations. Preliminary data analysis showed the existence of bias among the disdrometers. The bias motivated us to develop a calibration procedure in which the diameter of a well-known sphere would be repeatedly measured by the disdrometer and then contrasted to its nominal diameter.

We developed an instrument capable of deploying spheres of two, three, four, five, and six millimeters in diameter on approximately the same point of the disdrometer's laser sheet. Figure A-2 shows the schematics of the calibration device, which consists of a reservoir for the spheres, ending in a tunnel that leads them to the loading rod. The loading rod has a set of grooves, each one matching the size of the sphere currently being used. When the groove is aligned to the reservoir, it allows one sphere to be loaded. The loaded sphere is deployed when the loading rod is moved to the release position; its loaded groove is aligned with an opening at the bottom of the calibration device; and the sphere is released. The calibration device has two supports that adjust to the disdrometer's frame and align the center of the device's outlet with the center of the laser beam. The release height of the spheres was chosen to provide the spheres with enough height to achieve a velocity of approximately one meter per second at the height of the beam.

We checked the steel spheres' diameters with a caliper and found no deviations from their nominal diameter to a tenth of a millimeter. Consequently, we assumed that the nominal diameter is the real diameter of the sphere, which allows us to refer to the difference between disdrometer measurement and nominal diameter as a measurement error. The average error for each instrument is an indication of bias in the diameter

measurement, while the standard deviation of the error will characterize the precision of the diameter measurement.
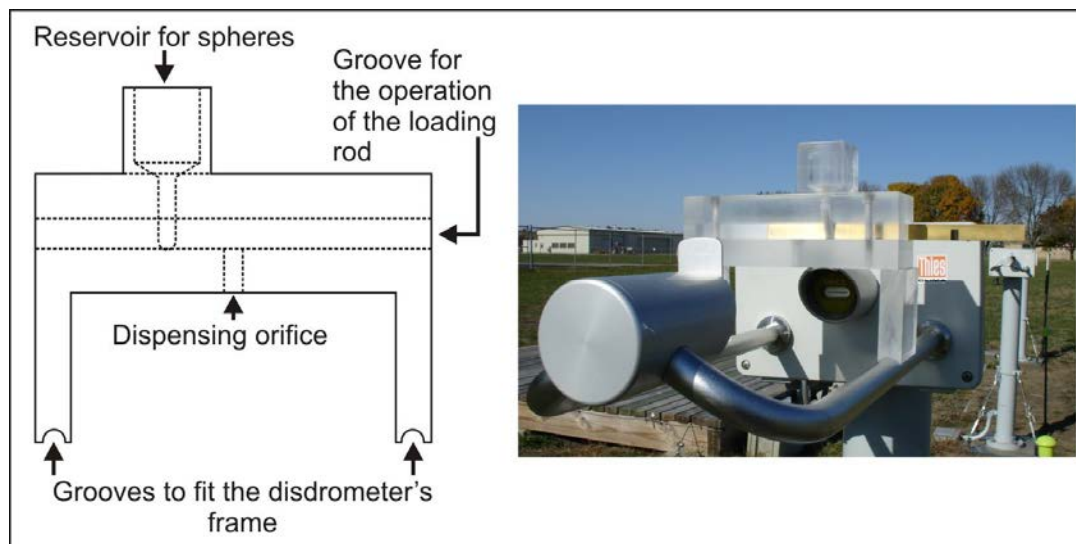
Figure A-2. Schematics of the calibration device alongside with a picture of the device set on a disdrometer during a field calibration.

Simulation studies

Computer simulation of the calibration procedure assuming different beam patterns

We developed a computer routine that simulates the functioning of the LPM to better understand the reasons for the discrepancies between nominal and measured diameters found during calibration. We hypothesized that the differences in the measurements come from inhomogeneities on the laser beam pattern due to imperfection on the lenses which cause the measured diameter to be dependent upon the location where the sphere falls.

We tested three arbitrary beam patterns, all based on a Gaussian distribution, with the edges of the beam corresponding to different percentiles of the distribution

controlling how uniform the beam is. The most uniform condition corresponds to using the 50% central area of the Gaussian distribution (cropped at the 12.5 and 87.5 percentiles). The other two cases used the 75% and 99.6% central area of the Gaussian distribution, respectively. Figure A-3 shows the simulation schematics for the first examined beam pattern and illustrates the effects of the position, where the drop enters the sensing volume, on the measured diameter.
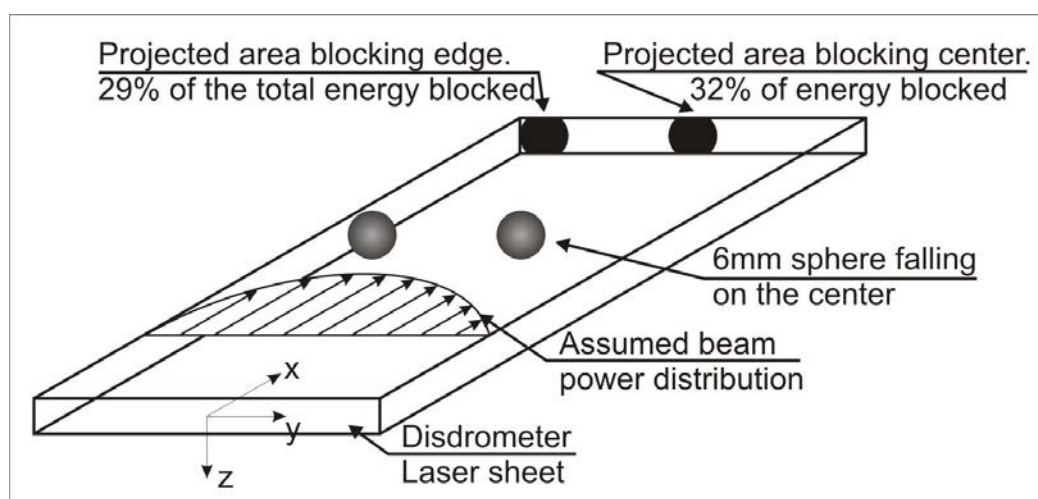
Figure A-3. Simulation schematics performed to estimate the error in the diameter measurement caused by an assumed Gaussian beam pattern with the tails removed at the 25th percentile and 75th percentile. Only the two extreme cases are shown, when a sphere falls

Propagation of the diameter measurement uncertainty into

rainfall accumulation using a Monte-Carlo simulation

We developed a Monte-Carlo simulation to propagate the uncertainty in the diameter measurement to the rainfall-rate estimation. We used the 2008 calibration data as an estimate of the uncertainty in the measurement of sphere diameters and fitted statistical distributions to the relative discrepancies between measured sphere diameter and nominal sphere diameter for each disdrometer separately. We chose four scenarios

for this study, each composed of one hour rainfall measurements, with rainfall accumulations of 5.8mm, 12.3mm, 15.33mm, and 31.9mm, respectively. To explore the effect of different diameter error configurations on the calculation of the rainfall accumulation, we created several error distributions that were based on the beta distribution and normalized to reflect a multitude of average and standard deviations of the relative deviations from the nominal diameter.

The simulation comprised the reading of the raw disdrometer data, integration in time to obtain one-hour drop matrices, construction of one vector per examined hour containing the diameter of each drop (simulating drop-by-drop measurements), subtraction of the simulated error from the diameter measurement, and subsequent recalculation of the rainfall rate. Analysis of the Monte Carlo simulation convergence indicated that repetition of this calculation about 1,500 times is enough to allow the determination of the average and standard deviation of the difference between simulated and original rainfall accumulation. This relatively low value is due to the elevated number of drops collected during one hour of rain which, for one of the studied cases when the accumulation was approximately 31.9 mm, exceeded 360,000 drops.

<u>Results and discussion</u>

Calibration

The purpose of the calibration procedure is to check the diameter measurements and, if necessary, correct them. In our first attempt, we concentrated on uncertainties associated with the measurement of spheres, although we recognize that raindrops are not perfectly spherical. As the instrument is not able to measure the shapes of hydrometeors, our goal with this simplified and idealized case is to define the lower limit for the disdrometer uncertainty. Considerations about raindrop shape would be possible if we used two-dimensional video disdrometers (Kruger and Krajewski, 2002).

We repeated the procedure four times. The first time began in 2005 when the calibration was done outdoors and ended in 2006 when the instruments were sent to the manufacturer for repair and upgrade. When the instruments were returned in the beginning of 2007, we conducted an indoor calibration on two of them before sending all instruments back to the field. After another year and a half of operation, we repeated the outdoors calibration procedure from July through August of 2008. The instruments remained in operation until April of 2009 when we brought them back indoors and executed a final round of calibration to assess the integrity of the instruments. Table A-1 presents statistics summarizing the evolution of the calibration results throughout the years.

We tested different materials to examine the influence of the sphere transparency and smoothness on the results. We tried glass (borosilicate), white rough plastic (nylon), dark smooth plastic (Polyamide-imide), and steel. Table A-2 shows the comparison of the average error and the standard deviation of the error for different materials on the same instrument. Despite the different behavior of the instrument with respect to the sphere's constituting material, we decided to remain with steel spheres as they are more readily available in the desired diameters.

Table A-1 shows the evolution of the average error alongside the error standard deviation over the years. The calibration executed in 2005 revealed that, on average, all four disdrometers were underestimating the diameter of the spheres by approximately half a centimeter, which presents a rather large bias if one considers that all errors in the estimation of the diameter are raised to the power of three when the rainfall rates are calculated. We applied the calibration curves obtained in 2008 to the disdrometers' raw data in the comparison of rainfall accumulations, as they were closer to the conditions the instruments faced during the storms. The dataset, which comprises at least 100 measurements per diameter, is shown in Figure A-4 to illustrate how dispersed the measurements can be.
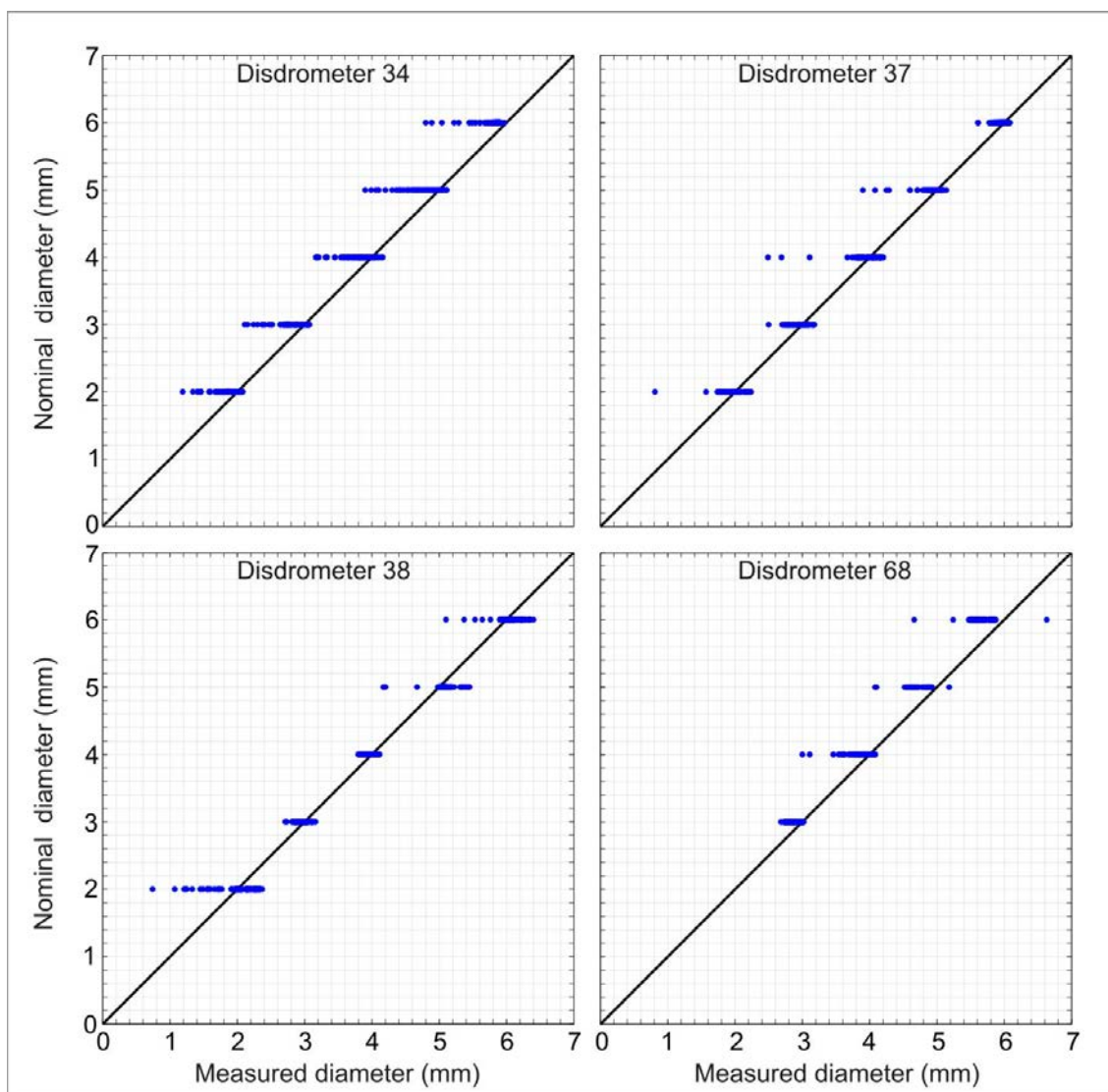
Figure A-4. Calibration data obtained in 2008. Solid lines represent the 1:1 line, points on the left of it are underestimating the diameter of the sphere and points on the right are overestimating their size. The calibration curves discussed in the next section come from linear regression on each of these panels.

Table A-1. Evolution of the calibration for the five disdrometers.

| | 2005 Outdoors | | | | 2007 Indoors | | 2008 Outdoors | | 2009 Indoors | |
| | Ave. Error (mm) | (mm) | Instrument | Ave. Error (mm) | (mm) | Ave. Error (mm) | (mm) | Ave. Error (mm) | (mm) |
Instrument									
Disd A	-0.60	0.38	0033	N/A		0.07	0.22	0.44	0.24
Disd B	-0.50	0.39	0034	N/A		-0.20	0.20	0.28	0.24
Disd C	-0.54	0.35	0037	N/A		-0.04	0.14	0.13	0.25
Disd D	-0.49	0.41	0038	-0.03	0.26	0.01	0.18	-0.21	0.47
Disd E	-0.59	0.35	0068	-0.20	0.20	-0.23	0.17	-0.08	0.17
Number of measurements	300			850		500		1000	

Note: Before 2006 the instruments were referred to as Disdrometers 1 to 5. During the repair and update, the manufacturer introduced the identities 0033, 0034, 0037, 0038, 0068 in the disdrometer communication protocol, which were used after that date.

Table A-2. Summary of the calibration attempts using different materials: glass (Borosilicate), dark plastic (Polyamide-imide), white plastic (Nylon) and steel, respectively.

	Glass	Brown plastic	White plastic	Steel
Number of measurements	241	178	312	310
Nominal diameters (mm)	2.38, 3.18, 3.96, 4.76, 5.53	3.18, 3.46, 4.76	2.38, 3.18, 3.96, 4.76	2, 3, 4, 5, 6
Ave. error (mm)	-0.68	-0.66	-0.76	-0.49
(mm)	0.48	0.59	0.73	0.41

Note: Average error corresponds to the average difference between the disdrometer measurement and a sphere's nominal diameter and   stands for the standard deviation of the referred differences.

Table A-3. 2009 Calibration results for each examined diameter.

	33		34		37		38		68	
Nominal diam. (mm)	Ave. error (mm)	(mm)	Ave. error (mm)	(mm)	Ave. error (mm)	(mm)	Ave. error (mm)	(mm)	Ave. error (mm)	(mm)
2	0.16	0.22	0.12	0.17	0.16	0.13	-0.13	0.44	-0.12	0.22
3	0.32	0.20	0.24	0.18	0.19	0.16	-0.26	0.51	-0.04	0.15
4	0.48	0.15	0.29	0.25	-0.09	0.32	-0.09	0.47	-0.04	0.13
5	0.58	0.13	0.34	0.24	0.12	0.29	-0.30	0.43	-0.09	0.14
6	0.65	0.11	0.44	0.21	0.26	0.17	-0.28	0.44	-0.11	0.18

Note: 200 repetitions were conducted for each diameter, which corresponds to a total of 1000 measurements per disdrometer. Average error corresponds to the average difference between the disdrometer measurement and a sphere's nominal diameter and stands for the standard deviation of the referred differences.

We repeated the calibration procedure once more, this time indoors, in 2009. This time, we measured 200 spheres of each diameter, which resulted in a sample size of 1000 observations per disdrometer. A closer examination of these results, presented in Table A-3, reveals an increasing average error on the disdrometers 33 and 34 with increasing sphere diameters, which is consistent with errors caused by non-homogeneous beams. To clarify this, let us examine how an instrument with a homogeneous beam estimates the sphere's size.

The diameter of a falling hydrometeor is estimated by the magnitude of the drop in the photodiode's voltage. This drop occurs when an object completely or partially blocks the laser beam illuminating the diode. The larger the object is, the larger the blocked beam area. In the homogeneous beam case, the shaded area is linearly related to the amount of energy that reaches the photodiode despite the location where the hydrometeor falls, provided that it falls entirely on the beam. The amount of energy reaching the diode is translated to the body's diameter.

The shaded area can be calculated with the use of equation A-1, which uses a Cartesian coordinate system where x is a horizontal axis running along the beam, *i.e.* pointing from the emitter towards the receiver with its origin on the center of the beam, y is a second horizontal axis that runs across the beam, and the z-axis is a vertical axis originating on the vertical center of the beam, as illustrated in Figure A-3.

The other terms in equation A-1 are *A*, which stands for the maximum area of the beam that is shaded by the sphere, *d,* which is the diameter of the sphere, and *h,* which is the height of the beam. Equation A-1 is valid if the diameter of the sphere is larger than the beam height (0.75mm) and if the body doesn't hit the horizontal edges of the beam, *i.e.* the y-coordinate of the center of the sphere is within the limits presented in equation A-2, where *W* stands for the beam width, which is 20mm, and *d* is the diameter of the body, which varies from 2 to 6mm in the investigated cases. The maximum shaded area is achieved when the center of the sphere is aligned with the vertical center of the beam.

$$A = h \cdot \sqrt{d^2 - \left(\frac{h}{2}\right)^2} + \frac{d^2}{4} \cdot \sin^{-1}\left(\frac{h}{d}\right) \tag{A-1}$$

$$\frac{W-d}{2} \geq y_{c \geq} \frac{d-W}{2} \tag{A-2}$$

In existing optical disdrometers, the energy emitted by the beam is non-uniform, adding more uncertainty to the estimation of the diameter. With a varying intensity, the received power is no longer linearly related to the shaded area, and different sections of the beam will be more or less efficient in blocking the beam's energy. To demonstrate the influence of the beam power distribution on the estimation of the diameters, we conducted a Monte Carlo simulation assuming 3 different beam patterns. The beam pattern "A" corresponds to the center section of a normal distribution encompassing 50% of the total area under the curve, beam pattern "B" includes 75% of the total area; and "C" includes 99.7% of the original area. The calibration device deploys the spheres on the center of the beam with a certain variation, which is normally distributed with a zero average and a varying standard deviation according to equation A-3.

$$\sigma_y = \frac{1}{3}\left(\frac{W-d}{2}\right) \tag{A-3}$$

Our analysis of the number of iterations necessary for the convergence of the average error in the diameter measurement pointed towards 3,000. To estimate the standard deviation of the error, 10,000 iterations were required.

According to the disdrometer's manufacturer, the original factory calibration is done with 4mm spheres deployed at 15 different beam positions. Using the simulation, we estimate the factor that we must apply to all simulated diameters in order eliminate the bias at the 4 mm diameter. Table A-4 shows the results of the average, standard deviation, and skewness of the error in the diameter measurement for the three different beam patterns. The average error decreases until it reaches 0 at the 4mm spheres and then increases. For distributions "A" and "C", the standard deviation increases with the increasing diameter, while for distribution "B", the standard deviation decreases with increasing sphere diameters. Figure A-5 shows the distribution of the relative differences

between simulated and nominal diameter for the three cases. The right panel shows a

slight increase in the probability distribution around -0.3, which resembles what happens

with disdrometers 34 and 37 in Figure A-6.

Table A-4. Average error and error standard deviation derived from the simulated
calibration, assuming a Gaussian beam pattern with the tails removed at the
25th percentile and 75th percentile and a normally distributed sphere position
across the beam with average 0 and standard deviation according to the sphere
diameter.

Beam Pattern	Diameter (mm)	Average error (mm)	Average relative error	Error standard deviation (mm)	Error skewness (mm3)
	2	-0.674	-0.337	0.04	-21.38
	3	-0.004	-0.001	0.09	-9.27
A	4	0.000	0.000	0.11	-7.13
	5	0.003	0.001	0.11	-6.47
	6	0.001	0.000	0.12	-7.22
	2	-0.097	-0.049	0.07	-2.81
	3	-0.004	-0.001	0.07	-3.93
B	4	0.000	0.000	0.06	-3.07
	5	-0.124	-0.025	0.04	-2.63
	6	-0.126	-0.021	0.04	-2.87
	2	-0.070	-0.035	0.56	-1.18
	3	0.016	-0.005	0.75	-1.46
C	4	0.000	0.000	0.89	-1.46
	5	0.033	0.007	0.98	-1.65
	6	0.566	0.094	1.29	-5.59

Note: Total number of iterations of 20,000 per sphere diameter.

Figure A-6 shows the differences between the measured and nominal diameters

for all 5 diameters with 200 measurements per diameter, as measured in the 2009

calibration as well as the simulated results using the 50% Gaussian beam pattern. Even

though the magnitudes of the average error, error standard deviation, and skewness do

not match those of the real data, the overall pattern of the simulated data is similar to

what disdrometers 33, 34, and 37 presented, in which both distributions are negatively

skewed with long tails and a comparatively sharp cut on the right side.
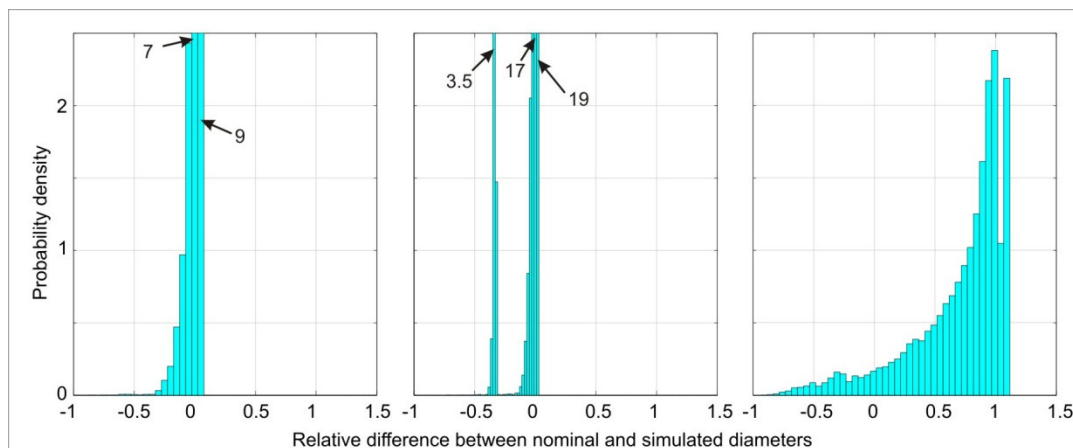
Figure A-5. Probability density plots of the relative difference between the simulated
           diameter and the nominal diameter for three alternative beam patterns. The
           left panel employed a beam power distribution that corresponds to the 75%
           central area of a normal distribution. The central panel's beam pattern utilized
           50% of the central area of a normal distribution and, the right panel shows a
           more extreme case, when 99.6% of the normal distribution is used to represent
           the beam pattern.

In Table A-5, disdrometers 37, 38, and 68 showed minimum absolute average

error for the diameter of 4mm, which is also the case for the simulated data shown in

Table A-4. The behavior of the error standard deviation obtained through calibration

wasn't similar to any of the three simulated beam patterns. We see two possible reasons

for the disagreement. The first is the small number of measurements, while the second

relates to the choice beam patterns for the simulations. Our study of the Monte Carlo

simulation convergence indicated that thousands of repetitions per diameter are needed to

reliably estimate the error standard deviation. In the experiment, we had 200

measurements per diameter, which might not have been enough to accurately determine

the error standard deviation.
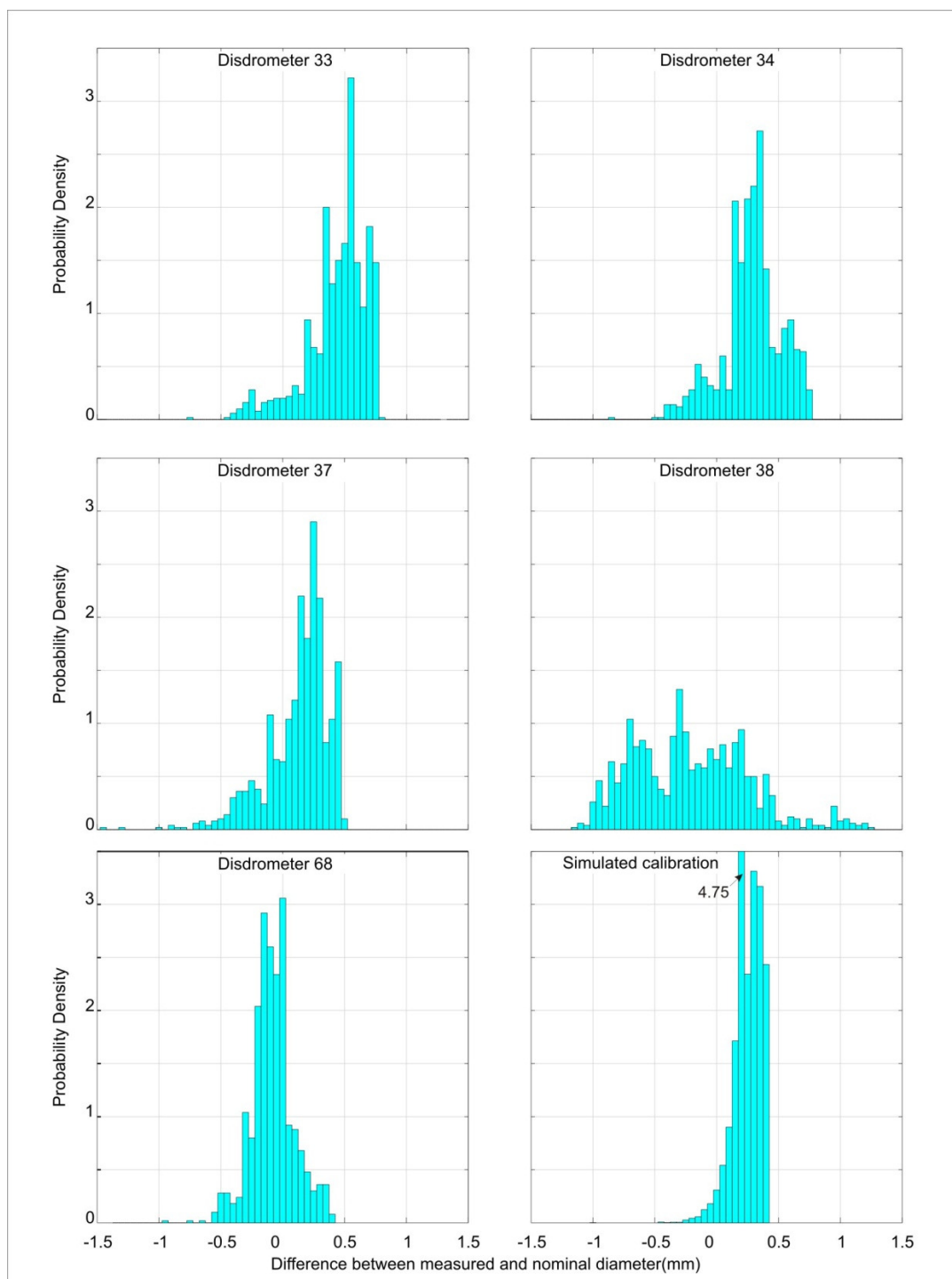
Figure A-6. Probability density plots for the 2009 calibration for each of 5 instruments alongside the results from the computer simulated calibration. Experimental plots generated from 1000 measurements of spheres with diameters of 2, 3, 4, 5, and 6mm (200 repetitions per diameter) for each instrument. Simulated plot representing measurements of 2, 3, 4, 5, and 6mm spheres with 10,000 measurements each.

Table A-5. Summary of simulation results showing how drops of 2, 3, 4, 5, and 6mm would be seen if they fell on the edge of the beam as opposed to falling on the center, assuming a Gaussian beam pattern with the tails removed at the 25th and 75th percentile.

Diameter	Position	Estimated diameter (mm)	Variation amplitude (mm)	Blocked Power
2	center	2.14	0.34	11%
	edge	1.80		9%
3	center	3.22	0.48	16%
	edge	2.74		14%
4	center	4.29	0.57	21%
	edge	3.72		18%
5	center	5.36	0.63	27%
	edge	4.72		24%
6	center	6.41	0.67	32%
	edge	5.75		29%

As shown in Table A-4, the standard deviation can increase or decrease with increasing sphere diameters, depending on the selected beam pattern. At this point, we have no measurements of disdrometers' beam power distributions, and we have only studied a small number of arbitrary distributions. Future work involves developing a method to obtain these distributions. The measured beam pattern will be used in the simulation to obtain a more realistic representation of instrument operation. Most likely, a combination of the two described factors, along with others still unknown at this time, is responsible for the lack of uniformity.

Data filtering

Upon consideration of the one-hour accumulations readings calculated from the disdrometer results, we found some suspicious points where only one disdrometer

reported drops. One of these points registered readings as high as 114 mm of

accumulated rainfall in one hour. The unlikelihood of such a localized and intense

rainfall led us to further investigate that hour. When examining the drop-size distribution

at that moment, we found a pattern that is highly unlikely to be associated with natural

rainfall, as shown in Figure A-7.
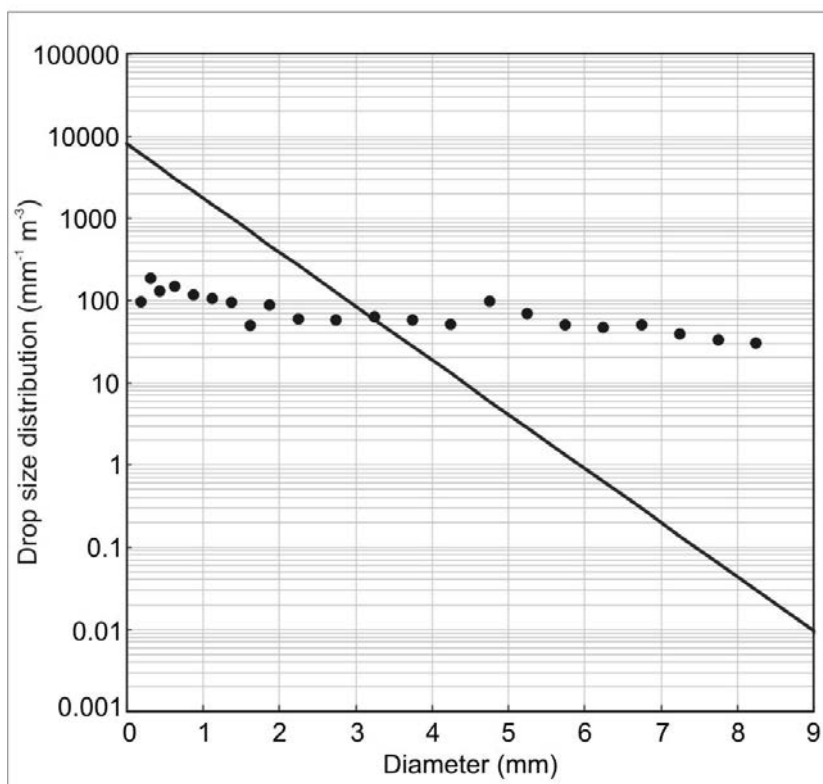
Figure A-7. Suspicious drop-size distribution registered during a 1-hour event detected
by a single disdrometer. The distribution showed as a reference corresponds
to the Marshall-Palmer distribution (Marshall and Palmer, 1948) fitted to
114mm/h. The almost constant concentration of drops with respect to average
class diameter is unlikely to happen in natural rainfall. Data was further
scrutinized to identify such occurrences, and these points were eliminated
from the rest of the analysis.

Instead of observing a falling concentration of drops with increasing diameter, we

observed a quite constant concentration in all diameters, especially of hydrometeors

larger than 8mm. Although we could not explain this concentration, we believe it was not the result of natural precipitation and should be removed from the rest of the analysis.

We searched the remaining data for hours when only one instrument detected accumulations in excess of one millimeter per hour, checked the drop-size distribution for that hour, and removed those that displayed improbable drop-size distributions. The number of hours of data removed from the study was different for each instrument and ranged from 1 to 6 in 2007 and from 1 to 19 in 2008. For comparison purposes, the disdrometers collected data for 2,175 hours in the first year and for 3,908 hours in the second. In most of the removed hours, the anomaly lasted for no more than five minutes. Although we don't have an explanation for the anomalies, they are easy to identify and remove from the dataset. As this type of inconsistency occurred for all disdrometers during the whole period of data collection, this procedure could be adopted as a simple quality control system to filter out anomalies from the Thies optical disdrometer.

<div align="center">Rainfall accumulation comparison</div>

Table A-6 shows the accumulations for all of the instruments. The accumulations for 2007 refer to the period of 01 August 2007 to 31 October 2007, when all instruments were online. A malfunction of the interface between one of the Vaisala compact weather stations (WXT 510 North) and the data acquisition computer prevented us from having a complete dataset for all instruments in 2008. In Table A-6, the line 2008* shows the rainfall accumulation between 1 May 2008 and 09 July 2008, when the connection with the WXT 510 North failed. During this period, all four disdrometers, three dual tipping bucket stations, and three compact weather stations were functional.

In 2007, the maximum disagreement between the three dual tipping bucket stations was on the order of 3%. In 2008*, the ICY13 station showed an underestimation of about 10% with respect to the average of the other tipping bucket station. Three

specific hours were decisive for the disagreement of the ICY13 and the average of the other 2 stations, and they accounted for 29mm of the missing water for that station.

The dates were 3 June 2008 between 13:00 and 14:00 UTC, 26 June 2008 between 03:00 and 04:00 UTC, and 8 July 2008 between 20:00 and 21:00 UTC. On these three occasions, a flag indicated that the data-logger memory was full and an unknown number of tips was lost. If those points were removed from the data series, the accumulation for the period would be 293.3mm, 294.53mm, and 288.20 mm for the Stations ICA01, ICA02, and ICY13, respectively. This corresponds to a maximum deviation from the mean of approximately 2%. The same is valid for the 2008 series. If these three points are removed from the series, the maximum difference between tipping buckets would be on the order of 1%.

The other instruments did not perform as well. In the accumulation level, we see the presence of bias among disdrometers, among compact weather stations, and also among disdrometers and weather stations with respect to tipping buckets. For instance, let us look at the 2007 accumulation. If one compares disdrometer 1 with disdrometer 5, we see that there are close to 127mm of rainfall missing, which corresponds to a deviation of 18% from the average of the other 3 disdrometers. Disdrometer 1 overestimated the rainfall rate by approximately 20% with respect to the average of the other three disdrometers, while disdrometers 2 and 4 respectively underestimated and overestimated the rainfall accumulation by about 5% with respect to the average of the other instruments.

In 2008, the discrepancy between disdrometer 1 and the rest of the group increased, while the other three disdrometers reported less dissimilar values. The difference between accumulation derived from disdrometer 1 data and the average accumulation derived from the other three disdrometers' data for the period of 2008* was nearly 150mm, which corresponded to an overestimation of 30% of the average of the other disdrometers.

When we apply the calibration curve derived from the 2008 calibration data, we notice an improvement in the agreement among disdrometers. In 2007, the worst deviation of calibrated data, *i.e.* between disdrometer 1 and the average accumulation of the other disdrometers, decreased from an overestimation of 20% to an overestimation of 9%. The same behavior happened with the 2008 data, when calibration successfully reduced the disagreement between disdrometers. However, when we compare disdrometers with the tipping bucket rain gauges, the advantage of applying the calibration curve was not so obvious.

Similar overestimations were found by Lanzinger et al. (2006) when comparing three Thies optical disdrometers with pit rain gauges. In their experiment, the laser disdrometers overestimated the rainfall accumulation by approximately 5%, 15%, and 20% with respect to pit gauges. Lanza and Vuerich (2009) compared 1-minute rainfall intensities derived from tipping buckets, weighing gauges, and optical disdrometers measurements and also reported the overall trend of optical disdrometers overestimating rainfall amounts with respect to a reference rainfall, which was the weighted average of several different types of instruments. For more details on this experiment refer to Vuerich et al. (2009).

Still, Table A-6 shows that applying the calibration curve to the disdrometers approximated the average disdrometer accumulation for the year 2007 to the average accumulation of the WXT 510, with the former going from a non-calibrated average of 442 mm to 473 mm after applying the calibration curve. This brings it closer to the compact weather stations' accumulation of 503mm. When this comparison is repeated for the 2008* period, the average disdrometer accumulation goes from 510 mm to 546 mm while the average WXT 510 shows only 452 mm. The same distancing between the instruments occurs in 2008, when the average disdrometer accumulation goes from 801 mm to 856 mm while the compact weather stations recorded an average of 735 mm of rainfall.

Table A-6. Comparison of the rainfall accumulations for the years 2007 and 2008.

Year		Disdrometers				WXT 510			Tipping Buckets		
		1	2	4	5	East	North	South	ICA01	ICA02	ICY13
2007	Not calibrated	506.0	424.4	458.5	379.3	531.7	476.0	502.6	351.1	353.2	343.2
	Calibrated	501.1	477.4	472.4	439.1						
2008*	Not calibrated	619.8	466.7	490.4	465.0	481.2	437.6	438.8	342.3	344.2	310.4
	Calibrated	613.8	525.0	505.2	538.3						
2008	Not calibrated	967.4	730.0	782.2	724.5	764.2	N/A	706.7	570.8	577.3	544.5
	Calibrated	958.2	821.2	805.9	838.7						

Note: The 2008* line shows a limited dataset for which all instruments were online (1 May 2008 until 09 July 2008), and the 2008 line shows the accumulated values from 1 May 2008 until 31 October 2008. Non-calibrated values were calculated from the disdrometer's drop matrix outputted by the instruments and only corrected for each device's specific catchment area. The 2008 calibration curves were used to calculate the calibrated disdrometer data for both years. No calibration is available for either the tipping buckets or the WXT510.

We cannot explain the apparent better suitability of the 2008 calibration curve to the 2007 dataset. Since the calibration data was collected in June of 2008, it should better fit 2008 than 2007. Application of the calibration curve obtained in 2009 (performed inside the laboratory) deteriorates the convergence of the disdrometer's accumulations. Furthermore, in the 2009 calibration data, we see negative average errors for sensor 38 (disdrometer 1), positive errors for sensors 34 and most of 37, respectively (disdrometers 2 and 4), and negative errors for sensor 68 (disdrometer 5). Negative errors during calibration indicate the instrument's tendency to underestimate the drop's diameter and, consequently, rainfall. However, during the operation, rain rates and rainfall accumulations were overestimated by disdrometer 1.

This lack of repeatability indicates that the readings could be influenced by lighting or atmospheric conditions during calibrations. We expect that the lack of wind explains the observed behavior, as spheres driven by wind would fall more consistently off the center of the laser beam leading to more underestimation of the diameter of the spheres. The added influence of varying wind velocities should also increase the error standard deviation. Revisiting Table A-1, we see that the error standard deviation increased for all disdrometers. The tendency to overestimate diameter indoors (2009) as opposed to outdoors (2008) only occurred for sensors 33 (no rain data collected), 34 (disdrometer 2), and 37 (disdrometer 4) and was reversed for sensors 38 (disdrometer 1) and 68 (disdrometer 5). For these reasons, we are uncertain at this point whether applying the 2008 calibration curve to the dataset is indeed beneficial.

The differences between the instruments' accumulations do not come from single unexplained or unpredictable occurrences but rather from long-term trends, which, in principle, could be removed by calibration without the need to change hardware. To support this statement, let us look at 1-hour accumulation comparisons between measurements of each disdrometer and the average of the other 3 disdrometers, shown in Figure A-8.
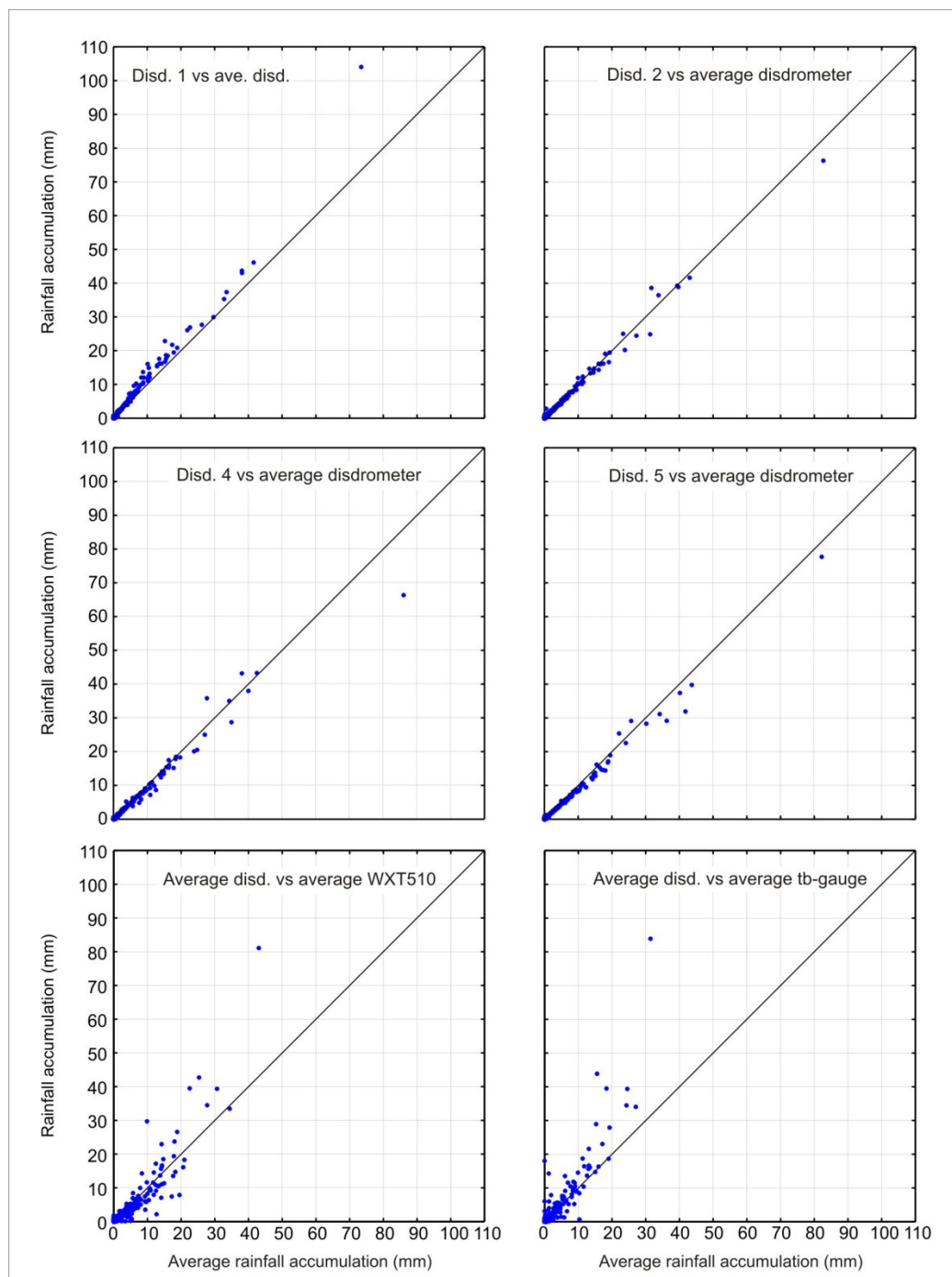
Figure A-8. Comparison of the one-hour accumulations as seen by disdrometers, compact weather stations (WXT 510), and tipping bucket rain-gauges. Individual disdrometers are compared to the average of the other disdrometers. One-hour accumulations derived from average disdrometer data are compared to the corresponding average WXT510 data and tipping bucket data. Plots comprise the period of 2007 and 2008*, as shown in Table 6.

We used the whole dataset (2007 and 2008) to create this figure. As one of the WXT 510 was not functional for the whole 2008 period, it was excluded from the last panel. The solid black line in all panels represents a 1:1 line, where all points should fall in a perfect situation without bias or spread. Points falling above the line indicate overestimation by the examined instrument, while points falling under the line represent underestimation. By looking at the first panel comparing disdrometer 1 with the average of the other three disdrometers, the long-term trend of overestimation of rates is evident. It is also apparent that instruments using the same principle of measurement agree better than those using different methods, which is not unheard of in the literature and was pointed out by Lanzinger et al. (2006) and Vuerich et al. (2009).

We investigated the effects of wind speed and direction on the differences between average disdrometer and tipping bucket hourly rain accumulations but failed to establish a relationship between them. We examined the relationship between wind speed and discrepancies between instruments by plotting the two quantities, which didn't reveal a pattern. We also calculated the correlation coefficient between the instruments' discrepancies and wind speed and found a value very close to zero, indicating no linear relationship. Comparing the wind direction with the differences in rainfall accumulations was done in a different manner, as the direction is a cyclic variable.

We classified the wind direction into perpendicular to the disdrometer axis (West - East or vice versa) or parallel to the disdrometer axis (North - South or vice versa) and looked at the distribution of the discrepancies between disdrometers and tipping bucket measurements, provided that there was rain. We observed a slightly higher average difference between instruments when the wind was perpendicular to the disdrometers and a higher standard deviation of these differences when the wind was parallel to the disdrometers. Quantitatively, the average difference between tipping bucket and disdrometer hourly rain accumulation under perpendicular wind was 0.3mm with a

standard deviation of 1.5mm. The same quantities with parallel wind were 0.5mm and 3.2mm, respectively. Figure A-9 presents the two distributions.
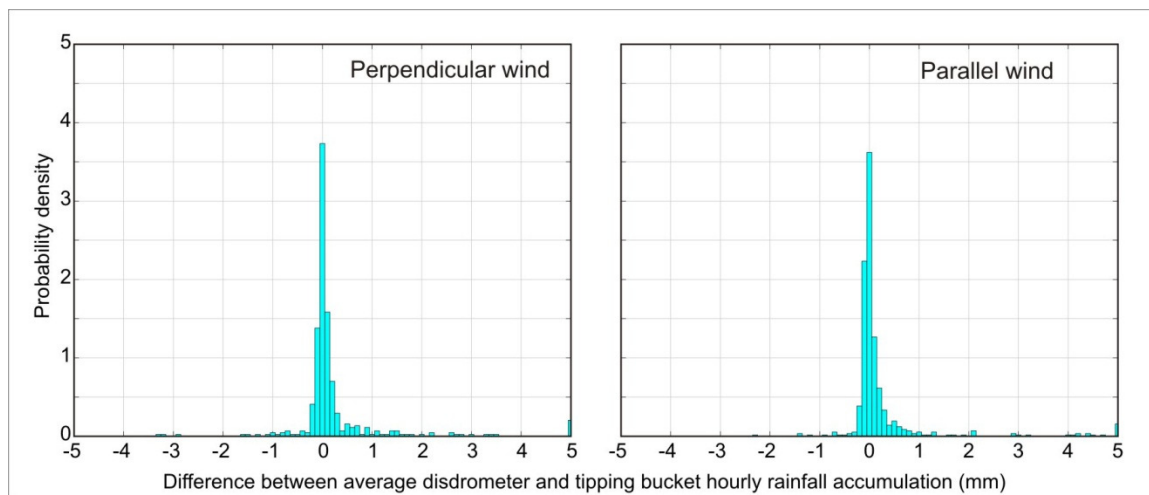
Figure A-9. Distributions of the discrepancies between 1-hour average disdrometer rainfall accumulations and 1-hour accumulations derived from the average tipping bucket data. The left hand side shows the distribution under perpendicular wind and the right hand side shows the distribution of the discrepancies with parallel wind. Both distributions only describe hours when there was at least one instrument measuring rainfall.

One other important question when comparing instruments is how long to integrate them in order to obtain meaningful results. If we integrate for too long, we lose time resolution. On the other hand, if we do not wait long enough, our data will be too variable, noisy, and not statistically representative. Figure A-10 shows how increasing the integration time influences the spread of the data. This figure shows four plots of one of the disdrometers against the average of the other three disdrometers at four integration intervals of 1, 5, 15, and 30 minutes.

By examining Figure A-10, it becomes apparent that increasing the integration time improves the agreement between sensors and that the spread of the data varies with rainfall intensity. Although this is an expected result, we examined the evolution of the

square of the correlation (r^2) of each disdrometer with respect to the average of the other

three. We examined 7 integration intervals, namely 1, 2, 5, 15, 30, 60, and 120 minutes,

and present the results in Figure A-11. The figure shows that the longer we integrate, the

better the linear relation is between instruments. The gain in correlation is more

pronounced when increasing the integration interval up to 5 minutes. After 30 minutes,

we observed no more real gain in terms of correlation. This comparison should be taken

with some caution, as the number of intervals contained in the data decreases as we

integrate for longer times.
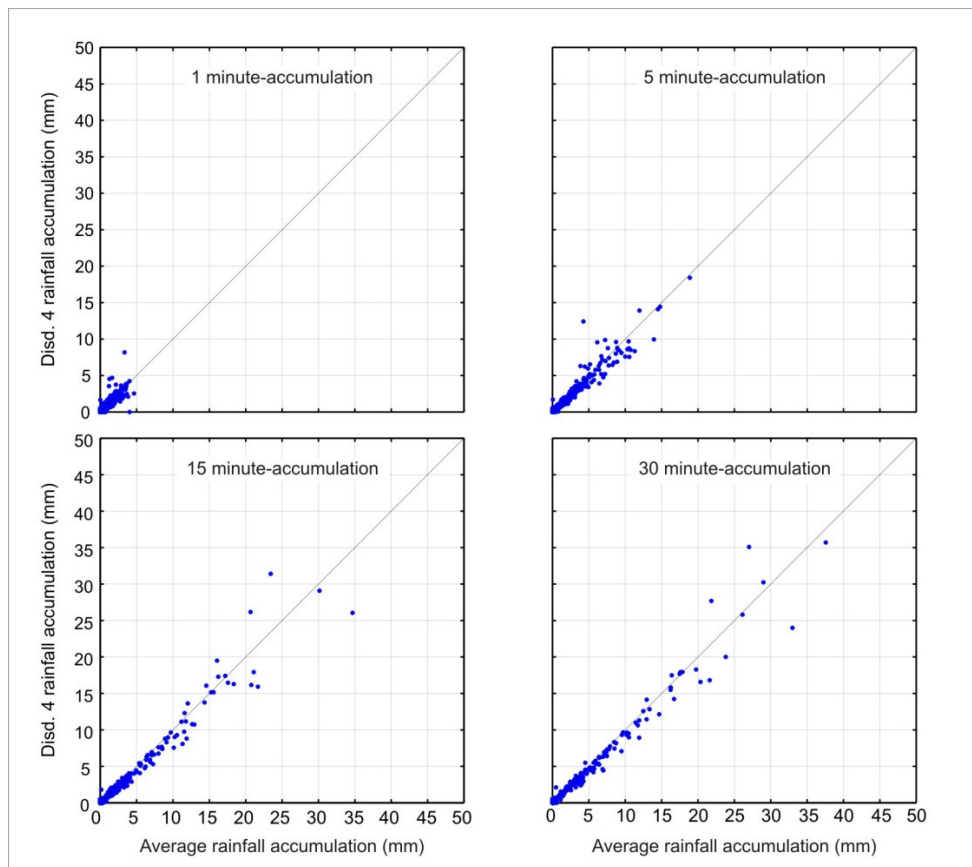
Figure A-10. Example of the effect of the integration interval on the agreement between
disdrometer and average disdrometer. The plots depict how the 1, 5, 15, and
30 minute rainfall accumulations derived from a typical LPM disdrometer
agree with the average of neighboring disdrometers. Displayed data comprise
the period of 2007 and 2008*, as illustrated in Table V-6.
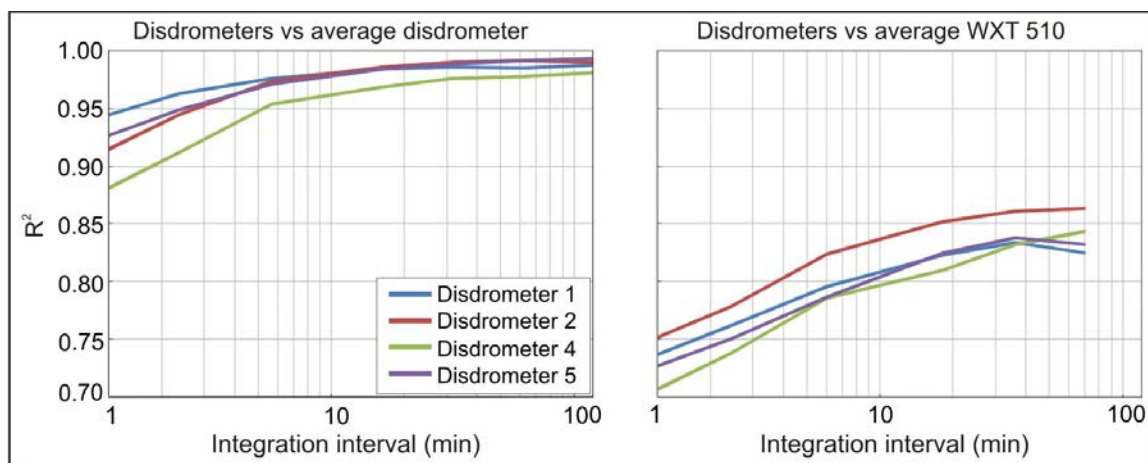
Figure A-11. The left hand side panel shows how the square of the correlation coefficient between disdrometer and average rainfall accumulation changes with respect to the accumulation time. The right hand side shows the behavior of the square of the correlation coefficient between each disdrometer and the average WXT 510 accumulation at different accumulation times.

It is also apparent in Figure A-10 that the average error and the error standard deviation change with accumulation amount. To investigate this dependency, we broke the series into 30 classes of 60-minute accumulations with respect to the average disdrometer accumulations at each corresponding integration interval. The first and the last classes are the only ones with different numbers of elements. The first groups all intervals with an average accumulation of at least 0.1mm. At the highest resolution, this first class indicates how well the instruments detect the onset of rainfall. The other classes had their limits chosen in order to contain the same number of elements. This criterion was selected in order to minimize the effect of sample size in the comparison across classes.

The left-hand side panel of Figure A-12 shows the dependency of the average difference between one disdrometer estimate and the average of the other instruments with respect to the average rainfall accumulation. Higher rainfall accumulation corresponds to higher average deviation. The pattern is quite linear, as shown by the

values of the correlation between the average rainfall accumulation and average difference of each disdrometer and the average of the others, as reflected in Table A-7. Lanza and Vuerich (2009), when comparing optical disdrometers with rain gauges, also observed an increase in the differences between the two instruments with increasing rainfall rate, which is consistent with the increasing bias in the rainfall accumulations with respect to the reference accumulation we present on the left panel of Figure A-12. We also observed an increase in the spread of the rainfall accumulation measurements with increasing average accumulations, as shown in the right panel of Figure A-12.
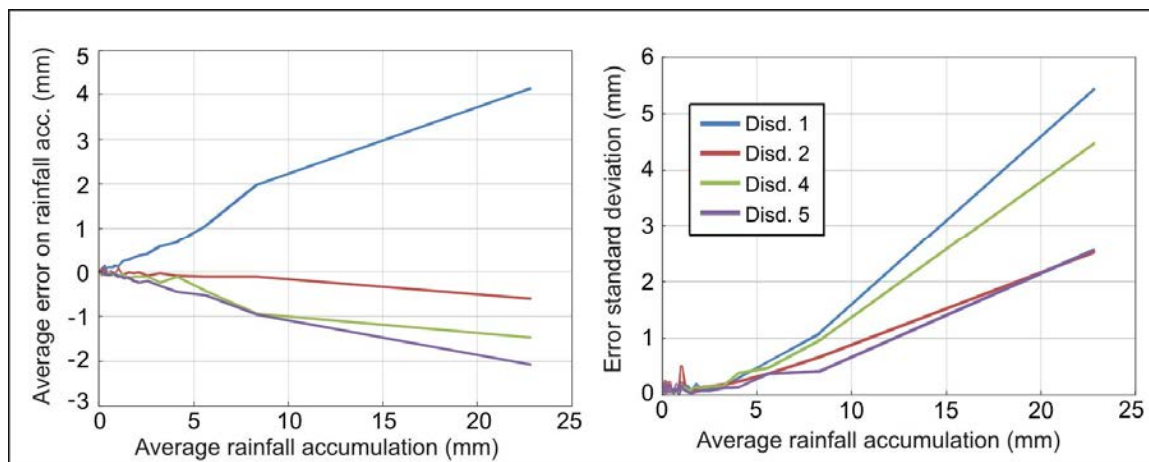
Figure A-12. The left hand side shows the average difference between individual disdrometers and the average of the other three calculated for 30 classes of one-hour rainfall accumulation. The right hand side panel shows the standard deviation of these differences, plotted against the average rainfall accumulation. We used 1-hour accumulations in this plot and designed each class width in order to produce homogenous counts at each class, with the exception of the first class (<0.1mm) and the last class (>10.9mm), which had counts of 5491 and 28 elements, respectively. All other classes had 21 elements each.

A possible source of bias that would not be detected in the calibration of the diameter measurements and would be consistent with the linear rising average difference between instruments with respect to the average rainfall accumulation is error in the

determination of the disdrometer's laser area. Although we used the areal correction factor provided by the disdrometers in our computations, if the correction factors were not correctly determined in the factory, they would cause such behavior.

Table A-7. Squared correlation coefficient between the average 1-hour rainfall accumulation and the average, standard deviation, and skewness of difference between each disdrometer's reading and the corresponding rainfall accumulation.

	R^2		
Disdrometer	Average "error" versus average rainfall accumulation	of the "error" *vs* average rainfall accumulation	"Error" skewness and rainfall accumulation
1	0.99	0.92	0.03
2	0.89	0.91	0.01
4	0.93	0.94	0.04
5	0.99	0.89	0.01

Note: "Error" in this table refers to the difference between each disdrometer's reading and the average of the other disdrometers.

Uncertainty propagation

By means of a Monte Carlo simulation, we studied how errors in diameter estimation propagate to the estimation of one hour rainfall accumulation. By subtracting the error from the diameter measurement, we attempt to find a correction for the rainfall estimated by the examined diameter. The average correction addresses the bias caused by errors in the diameter measurement, while the standard deviation of this correction indicates the amount of spread in the rainfall accumulation that can be attributed to errors in the diameter measurement. We worked with two stages, each covering four cases.

In the first stage, we used arbitrary shapes for the diameter relative error distribution to study the effects of its direction of the skewness, standard deviation, and average on the rainfall accumulation correction.

In this stage of the study, we chose the Beta distribution since it can assume diverse shapes, thereby allowing us to study the effects of the average, standard deviation, and skewness of the relative error of the diameter measurement into the rainfall accumulation. We worked with three sets of values for   and , the first set varying from = 1 and = 8 to = 8 and =8 and finally =8 and = 1, the second set varying from = 1 and = 32 to = 32 and =32 and finally =32 and = 1, and the third set from = 1 and = 64 to = 64 and =64 and finally =64 and = 1, allowing us to cover positively skewed distributions, symmetric distributions, and negatively skewed distributions with more or less pronounced peaks.

As the Beta distribution is restricted to the interval between zero and one, we first divided the vector containing the randomly generated diameter relative errors by its own standard deviation. We then multiplied it by the desired standard deviation and translated the error vector to force it to have the desired average. We tested average relative errors of -0.1 (supposing that the hypothetical disdrometer would, on average, underestimate the drop size by 10%), -0.05, 0 (in average, no bias), 0.05, and 0.1. For the standard deviation of the diameter relative error, we used values of 0.04, 0.1, and 0.16. The disdrometers presented average diameter relative errors of 0.002, -0.06, -0.001, and -0.05 and standard deviations of 0.06, 0.06, 0.04, and 0.03 during the 2008 calibration.

Table A-8 summarizes the results from the first stage of this analysis. Qualitatively, the average rainfall correction is not particularly sensitive to the skewness of the diameter relative error distribution unless the average relative error in the diameter is smaller, in absolute value, than the standard deviation. In those cases, when the average relative error of the diameter measurement is of the same order of magnitude, 0.1 (average underestimation of the diameter of 10%) and 0.16, respectively, the rainfall correction for an hour of rain that originally registered 31.9 mm changed from -6.7mm to -6.2mm with a change of skewness from 1.94 to -1.93. In the extreme tested case, when the average diameter relative error was 0 and the standard deviation was 0.16, the rainfall

correction for the same studied hour changed from 2.20mm to 2.70mm with the same change in skewness. This shows that, although the change in the correction was more pronounced than in the previous case, it is still negligible when compared to the original rainfall accumulation.

Table A-8. Summary of the Monte Carlo simulation designed to propagate the errors in the diameter measurement to the 1-hour rainfall accumulation.

Disdrometer	Original rainfall accumulations		Corrected rainfall accumulations	
	Hour 1	Hour 2	Hour 1	Hour 2
1	43.0	7.4	43.2	7.4
2	39.3	6.8	46.5	8.1
4	43.2	6.4	44.6	6.6
5	31.9	5.8	37.0	6.8

Note: The diameter relative error was subtracted from the measured diameter, for four non-consecutive hours of rainfall measurements. Diameter error distribution "A" was based on a Beta distribution with parameters = 8 and = 8, "B" = 1 and = 64, "C" = 64 and = 64 and "D" = 64 and = 1 modified to have the presented average and standard deviation.

The same degree of insensitivity to changes in the relative error distribution of the diameter does not apply to the spread of the rainfall correction. In all instances, the standard deviation of the rainfall correction is significantly affected by changes in the skewness of the diameter relative error distribution. These changes can be as small as approximately 15%, when the average diameter relative error was 0.1, the standard deviation 0.04, and the skewness changed from 1.90 to -1.90, with the corresponding rainfall correction standard deviation changing from 0.028 to 0.033 or as large as 66% for average diameter relative error of 0.1, standard deviation 0.16, and similar change in skewness with corresponding rainfall correction standard deviation going from 0.010 to 0.017.

The determining factors in the magnitude of the rainfall correction average and standard deviation are the average and the standard deviation of the diameter relative error. An unbiased measurement of the diameter still leads to a slight positive correction of the rainfall accumulation. A higher standard deviation of the relative error in the diameter yields a higher correction of the rainfall accumulation. However, the corrections never accounted for more than 7.7% of the original rainfall accumulation. For other cases, when bias in the diameter measurement was present, the magnitude of the average rainfall correction was still dependent upon the standard deviation of the relative error in the diameter measurement.

The higher the standard deviation, the higher the correction, provided that the correction is positive. If the rainfall accumulation correction is negative, then the absolute value of the correction decreases. The standard deviation of the rainfall correction is also affected by the spread in the diameter measurements. Higher standard deviation of the relative error in diameter is associated with higher variability of the rainfall accumulation correction. We observed that increasing the standard deviation of the relative error on the diameter measurement by a factor of four would correspond to an increase of approximately four times in the spread of the rainfall accumulation corrections.

Comparison of average rainfall correction obtained by this simulation with the correction factor obtained by linear regression on the calibration data produced similar results. Previously, if a disdrometer on average underestimated the diameter of spheres by 10%, the correction on the rainfall accumulation would correspond to an increase by a factor of 1.331, *i.e.* 1.10 elevated to the third power. For the first case shown in Table A-8, an underestimation of 10% in the diameter, with corresponding standard deviation of the relative error of 0.04, led to a correction of 10.7mm to the rainfall accumulation of 31.9 mm, while a correction in the same accumulation by a factor of 1.331 corresponds to 10.6mm. In cases when the disdrometer overestimates the diameter of falling drops with

the same 0.04 standard deviation of the relative error, we still observe good correspondence between the results obtained through Monte-Carlo simulation and simple linear regression on a hypothetical calibration.

Differences between the results obtained through Monte-Carlo simulation and the linear regression methodology arise when the average and the standard deviation of the relative error in the diameter are on the same order of magnitude. In these cases, the linear regression method underestimates positive rainfall accumulation corrections and overestimates (in absolute value) the negative rainfall accumulation corrections.

In Table A-8, average and standard deviation of the diameter relative error of 0.1 and 0.04, respectively, lead to a correction of -8.5mm, while the linear regression method would lead to a correction of -8.6mm, both of which are applied to the original rainfall accumulation of 31.9mm. If the standard deviation of the relative error on the diameter was 0.16, the correction suggested by the Monte-Carlo simulation method would be -6.4mm.

In the second stage, we used the 2008 calibration data for disdrometer 5. The errors in the diameter measurement had a normal distribution with an average of -0.05 and standard deviation 0.0339, as shown in the first panel of Figure A-13. The proposed corrections and the estimation of the spread of the rainfall accumulations account for errors in the determination of the diameter only and do not address errors due to rainfall sampling, quantization of drop sizes, detection of simultaneous drops, or any other sources of uncertainty. The second panel of Figure A-13 shows the distribution of rainfall accumulation corrections for one of the studied cases, when the original rainfall accumulation totaled 31.9mm. The average of this distribution could be used to correct the rainfall accumulation for that hour, leading to a new total of 37.0mm.

Although we could not approach the relative error of the other disdrometer's diameter measurements as well, the results of the previous stage suggest an insensitivity of the average rainfall accumulation correction to the shape of the relative error diameter

error distribution. Table A-9 shows the effect of applying the proposed correction to these two particular hours of measurements.
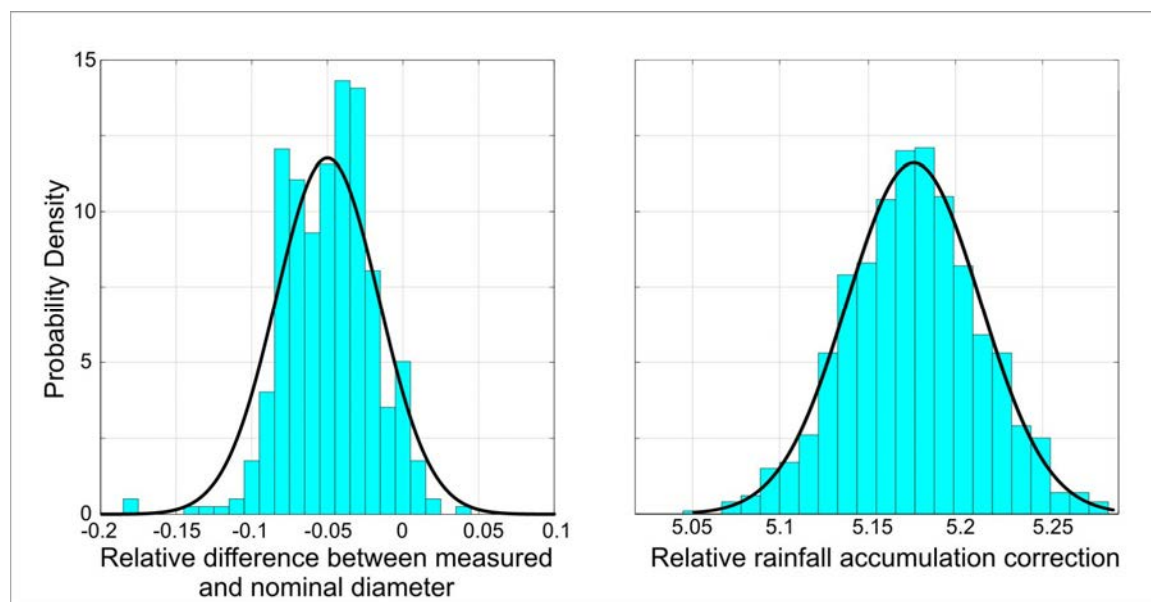
Figure A-13. Original and transformed distribution of the relative error in the diameter measurement obtained with disdrometer 5 during the outdoors calibration procedure executed in 2008 and the resulting distribution of the rainfall accumulation correction for one hour of sample rainfall data with original accumulation of 31.9mm.

Overall, there was an increase in the rainfall accumulations, with the more visible effects apparent in the two instruments that were underestimating the rainfall accumulation with respect to the other disdrometers. Although this procedure seemed beneficial for the two studied cases, it is time consuming if applied to large datasets. Its real value consists of its tests of "what if" scenarios, as it allows for an assessment of the effects of the quality of the diameter measurements (determined by the optical characteristics of the lenses, quality of the laser emitter and receiver characteristics of the lenses, quality of the laser emitter and receiver, and signal sampling rate) in the rainfall accumulation estimation.

Table A-9. Results of adding the rainfall accumulation correction two hours of
measurements.

Distribution	Diameter relative error (all dimensionless)			Rainfall correction (mm)	
	$\overline{d}$	σ_d	Skewness$_d$	$\overline{R}$ (mm)	σ_R (mm)
A	-0.1	0.04	-0.01	10.7	0.05
A	0	0.04	0.00	0.2	0.04
A	0.1	0.04	0.00	-8.5	0.03
A	-0.1	0.16	0.00	13.2	0.18
A	0	0.16	0.00	2.5	0.15
A	0.1	0.16	0.00	-6.4	0.13
B	-0.1	0.04	1.91	10.7	0.04
C	-0.1	0.04	0.00	10.7	0.04
D	-0.1	0.04	-1.90	10.7	0.05
B	0	0.04	1.89	0.1	0.03
C	0	0.04	0.00	0.2	0.04
D	0	0.04	-1.90	0.2	0.04
B	0.1	0.04	1.91	-8.5	0.03
C	0.1	0.04	0.01	-8.5	0.03
D	0.1	0.04	-1.90	-8.5	0.03
B	0.1	0.16	1.94	-6.7	0.10
C	0.1	0.16	0.00	-6.4	0.13
D	0.1	0.16	-1.93	-6.2	0.18

Note: The original values are calculated from the disdrometer's raw data. Applying the
proposed correction reduced the mean square difference from individual disdrometers
to the average from 20.9 mm to 12.7mm for the first hour, while slightly increased the
mean square difference for the second case.

Summary and conclusions

We compared rainfall accumulations measured by four Thies LPM disdrometers, three Vaisala WXT510, and three dual tipping bucket stations at time resolutions ranging from 1 minute to 1 hour. The four disdrometers displayed bias, only partially addressed by calibrating the diameter measurements, which increased the agreement between disdrometers. Furthermore, disdrometers' accumulations were generally distanced from accumulations measured by WXT510 or tipping bucket rain gauges. The partial success of calibration indicates that other factors cause the discrepancies, and we hypothesized that the visible bias between disdrometers and between disdrometers and other gauges could be caused by miscalculation of the disdrometer's sensing area.

The strong linear relations between the disdrometers, especially at the 1-hour accumulation level, suggest that if the bias can be eliminated, the instruments are very promising. They provide reliable measurements yet require low maintenance. We didn't observe the same level of linearity between disdrometers and compact weather stations, nor between disdrometers and tipping bucket stations, unless one looks exclusively at storm totals. Analysis of the relationship between wind speed and direction and differences between instruments, aside from showing a stronger spread when the wind was parallel to the disdrometer axis, didn't explain the discrepancies.

We developed a computer simulation to study the effects of three different non-skewed beam patterns on the diameter measurements. We concluded that even though the simulated average error, error standard deviation, and error skewness didn't match their corresponding parameters in the calibration data, the described model reproduced the overall shape of the diameter measurement distributions, most noticeably the negative skewness with long tails and a comparatively sharp cut on the right side of the error distributions of three disdrometers.

In the last section, we present the results of a Monte Carlo simulation designed to propagate the errors from the measurement of diameters into the rainfall accumulations.

We used the results of this simulation to correct the disdrometers' measurements for two non-consecutive hours of measurements, which improved the agreement among disdrometers, although apparently overcorrected the accumulation for one of the instruments. Nonetheless, this method can be used to predict the effects of using different optical setups on the estimation of rainfall accumulations.

REFERENCES

Alves, D.R.B., Frizzone, J.A. and Neto, D.D., 2001. Repartição da lâmina de irrigação, aplicada via pivô central, na cultura do milho. Revista Brasileira de Engenharia Agrícola e Ambiental, 5(1): 67-70.

Armstrong, C.L. and Mitchell, J.K., 1987. Transformations of Rainfall by Plant Canopy. Transactions of the Asae, 30(3): 688-696.

Armstrong, C.L. and Mitchell, J.K., 1988. Plant canopy characteristics and processes which affect transformation of rainfall properties. Transactions of the Asae, 31(5): 1400-1409.

Barthazy, E., Goke, S., Schefold, R. and Hogl, D., 2004. An optical array instrument for shape and fall velocity measurements of hydrometeors. Journal of Atmospheric and Oceanic Technology, 21(9): 1400-1416.

Bassette, C. and Bussière, F., 2005. 3-D modelling of the banana architecture for simulation of rainfall interception parameters. Agricultural and Forest Meteorology, 129(1-2): 95-100.

Bassette, C. and Bussière, F., 2008. Partitioning of splash and storage during raindrop impacts on banana leaves. Agricultural and Forest Meteorology, 148(6-7): 991-1004.

Berry, E.X. and Pranger, M.R., 1974. Equations for calculating terminal velocities of water drops. Journal of Applied Meteorology, 13(1): 108-113.

Biskup, B., Scharr, H., Schurr, U. and Rascher, U., 2007. A stereo imaging system for measuring structural parameters of plant canopies. Plant Cell and Environment, 30(10): 1299-1308.

Bonhomme, R. and Varletgrancher, C., 1978. Estimation of gramineous crop geometry by plant profiles including leaf width variations. Photosynthetica, 12(2): 193-196.

Brandt, C.J., 1989. The size distribution of throughfall drops under vegetation canopies. Catena, 16(4-5): 507-524.

Brandt, C.J., 1990. Simulation of the size distribution and erosivity of raindrops and throughfall drops. Earth Surface Processes and Landforms, 15(8): 687-698.

Brawn, D. and Upton, G., 2008. Estimation of an atmospheric gamma drop size distribution using disdrometer data. Atmospheric Research, 87(1): 66-79.

Bui, E.N. and Box, J.R., 1992. Stemflow, rain throughfall and erosion under canopies of corn and sorghum. Soil Science Society of America Journal, 56: 242-247.

Bussière, F., Solmon, F. and Fouere, A., 2002. Implementation and evaluation of DROP, a model for the simulation of rainfall distribution below plants described in 3D. Agronomie, 22(1): 93-103.

Calder, I.R., 1986. A stochastic model of rainfall interception. Journal of Hydrology, 89(1-2): 65-71.

Calder, I.R., 1996. Dependence of rainfall interception on drop size .1. Development of the two-layer stochastic model. Journal of Hydrology, 185(1-4): 363-378.

Calder, I.R., Hall, R.L., Rosier, P.T.W., Bastable, H.G. and Prasanna, K.T., 1996. Dependence of rainfall interception on drop size .2. Experimental determination of the wetting functions and two-layer stochastic model parameters for five tropical tree species. Journal of Hydrology, 185(1-4): 379-388.

Campos, E. and Zawadzki, I., 2000. Instrumental uncertainties in Z-R relations. Journal of Applied Meteorology, 39(7): 1088-1102.

Cao, Q. et al., 2008. Analysis of video disdrometer and polarimetric radar data to characterize rain microphysics in Oklahoma. Journal of Applied Meteorology and Climatology, 47(8): 2238-2255.

Caracciolo, C., Prodi, F. and Uijlenhoet, R., 2006. Comparison between Pludix and impact/optical disdrometers during rainfall measurement campaigns. Atmospheric Research, 82(1-2): 137-163.

Chambelland, J.C. et al., 2008. A double-digitising method for building 3D virtual trees with non-planar leaves: application to the morphology and light-capture properties of young beech trees (Fagus sylvatica). Functional Plant Biology, 35(9-10): 1059-1069.

Ciach, G.J., 2003. Local random errors in tipping-bucket rain gauge measurements. Journal of Atmospheric and Oceanic Technology, 20(5): 752-759.

Constantinescu, G.S., Krajewski, W.F., Ozdemir, C.E. and Tokyay, T., 2007. Simulation of airflow around rain gauges: Comparison of LES with RANS models. Advances in Water Resources, 30(1): 43-58.

de Ploey, J., 1982. A stemflow equation for grasses and similar vegetation. Catena, 9: 139-152.

Dolan, M.S., Dowdy, R.H. and Lamb, J.A., 2001. Redirection of precipitation by a corn canopy and related soil water status. Communications in Soil Science and Plant Analysis, 32(5-6): 739-750.

Donnadieu, G., 1980. Comparison of results obtained with the vidiaz spectropluviometer and the Joss-Waldvogel rainfall disdrometer in a rain of a thundery type. Journal of Applied Meteorology, 19(5): 593-597.

Dornbusch, T., Wernecke, P. and Diepenbrock, W., 2007. A method to extract morphological traits of plant organs from 3D point clouds as a database for an architectural plant model. Ecological Modelling, 200(1-2): 119-129.

EOS Systems Inc., 2008a. Photomodeler 6.

EOS Systems Inc., 2008b. Photomodeler User's manual.

España, M., Baret, F., Aries, F., Andrieu, B. and Chelle, M., 1999a. Radiative transfer sensitivity to the accuracy of canopy structure description. The case of a maize canopy. Agronomie, 19(3-4): 241-254.

España, M., Baret, F., Chelle, M., Aries, F. and Andrieu, B., 1998. A dynamic model of maize 3D architecture: application to the parameterisation of the clumpiness of the canopy. Agronomie, 18(10): 609-626.

España, M.L. et al., 1999b. Modeling maize canopy 3D architecture - Application to reflectance simulation. Ecological Modelling, 122(1-2): 25-43.

Frasson, R.P.d.M., 2007. Observational studies of rainfall interception by corn, The University of Iowa, Iowa City, 102 pp.

Frasson, R.P.d.M., Cunha, L.K.d. and Krajewski, W.F., 2011. Assessment of the Thies optical disdrometer performance. Atmospheric Research, 101: 237-255.

Frasson, R.P.d.M. and Krajewski, W.F., 2009. Three-dimensional digital model of maize canopy 7th World Congress on Computers in Agriculture, Reno, Nevada.

Frasson, R.P.d.M. and Krajewski, W.F., 2010. Three-dimensional digital model of a maize plant Agricultural and Forest Meteorology, 150(3): 478-488.

Frasson, R.P.d.M. and Krajewski, W.F., 2011. Characterization of the drop-size distribution and velocity–diameter relation of the throughfall under the maize canopy. Agricultural and Forest Meteorology, 151(9): 1244-1251.

Gash, J.H.C., 1979. An analytical model of rainfall interception by forests. Quarterly Journal of the Royal Meteorological Society, 105: 43-55.

Grossklaus, M., Uhlig, K. and Hasse, L., 1998. An optical disdrometer for use in high wind speeds. Journal of Atmospheric and Oceanic Technology, 15(4): 1051-1059.

Gunn, R. and Kinzer, G.D., 1949. The terminal velocity of fall for water droplets in stagnant air. Journal of Meteorology, 6(4): 243-248.

Guo, Y. et al., 2006. Parameter optimization and field validation of the functional-structural model GREENLAB for maize. Annals of Botany, 97(2): 217-230.

Habib, E. and Krajewski, W.F., 2001. An example of computational approach used for aerodynamic design of a rain disdrometer. Journal of Hydraulic Research, 39(4): 425-428.

Hall, R.L., 2003. Interception loss as a function of rainfall and forest types: stochastic modelling for tropical canopies revisited. Journal of Hydrology, 280(1-4): 1-12.

Hall, R.L. and Calder, I.R., 1993. Drop size modification by forest canopies - Measurements using a disdrometer. Journal of Geophysical Research-Atmospheres, 98(D10): 18465-18470.

Hartley, G.S. and Brunskill, R.T., 1958. In: J.F. Danielli (Editor), Surface Phenomena in Chemistry and Biology. Pergamon Press, London, pp. 214-223.

Hauser, D., Amayenc, P., Nutten, B. and Waldteufel, P., 1984. A new optical instrument for simultaneous measurement of raindrop diameter and fall speed distributions. Journal of Atmospheric and Oceanic Technology, 1: 256-269.

Haynes, J.L., 1940. Ground rainfall under vegetative canopy of crops. Journal of the American Society of Agronomy, 32: 176-184.

Henning, J.G. and Radtke, P.J., 2006. Ground-based laser imaging for assessing three-dimensional forest canopy structure. Photogrammetric Engineering and Remote Sensing, 72(12): 1349-1358.

Hornbuckle, B.K., England, A.W. and Anderson, M.C., 2007. The effect of intercepted precipitation on the microwave emission of maize at 1.4 GHz. Ieee Transactions on Geoscience and Remote Sensing, 45(7): 1988-1995.

Hornbuckle, B.K., England, A.W., Anderson, M.C. and Viner, B.J., 2006. The effect of free water in a maize canopy on microwave emission at 1.4 GHz. Agricultural and Forest Meteorology, 138(1-4): 180-191.

Hosoi, F. and Omasa, K., 2006. Voxel-based 3-D modeling of individual trees for estimating leaf area density using high-resolution portable scanning lidar. Ieee Transactions on Geoscience and Remote Sensing, 44(12): 3610-3618.

Hosoi, F. and Omasa, K., 2007. Factors contributing to accuracy in the estimation of the woody canopy leaf area density profile using 3D portable lidar imaging. Journal of Experimental Botany, 58(12): 3463-3473.

Hupet, F. and Vanclooster, A., 2005. Micro-variability of hydrological processes at the maize row scale: implications for soil water content measurements and evapotranspiration estimates. Journal of Hydrology, 303(1-4): 247-270.

Illingworth, A.J. and Stevens, C.J., 1987. An optical disdrometer for the measurement of raindrop size spectra in windy conditions. Journal of Atmospheric and Oceanic Technology, 4: 411-421.

Ivanov, N., Boissard, P., Chapron, M. and Andrieu, B., 1995. Computer stereo plotting for 3-D reconstruction of a maize canopy. Agricultural and Forest Meteorology, 75(1-3): 85-102.

Ivanov, N., Boissard, P., Chapron, M. and Valery, P., 1994. Estimation of the height and angles of orientation of the upper leaves in the maize canopy using stereovision. Agronomie, 14(3): 183-194.

Joss, J. and Waldvogel, A., 1977. Some observations on Joss-Waldvogel rainfall disdrometer - Reply. Journal of Applied Meteorology, 16(1): 112-113.

Keim, R.F. and Skaugset, A.E., 2004. A linear system model of dynamic throughfall rates beneath forest canopies. Water Resources Research, 40(5).

Keim, R.F., Skaugset, A.E., Link, T.E. and Iroume, A., 2004. A stochastic model of throughfall for extreme events. Hydrology and Earth System Sciences, 8(1): 23-34.

Keim, R.F., Skaugset, A.E. and Weiler, M., 2006. Storage of water on vegetation under simulated rainfall of varying intensity. Advances in Water Resources, 29(7): 974-986.

Kiesselbach, T.A., 1949. The structure and reproduction of corn. University of Nebraska, Lincoln, 101 pp.

Kinnell, P.I.A., 1976. Some observations on Joss-Waldvogel rainfall disdrometer. Journal of Applied Meteorology, 15(5): 499-502.

Krajewski, W.F. et al., 2006. DEVEX-disdrometer evaluation experiment: Basic results and implications for hydrologic studies. Advances in Water Resources, 29(2): 311-325.

Kruger, A. and Krajewski, W.F., 2002. Two-dimensional video disdrometer: A description. Journal of Atmospheric and Oceanic Technology, 19(5): 602-617.

Kummerow, C., 2009. Cloud and precipitation retrievals from TRMM and GPM satallites - Impact of a-priory information, Joint Center for Satellite Data Assimilation Seminars.

Lamm, F.R. and Manges, H.L., 2000. Partitioning of sprinkler irrigation water by a corn canopy. Transactions of the Asae, 43(4): 909-918.

Lanza, L.G. and Vuerich, E., 2009. The WMO Field Intercomparison of Rain Intensity Gauges. Atmospheric Research, 94(4): 534-543.

Lanzinger, E., Theel, M. and Windolph, H., 2006. Rainfall amount and intensity measured by the Thies laser precipitation monitor, TECO-2006, Geneva, Switzerland.

Levia, D.F. and Frost, E.E., 2003. A review and evaluation of stemflow literature in the hydrologic and biogeochemical cycles of forested and agricultural ecosystems. Journal of Hydrology, 274(1-4): 1-29.

Levia, D.F. and Frost, E.E., 2006. Variability of throughfall volume and solute inputs in wooded ecosystems. Progress in Physical Geography, 30(5): 605-632.

Lewis, J., 2003. Stemflow estimation in a redwood forest using model-based stratified random sampling. Environmetrics, 14(6): 559-571.

Licznar, P., Lomotowski, J., Blonski, S. and Ciach, G.J., 2008. Microprocessor field impactometer calibration: Do we measure drops' momentum or their kinetic energy? Journal of Atmospheric and Oceanic Technology, 25(5): 742-753.

Limousin, J.M., Rambal, S., Ourcival, J.M. and Joffre, R., 2008. Modelling rainfall interception in a Mediterranean Quercus ilex ecosystem: Lesson from a throughfall exclusion experiment. Journal of Hydrology, 357(1-2): 57-66.

Loffler-Mang, M. and Joss, J., 2000. An optical disdrometer for measuring size and velocity of hydrometeors. Journal of Atmospheric and Oceanic Technology, 17(2): 130-139.

Magarey, R.D., Seem, R.C. and Russo, J.M., 2006. Grape canopy surface wetness: Simulation versus visualization and measurement. Agricultural and Forest Meteorology, 139(3-4): 361-372.

Marshall, J.S. and Palmer, W.M., 1948. The distribution of raindrops with size. Journal of Meteorology, 5(4): 165-166.

Miralles, D.G., Gash, J.H., Holmes, T.R.H., de Jeu, R.A.M. and Dolman, A.J., 2010. Global canopy interception from satellite observations. J. Geophys. Res., 115(D16): D16122.

Miriovsky, B.J., 2003. Towards the statistical characterization of small-scale rainfall variability using field experiments, The University of Iowa, Iowa City, 131 pp.

Montero-Martinez, G., Kostinski, A.B., Shaw, R.A. and Garcia-Garcia, F., 2009. Do all raindrops fall at terminal speed? Geophysical Research Letters, 36.

Morgan, R.P.C., 1985. Effect of corn and soybean canopy on soil detachment by rainfall. Transactions of the Asae, 28(4): 1135-1140.

Murakami, S., 2006. A proposal for a new forest canopy interception mechanism: Splash droplet evaporation. Journal of Hydrology, 319(1-4): 72-82.

Muzylo, A. et al., 2009. A review of rainfall interception modelling. Journal of Hydrology, 370(1-4): 191-206.

Nanko, K., Hotta, N. and Suzuki, M., 2004. Assessing raindrop impact energy at the forest floor in a mature Japanese cypress plantation using continuous raindrop-sizing instruments. Journal of Forest Research, 9(2): 157-164.

Nanko, K., Hotta, N. and Suzuki, M., 2006. Evaluating the influence of canopy species and meteorological factors on throughfall drop size distribution. Journal of Hydrology, 329(3-4): 422-431.

Nanko, K., Mizugaki, S. and Onda, Y., 2008. Estimation of soil splash detachment rates on the forest floor of an unmanaged Japanese cypress plantation based on field measurements of throughfall drop sizes and velocities. Catena, 72(3): 348-361.

Nespor, V., Krajewski, W.F. and Kruger, A., 2000. Wind-induced error of raindrop distribution measurement using a two-dimensional video disdrometer. Journal of Atmospheric and Oceanic Technology, 17(11): 1483-1492.

Norman, J.M. and Campbell, G.S., 1983. Application of a plant-environment model to problems in irrigation. In: D.I. Hillel (Editor), Advances in Irrigation. Academic Press, New York, pp. 155-188.

Nosonovsky, M., 2007. Model for solid-liquid and solid-solid friction of rough surfaces with adhesion hysteresis. Journal of Chemical Physics, 126(22).

Nosonovsky, M. and Bhushan, B., 2008. Energy transitions in superhydrophobicity: low adhesion, easy flow and bouncing. Journal of Physics-Condensed Matter, 20(39).

Nystuen, J.A., 1998. Temporal sampling requirements for automatic rain gauges. Journal of Atmospheric and Oceanic Technology, 15(6): 1253-1260.

Omasa, K., Hosoi, F. and Konishi, A., 2007. 3D lidar imaging for detecting and understanding plant responses and canopy structure. Journal of Experimental Botany, 58(4): 881-898.

Omasa, K., Hosoi, F., Uenishi, T.M., Shimizu, Y. and Akiyama, Y., 2008. Three-dimensional modeling of an urban park and trees by combined airborne and portable on-ground scanning LIDAR remote sensing. Environmental Modeling & Assessment, 13(4): 473-481.

Paltineanu, I.C. and Starr, J.L., 2000. Preferential water flow through corn canopy and soil water dynamics across rows. Soil Science Society of America Journal, 64(1): 44-54.

Parkin, T.B. and Codling, E.E., 1990. Rainfall distribution under a corn canopy - Implications for managing agrochemicals. Agronomy Journal, 82(6): 1166-1169.

Quinn, N.W. and Laflen, J.M., 1983. Characteristics of raindrop throughfall under corn canopy. Transactions of the Asae, 26(5): 1445-1450.

Raasch, J. and Umhauer, H., 1984. Errors in the determination of particle size distributions caused by coincidences in optical particle counters. . Particle Characterization, 1: 53-58.

Rutter, A.J. and Kershaw, K.A., 1971. A predictive model of rainfall interception in forests, 1. Derivation of the model for observations in a plantation of Corsican pine. Agricultural and Forest Meteorology, 9: 367-384.

Rutter, A.J. and Morton, A.J., 1977. Predictive model of rainfall interception in forests. 3. Sensitivity of model to stand parameters and meteorological variables. Journal of Applied Ecology, 14(2): 567-588.

Rutter, A.J., Morton, A.J. and Robins, P.C., 1975. Predictive model of rainfall interception in forests .2. Generalization of model and comparison with observations in some coniferous and hardwood stands. Journal of Applied Ecology, 12(1): 367-380.

Schellekens, J., Scatena, F.N., Bruijnzeel, L.A. and Wickel, A.J., 1999. Modelling rainfall interception by a lowland tropical rain forest in northeastern Puerto Rico. Journal of Hydrology, 225(3-4): 168-184.

Sinoquet, H., Moulia, B. and Bonhomme, R., 1991. Estimating the 3-dimensional geometry of a maize crop as an input of radiation models - Comparison between 3-dimensional digitizing and plant profiles. Agricultural and Forest Meteorology, 55(3-4): 233-249.

Sinoquet, H. and Rivet, P., 1997. Measurement and visualization of the architecture of an adult tree based on a three-dimensional digitising device. Trees-Structure and Function, 11(5): 265-270.

Sinoquet, H., Thanisawanyangkura, S., Mabrouk, H. and Kasemsap, P., 1998. Characterization of the light environment in canopies using 3D digitising and image processing. Annals of Botany, 82(2): 203-212.

Steiner, J.L., Kanemasu, E.T. and Clark, R.N., 1983. Spray losses and partitioning of water under a center pivot sprinkler system. Transactions of the Asae, 26(4): 1128-1134.

Thies Clima, 2007. Instructions for use. Laser precipitation monitor 5.4110.xx.x00 V2.2xSTD.889, 58 pp.

Tokay, A., Bashor, P.G. and Wolff, K.R., 2005. Error characteristics of rainfall measurements by collocated Joss-Waldvogel disdrometers. Journal of Atmospheric and Oceanic Technology, 22(5): 513-527.

Tokay, A., Kruger, A. and Krajewski, W.F., 2001. Comparison of drop size distribution measurements by impact and optical disdrometers. Journal of Applied Meteorology, 40(11): 2083-2097.

Tokay, A., Wolff, D.B., Wolff, K.R. and Bashor, P., 2003. Rain gauge and disdrometer measurements during the keys area microphysics project (KAMP). Journal of Atmospheric and Oceanic Technology, 20(11): 1460-1477.

Van der Zande, D., Stuckens, J., Verstraeten, W.W., Muys, B. and Coppin, P., 2010. Assessment of light environment variability in broadleaved forest canopies using terrestrial laser scanning. Remote Sensing, 2(6): 1564-1574.

van Dijk, A. and Bruijnzeel, L.A., 2001a. Modelling rainfall interception by vegetation of variable density using an adapted analytical model. Part 1. Model description. Journal of Hydrology, 247(3-4): 230-238.

van Dijk, A. and Bruijnzeel, L.A., 2001b. Modelling rainfall interception by vegetation of variable density using an adapted analytical model. Part 2. Model validation for a tropical upland mixed cropping system. Journal of Hydrology, 247(3-4): 239-262.

van Elewijck, L.L., 1989a. Influence of leaf and branch slope on stemflow amount. Catena, 16(4-5): 525-533.

van Elewijck, L.L., 1989b. Stemflow on maize: a stemflow equation and the influence of rainfall intensity on stemflow amount. Soil Technology, 2: 41-48.

Villarini, G., Mandapaka, P.V., Krajewski, W.F. and Moore, R.J., 2008. Rainfall and sampling uncertainties: A rain gauge perspective. Journal of Geophysical Research-Atmospheres, 113(D11).

Vivekanandan, J., Zhang, G.F. and Brandes, E., 2004. Polarimetric radar estimators based on a constrained gamma drop size distribution model. Journal of Applied Meteorology, 43(2): 217-230.

Vuerich, E., Monesi, C., Lanza, L.G., Stagi, L. and Lanzinger, E., 2009. WMO field intercomparison of rainfall intensity gauges, WMO/TS-No. 1504.

Wang, A., Diao, Y., Pei, T., Jin, C. and Zhu, J., 2007. A semi-theoretical model of canopy rainfall interception for a broad-leaved tree. Hydrological Processes, 21(18): 2458-2463.

Wang, A., Li, J.Z., Liu, J.M., Pei, T.F. and Jin, C.J., 2005. A semi-theoretical model of canopy rainfall interception for Pinus Koraiensis Nakai. Ecological Modelling, 184(2-4): 355-361.

Wang, P.K. and Pruppacher, H.R., 1977. Acceleration to terminal velocity of cloud and raindrops. Journal of Applied Meteorology, 16(3): 275-280.

Watanabe, T. and Yamaguchi, I., 1993. The specific adhesional forces of aqueous droplets on crop leaf surfaces and factors influencing them. Journal of Pesticide Science, 18: 99-107.

Wigneron, J.P. et al., 2007. L-band microwave emission of the biosphere (L-MEB) model: Description and calibration against experimental data sets over crop fields. Remote Sensing of Environment, 107(4): 639-655.

Yan, H.P., Kang, M.Z., De Reffye, P. and Dingkuhn, M., 2004. A dynamic, architectural plant model simulating resource-dependent growth. Annals of Botany, 93(5): 591-602.

Yang, X.S. and Madden, L.V., 1993. Effect of ground cover, rain intensity and strawberry plants on splash of simulated raindrops. Agricultural and Forest Meteorology, 65(1-2): 1-20.

Zhang, G.F., Vivekanandan, J., Brandes, E.A., Meneghini, R. and Kozu, T., 2003. The shape-slope relation in observed gamma raindrop size distributions: Statistical error or useful information? Journal of Atmospheric and Oceanic Technology, 20(8): 1106-1119.